

Rotorcraft Simulation Model Enhancement to Support Land and Sea-Based Testing and Operational Analysis

Cheng-Jian He and Johnson Lee

Advanced Rotorcraft Technology, Inc.
1685 Plymouth St., Suit 250
Mountain View, CA 94043

ART Technical Report: ART-97-TR0006

Final Report
for

OSD SBIR Phase One Contract Number: N00421-97-C-1061
Naval Air Warfare Center Aircraft Division
Patuxent River, MD 20670-5304

DISTRIBUTION STATEMENT A
Approved for Public Release
Distribution Unlimited

June 10, 1997

20010622 109

REPORT DOCUMENTATION PAGE

Form Approved
OMB No. 0704-0188

Public reporting burden for this collection of information is estimated to average 1 hour per response, including the time for reviewing instructions, searching existing data sources, gathering information, including suggestions for reducing this burden, to Washington Headquarters Services, Directorate of Information Operations and Reports, 1215 Jefferson Davis Highway, Suite 1204, Arlington, VA 22202-4302, and to the Office of Management and Budget, Paperwork Reduction Project (0704-0188), Washington, DC 20503.

1. AGENCY USE ONLY (Leave blank)	2. REPORT DATE 10 June 1997	3. REPORT TYPE AND DATES COVERED Final Report 12/20/97 - 6/10/97
4. TITLE AND SUBTITLE ROTORCRAFT SIMULATION MODEL ENHANCEMENT TO SUPPORT LAND AND SEA-BASED TESTING AND OPERATIONAL ANALYSIS		5. FUNDING NUMBERS N00421-97-C-1061
6. AUTHOR(S) Cheng-Jian He Johnson Lee		
7. PERFORMING ORGANIZATION NAME(S) AND ADDRESS(ES) Advanced Rotorcraft Technology, Inc. 1685 Plymouth Street, Suite 250 Mountain View, CA 94043		8. PERFORMING ORGANIZATION REPORT NUMBER ART-97-TR0006
9. SPONSORING/MONITORING AGENCY NAME(S) AND ADDRESS(ES) Naval Air Warfare Center Aircraft Division Patuxent River, MD 20670-5304		10. SPONSORING/MONITORING AGENCY REPORT NUMBER S4578
11. SUPPLEMENTARY NOTES		
12a. DISTRIBUTION / AVAILABILITY STATEMENT Approved for public release; distribution is unlimited		12b. DISTRIBUTION CODE A
13. ABSTRACT (Maximum 200 words) This study addresses model enhancements to rotor wake modeling that significantly improve the prediction of helicopter behavior across the flight envelope. Specifically, the model enhancements have been made to include the tip vortex distortion effect in the finite state dynamic wake model to improve the poor prediction of rotorcraft off-axis response. The enhanced formulation allows for better prediction of aerodynamic interference. This includes the rotor aerodynamic interference on fuselage and other lifting surfaces. A modification of the finite state dynamic wake model has also been made to include the vortex ring state. The resulting simulation is applicable across the flight envelope. The enhanced model has shown a remarkable improvement in the prediction of helicopter response in both hover and forward flight.		
14. SUBJECT TERMS Rotorcraft model enhancement; finite state dynamic wake; flight simulation; vortex ring state; aerodynamic interference off-axis response		15. NUMBER OF PAGES 82
		16. PRICE CODE
17. SECURITY CLASSIFICATION OF REPORT UNCLASSIFIED	18. SECURITY CLASSIFICATION OF THIS PAGE UNCLASSIFIED	19. SECURITY CLASSIFICATION OF ABSTRACT UNCLASSIFIED
		20. LIMITATION OF ABSTRACT UNLIMITED

Contents

Contents	i
List of Figures	iii
Nomenclature	v
Summary	vii
1 Introduction	1
1.1 Background	1
1.1.1 Off-Axis Response	2
1.1.2 Aerodynamic Interference	3
1.1.3 Vortex Ring State	3
1.1.4 Rotor Wake Modeling	4
1.1.5 Comprehensive Interdisciplinary Simulation	5
1.2 Objectives	6
1.3 Approach	6
2 Finite State Wake with Distorted Tip Vortex	8
2.1 Finite State Dynamic Wake Theory of Peters/He	9
2.2 Formulation with Tip Vortex Distortion	12
2.3 Induced Flow due to Distorted Tip Vortex	14
2.4 Parametric Formulation of the Tip Vortex Effects	14
2.5 Tip Vortex Modeling	16
2.5.1 Tip Vortex Trajectory	17
2.5.2 Prescribed and Free Vortex	17
2.5.3 Induced Velocity Calculation	18
2.5.4 Global Geometric Distortion Effect	18
2.5.5 Local Distortion Effect	19
2.5.6 Vortex Core Model	19
2.6 Results and Discussion	20
2.6.1 Wake Distortion Influence Coefficients	20
2.6.2 Inflow State Variation with Vortex Wake Local Distortion . .	22

2.6.3 Off-Axis Response	23
3 Finite State Inflow Interference	53
3.1 Formulation	54
3.1.1 Partial Derivative Relationship	54
3.1.2 Gradient of Pressure Function	55
3.1.3 Three Components of Induced Velocity	55
3.2 Results and Discussion	58
3.2.1 Induced Flowfield	58
3.2.2 Effects on Helicopter Trim	59
3.2.3 Effects on Helicopter Response	59
4 Finite State Inflow in Vortex Ring State	68
4.1 Vortex Ring State Boundary	68
4.2 Vortex Ring Model	69
4.3 Results and Discussion	72
5 Conclusions	75
6 Future Plan	77
Bibliography	79

List of Figures

2.1	Ellipsoidal Coordinates	26
2.2	Skewed wake geometry due to hub translation	27
2.3	Illustration of blade lift distribution	28
2.4	Wake geometry at hover with different tip-path-plane rotation rates .	29
2.5	Wake geometry at 30 knots with different tip-path-plane rotation rates	30
2.6	Global geometric wake distortion influence coefficient in hover . . .	31
2.7	Variation of normalized induced flow states with Tpp angle of attack at 10 Knots	32
2.8	Variation of normalized induced flow states with Tpp angle of attack at 80 Knots	33
2.9	Fore-to-aft inflow influence coefficient due to pitch in forward flight .	34
2.10	Side-to-side inflow influence coefficient due to pitch in forward flight .	35
2.11	Side-to-side inflow influence coefficient due to roll in forward flight .	36
2.12	Fore-to-aft inflow influence coefficient due to roll in forward flight .	37
2.13	Variation of fore-to-aft inflow influence coefficient due to pitch with forward flight speed	38
2.14	Variation of side-to-side inflow influence coefficient due to roll with forward flight speed	39
2.15	Variation of side-to-side inflow influence coefficient due to pitch with forward flight speed	40
2.16	Variation of fore-to-aft inflow influence coefficient due to roll with forward flight speed	41
2.17	Illustration of rotor wake distortion in 30 Knots	42
2.18	Averaged inflow states from distorted and undistorted wake	43
2.19	Oscillating inflow states from distorted and undistorted wake, 30 Knots	44
2.20	Pilot control stick inputs	45
2.21	UH-60 body rotation rate response in hover	46
2.22	UH-60 body attitude response in hover	47
2.23	Effect of hub rotation on inflow and hub moment	48
2.24	Wake distortion effect on off-axis response in 60 Knots	49
2.25	Wake distortion effect on rotor tip-path-plane in 60 Knots	50
2.26	Wake distortion effect on hub moments in 60 Knots	51
2.27	Fuselage induced downwash at rotor plane, $\mu = 0.15$	52

3.1	Relative wind and wind-hub coordinates	61
3.2	Induced flow distribution along horizontal stabilator, $\mu = 0.2$	62
3.3	Induced velocity distribution along vertical tail, $\mu = 0.2$	63
3.4	Time Varying Induced Velocity at Fuselage and Horizontal Tail	64
3.5	UH-60 trim comparison at level flight	65
3.6	UH-60 responses to an aft longitudinal stick (1 inch) at 60 Knots	66
3.7	Main rotor interference effect on tail rotor, 60 Knots	67
4.1	Comparison of induced flow between prediction and measured data .	73
4.2	Induced flow variation in vertical and forward descent	74

Nomenclature

C_T	thrust coefficient, $C_T = T/[\rho\pi R^2(\Omega R)^2]$
L_q	blade sectional circulatory lift for induced flow calculation
$[L]$	induced inflow influence coefficient matrix
$[M]$	apparent mass matrix
m	harmonic number
n	polynomial number
p_{tpp}	Tip-path-plane roll rate
q_{tpp}	Tip-path-plane pitch rate
\bar{P}_n^m	normalized associated Legendre function of first kind, $\bar{P}_n^m(\nu) = (-1)^m P_n^m(\nu)/\rho_n^m$
\bar{Q}_n^m	normalized associated Legendre function of second kinds, $\bar{Q}_n^m(i\eta) = Q_n^m(i\eta)/Q_n^m(i0)$
Q	number of rotor blades
q_i	i-th component of induced velocity, dimensionless on ΩR
R	rotor radius
r	radial coordinate, nondimensionalized by R
r_{vc}	vortex core size
T	thrust
t	time, second
\bar{t}	nondimensional time, $\bar{t} = \Omega t$
V	mass flow parameter, dimensionless on ΩR
V_T	total flow through rotor disk, dimensionless on ΩR
w_{ih}	averaged momentum theory induced flow in hover
w_{i0}	averaged momentum theory induced flow
x_ξ, y_ξ, z_ξ	relative wind coordinate system
x_w, y_w, z_w	wind coordinate system

Greek Symbols

α	rotor disk angle of attack
α_n^m, β_n^m	induced flow states
μ_x, μ_y, μ_z	air velocity components in rotor hub coordinate system

μ	advance ratio, $\mu = \sqrt{\mu_x^2 + \mu_y^2}$
λ	total inflow, $\lambda = (-\mu_z) + \nu_0$
ρ	air density
$(\rho_n^m)^2$	integral (0 to 1) of $(P_n^m(\nu))^2 = \sqrt{\frac{1}{(2n+1)} \frac{(n+m)!}{(n-m)!}}$
τ_n^{mc}, τ_n^{ms}	pressure function coefficients (inflow forcing functions)
ψ	rotor azimuth measured in wind frame
Ω	rotor rotational speed, rad/sec.
Φ	nondimensional pressure
$\phi_n^m(r)$	inflow radial modal functions
$\nu, \eta, \bar{\psi}$	ellipsoidal coordinates, dimensionless
$(\)^*$	derivative with respect to \bar{t}
ξ	nondimensional coordinate along relative wind direction, positive upstream

Summary

A unique characteristic of rotorcraft is the dominating effect of the rotor down-wash on the aerodynamics of the rotor and the airframe. This study addresses enhancements to inflow modeling that significantly improve the prediction of helicopter behavior across the flight envelope when used in conjunction with a comprehensive rotorcraft simulation. The simulation includes interaction of a broad range of phenomena and subsystems including rotor dynamics, rotor wake, unsteady airloads with dynamic stall, the flight control system and the propulsion (including engine dynamics and fuel control).

Specifically, the model enhancements that have been made under the Phase One effort can be grouped into three areas.

- The tip vortex distortion effect due to the hub rotation has been included in the finite state dynamic wake model formulation to overcome the poor prediction of rotorcraft off-axis response. Also a significant breakthrough has been accomplished in the development of a parametric formulation of the finite state dynamic wake model with wake distortion influence coefficients derived from a distorted vortex wake model in both hover and forward flight.
- The enhanced formulation allows for better prediction of aerodynamic interference. This includes the rotor aerodynamic interference on other lifting surfaces such as the horizontal tail, the vertical fin, and the tail rotor.
- A modification of the finite state dynamic wake model has been made to include the vortex ring state. The resulting simulation is applicable across the flight envelope.

Investigations have been performed to prove the feasibility of the approach. The enhanced model has been validated against measured data in hover, forward flight and in the vortex ring state. The results have shown a remarkable improvement in the prediction of helicopter response in both hover and forward flight.

Chapter 1

Introduction

Modern computer simulation and computer aided analysis technology have found widespread applications in various engineering fields. Its potential for shortening the rotorcraft design cycle, reducing cost, enhancing flight test productivity, and increasing the safety of flight operations is yet to be explored. High fidelity piloted flight simulation models are required to support land and sea-based flight testing and operational analysis. Such models need to represent rotorcraft accurately before they can be utilized in both engineering analysis for flight test support and piloted flight simulation for training under routine or emergency conditions. Among other things, a reliable prediction of rotorcraft dynamic response to flight control inputs is a fundamental requirement in piloted flight simulation. Although many efforts have been undertaken to improve rotorcraft mathematical modeling, the capability of predicting certain aspects of rotorcraft response is still poor.

As economic development continues its global expansion, the world market is becoming more competitive. Unfortunately, both the production and operational costs of rotorcraft have been too high and have made the rotorcraft industry noncompetitive in the commercial transportation marketplace, Ref. [1]. A computer based simulation tool will certainly provide a solution for increased productivity and reduced cost. A reliable simulation tool will provide the rotorcraft industry with the capability to achieve more affordable development, test and operation of rotorcraft.

1.1 Background

Although there exists a number of tools for rotorcraft modeling and analysis, the prediction of the helicopter behavior in flight including in the design phase is a primary industrial challenge. Some areas that require model enhancement for high fidelity simulation are the helicopter off-axis response prediction, aerodynamic interference modeling, and simulation of unique environments, such as vortex ring state, or ship deck landing.

1.1.1 Off-Axis Response

One of the most perplexing problems with existing rotorcraft flight analysis/simulation programs is the inability to predict the correct vehicle **off-axis response** (e.g., lateral axis response due to the longitudinal control). Not only does the magnitude not correlate with flight test data, but the trend is also erroneous, Refs. [2] and [3]. The current inability of simulations to predict the correct qualitative rotorcraft response limits their application in design, flight test support and training.

The problem has attracted worldwide attention and efforts in resolving it, Refs. [4] to [8]. These investigations have mainly concentrated on the pitch-roll coupling. They have indicated that the physics which causes a discrepancy between the test data and the simulation in the off-axis response correlation is related to the rotor aerodynamics. Refs. [4] and [5] emphasize the dynamic wake distortion during transient maneuvers of the rotorcraft. When the rotor tip-path-plane tilts due to the application of the cyclic control, the rotor tip vortex deforms in a dynamic fashion resulting in an induced velocity variation over the rotor disk. The influence of the induced flow is such that it causes a reversal in the off-axis tip-path-plane tilt (lateral tilt in the case of pitch and longitudinal tilt in the case of roll) in a direction that agrees with the flight test data.

Reference [4] develops a model based on a prescribed vortex wake trajectory for steady helicopter body rotation in hover. Reference [5] modifies the inflow dynamics from simple momentum theory in hover by adding a constant gain feedback term explicitly related to the helicopter pitch or roll rate. A separate numerical solution to a curved vortex tube associated with the steady pitch rate is applied to obtain the parameters for the inflow dynamics equations. Reference [6] applies parameter identification techniques to flight test data to capture this effect by identifying an aerodynamic phase angle that is tuned to improve the off-axis response correlation with the test data. Reference [7] introduces a concept of steady induced angular momentum due to the rotor downwash swirl. The cross coupling moments due to the so called "virtual inertia effect" during helicopter pitch and roll are added to the helicopter body dynamics equations. The moments introduced by Ref. [7] behave like mechanical gyro moments, but are from the air rotation. Ref. [7] shows that adding these moments in the helicopter body dynamics improves the pitch-roll cross coupling response. However, no formulation or detailed calculation of these moments has been given by Ref. [7]. Ref. [8] applies the vortex method using nonuniform vortex rings in a dynamic fashion to compute the induced velocities at both main rotor and tail components. Ref. [8] shows a better prediction in phugoid and lateral-directional modes.

The above efforts have greatly enriched our understanding of the cross coupling response problem. The investigations have indicated that the pitch-roll cross coupling results from combined effects of various phenomena. The rotor aerodynamics is the key to solving the poor prediction of the cross coupling response for existing rotorcraft simulation programs. Although some simple formulations have been offered, they are

limited to steady rotation in hover and rely on separate methods (system identification or vortex method) to obtain the cross coupling parameters. There is a need to address this problem in a systematic way and provide a well defined solution that is valid for the full range of the flight conditions encountered in helicopter flight operation.

1.1.2 Aerodynamic Interference

The efforts taken in Refs. [4] to [7] have been focused on main rotor pitch-roll cross coupling. There are a broader range of off-axis response phenomena that are more closely related to the **aerodynamic interference**. Unfortunately, this is another poorly modeled phenomena in rotorcraft simulation.

The aerodynamic interference includes interference of rotor-rotor, rotor-fuselage, and rotor-empennage (vertical fin and horizontal surfaces). These aerodynamic interferences can have considerable influence on rotorcraft performance, flight control and vibration. It has been noticed that much of the redesign efforts on helicopters over the past 30 years have been driven by the unexpected negative impact of aerodynamic interference, Refs. [9] and [10]. The aerodynamic interaction plays a major role in affecting the helicopter off-axis responses, such as, pitch due to sideslip, yaw due to collective or pitch, etc.. The most important interference effects are the ones from the main rotor wake. It is also the most difficult to model and time consuming to compute. There have been both analytical and experimental works, Refs. [11] to [16] that investigate the phenomena. However, at the present time, most flight simulation programs, either use simple momentum estimation models, or adopt crude empirical models or table look-ups for specific vehicles. The sophisticated and time consuming vortex wake is only utilized in non-real time rotorcraft trim and steady state flight analysis, Refs. [17] to [20].

1.1.3 Vortex Ring State

Another deficiency of existing rotorcraft simulations is flight in a **vortex ring state**. Both the helicopter main rotor and tail rotor can encounter the vortex ring state during flight. It is one of the most critical flight conditions where flight safety is concerned. The main rotor could run into the vortex ring state when the helicopter is descending. The tail rotor would encounter the problem when it is in sideward flight or in a side wind. The capability to simulate the rotorcraft in the vortex ring state will provide a safety guide to flight test and training that will reduce the hazards of entering the vortex ring state in flight.

The vortex ring state analysis is another issue that needs to be addressed in order for a full flight rotorcraft simulation program to be applicable in all ranges of the flight environment. Moreover, a reliable vortex ring state simulation is required for flight safety in support of flight test and training. There are experimental studies describing the rotor vortex ring phenomena, Refs. [21] to [26]. Empirical uniform

induced velocity equations for vertical descent can be found in the literature, Ref. [27]. However, very limited analytical modeling of the vortex ring state is available. Reference [28] presented an analytical model by modifying the rotor uniform induced flow in the vortex ring state using a cylindrical vortex sheet with a linear decay vortex strength. The model is, however, limited to vertical descent. Recently, ART modified the model in Ref. [28], allowing the equation to be applicable in both hover and forward flight, Ref. [16]. But, the modified model has a problem in transition from normal flight to the vortex ring state.

Another interesting aspect of the vortex ring state modeling is the establishment of the vortex ring state boundary. The establishment of the vortex ring state boundary can, on the one hand, serve as a safety guide for rotorcraft operation. It can also be used to modify the finite state dynamic wake equations for a smooth modeling transition from the normal flow to the vortex ring state. There has been research work performed in determining the vortex ring state boundary. Reference [24] assumed that the normal component of the blade tip vortex translational velocity is the sum of half of the averaged rotor downwash and the normal relative airflow speed. From this assumption, Ref. [24] then defined the vortex ring state boundary by setting the normal component of the blade tip vortex translational velocity to zero. Physically, this boundary criteria, in fact, addresses the center of the vortex ring state instead of the boundary. Reference [29] proposed a different criteria for entrance of the vortex ring state by checking if the component of the relative airflow is negative in the direction of the rotor downwash. In application, this criteria is too conservative since it indicates that the helicopter will enter the vortex ring state during the descent at almost all descending angles. In reality, the helicopter can still fly safely at a small descent speed without entering the vortex ring state. When the helicopter is in forward flight, the safety margin is even larger. Therefore, a more accurate vortex ring state criteria is yet to be defined.

1.1.4 Rotor Wake Modeling

The previously identified defects in current rotorcraft simulations are mostly related to the rotor aerodynamics. Rotor aerodynamics remains one of the most challenging tasks in rotorcraft simulation modeling. Among all of the rotor aerodynamic phenomena, the rotor wake problem remains the essential issue. The wake is of primary importance in determining the rotor aerodynamic behavior, which directly affects almost every aspect of rotorcraft flight including performance, flight dynamics, stability, vibration, and aeroacoustic noise. Detailed modeling of the rotor wake has traditionally relied on modeling of a discretized field of vortex elements that are trailed and shed from the rotor blade due to radial and azimuthal changes in airloads. This “vortex wake” can predict the induced velocity distribution from the potential functions used to describe each discrete vortex element in the model. Two types of vortex wake models are commonly used. The Prescribed Wake model assumes the

geometry of the vortex elements relative to the rotor and only updates the strength of these elements due to the changing airloads on the rotor blades. The Free Wake model allows the position of the vortex elements to change due to the local induced velocity at each element. Both approaches are iterative and enforce a periodic steady state condition on the rotor loads to compute the strength and position of the vortex elements at each flight condition. They are therefore used predominantly for steady state performance prediction.

The **finite state dynamic wake model** developed by Peters and He, Refs. [30] to [32], represents a major advance in rotorcraft simulation technology. Beginning with potential functions derived from a prescribed wake geometry, this method postulates a truncated series solution to the induced velocity distribution, and derives closed form equations for the coefficients of this solution. The level of detail of the flow distribution may then be customized to the user's application by the selection of the number of radial and azimuthal terms in the expansion (the finite state). A key feature of this approach is the inclusion of an acceleration potential based on the inertia of the air mass that allows for the prediction of the transient behavior of the inflow (dynamic inflow). The finite state dynamic wake model has the sophistication of the classical prescribed vortex wake for modeling accuracy. At the same time it offers efficiency in satisfying the stringent computational demands of flight simulation. The capability of the finite state dynamic inflow model to predict induced velocity under both steady and maneuvering flight conditions is a major advantage over the vortex wake models that are based on periodicity assumptions for the wake and are therefore limited to steady state conditions. The increasingly widespread application of finite state dynamic inflow approach throughout rotorcraft flight dynamics community makes it an ideal candidate for enhancement to resolve the deficiencies of existing rotorcraft simulation models.

1.1.5 Comprehensive Interdisciplinary Simulation

A distinctive characteristic of rotorcraft is the strong coupling of its structure, aerodynamics, propulsion, and control system. Any meaningful rotorcraft simulation must model all these disciplines and their couplings. The fidelity of the simulation highly depends on how well each of these disciplines and their couplings are addressed. The FLIGHTLAB simulation program developed by Advanced Rotorcraft Technology, Inc. (ART) offers a comprehensive, multidisciplinary rotorcraft analysis/simulation software tool, Ref. [33]. It provides physically based rotorcraft modeling, including models of different levels of sophistication (selective fidelity) for the structure, aerodynamics, propulsion (engine/drivetrain), and flight control system. FLIGHTLAB models are reconfigurable to deal with different types of rotorcraft (single-main rotor, tandem rotors, co-axial rotors, and tiltrotors) as well as different rotor configurations (articulated, hingeless, bearingless, teetering, and gimbaled). The reconfiguration can be done by selection from available options and entering different data, instead

of modifying the simulation code. FLIGHTLAB provides a unified analysis and simulation environment to carry out the performance, stability, control response (time and frequency), load calculations, and pilot-in-the-loop simulation. The enhancement of rotorcraft modeling in FLIGHTLAB with the capability of predicting off-axis response, modeling aerodynamic interaction and simulating the vortex ring state will provide a valuable computer aided simulation/analysis tool to support flight test and flight simulation effectively.

1.2 Objectives

The overall objective is to enhance current rotorcraft simulation modeling to offer a cost effective tool that supports land and sea based testing and operational analysis. In achieving the goal, the Phase I efforts are to develop a theoretical finite state dynamic wake formulation to include the wake distortion effect and investigate the feasibility of the approach. Under Phase I, the new formulation will approach the problem in a systematic way so that the resulting model will be applicable in a full range of flight conditions. The formulation will also include the rotor wake interference for aerodynamic coupling among rotors and other lifting surfaces. The formulation will be developed for implementation in a comprehensive rotorcraft simulation program to allow for the interaction of various disciplines related to the flight modeling and simulation, such as the coupling of the finite state dynamic wake with the unsteady airloads, the structure elasticity, the propulsion system dynamics and flight control system.

1.3 Approach

The approaches taken are to resolve the deficiency of current rotorcraft simulation programs in the off-axis response, aerodynamic interaction, and vortex ring state prediction through the improvement of the Peters/He finite state dynamic wake model, Refs. [30] to [32]. The enhanced finite state dynamic wake model will model the transient wake deformation and inherently address the source of off-axis correlation, while providing a more computationally efficient approach than a vortex wake model. Also the enhancement will provide a more global and robust representation than a semi-empirical model tuned to the experimental data.

The enhanced finite state dynamic wake model will be incorporated into FLIGHTLAB to evaluate the effectiveness of these enhancements in improving the prediction of the flight dynamic response. FLIGHTLAB's comprehensive modeling and selective fidelity capabilities will ensure a uniform level of sophistication in modeling all interacting phenomena. For Phase One, the enhanced formulation for the general finite state dynamic wake model will be developed. The implementation is made to a three state inflow model to demonstrate the feasibility of the approach. A full implemen-

tation of the general finite state dynamic wake equations will be addressed in Phase Two.

The details of the formulation of the rotorcraft simulation model enhancement will be presented in the chapters that follow. The **innovations** of this approach are first summarized:

1. Inclusion of the tip vortex distortion effect in the widely used finite state dynamic wake model to overcome the poor prediction of rotorcraft off-axis response.
2. Modification of finite state dynamic wake model in the vortex ring state to generate a simulation model applicable across the flight envelope.
3. Enhancement for the finite state dynamic wake model to allow for aerodynamic interaction.
4. Integration of the enhanced finite state dynamic wake model into a comprehensive simulation program (FLIGHTLAB) to address the inter-disciplinary couplings.

Chapter 2

Finite State Wake with Distorted Tip Vortex

Ref. [34] first observed that the theoretical pitch-roll damping of of helicopters did not agree with flight measurements and attributed this discrepancy to inflow variation over the rotor disk. Ref. [35] provided a mathematical model to explain this phenomenon, and made the first systematic exploration that established a quasi-steady relation between instantaneous perturbation in thrust and perturbation in induced flow based on momentum theory. Since then, the theory of dynamic inflow has experienced a development from the simple momentum approach to a sophisticated finite state dynamic wake theory, Refs. [36] to [40] and Refs. [30] to [32].

The Peters/He finite state dynamic wake model describes the variation of the rotor downwash in a dynamic fashion. It represents the induced downwash over the rotor plane in terms of a series of polynomials for spanwise variation and harmonic (sine and cosine) functions for azimuthal variation. The finite state dynamic wake model offers a formulation so that the user can tailor the sophistication of the model to his needs by truncating the series. It is applicable in both steady and maneuver flight conditions. The finite state dynamic wake model presents the induced flow equations in a format consistent with those of the rotor dynamics. Moreover, it provides closed form solutions for its coefficient matrices, which significantly reduces the computation time. Because of these advantages over other wake solutions, the finite state dynamic wake model has found widespread applications in flight dynamics modeling and simulation, and is becoming a standard industry formulation for rotorcraft simulation. The original Peters/He finite state dynamic wake model, Refs [30] to [32], has three major limitations. First, it gives the analytical closed form solution to the normal downwash at the rotor plane only, which limits its application for rotor interference modeling. Second, its induced velocity calculation is derived from a prescribed undistorted cylindrical wake geometry. Third, it has a singularity in the vortex ring state where the well defined slipstream no longer exists. This prevents it from accurately predicting the cross coupling response and the vortex ring state.

2.1 Finite State Dynamic Wake Theory of Peters/He

Before we proceed to the derivation of an enhanced formulation to the Peters/He finite state dynamic wake model for including the tip vortex distortion effect, a brief review of the fundamental equations of the finite state dynamic wake theory is necessary. The Peters/He finite state dynamic wake model offers a new approach to complicated helicopter rotor unsteady wake modeling. It solves the problem from fundamental unsteady fluid dynamics. The solution is based on the governing equations for an incompressible potential flow, Ref. [30].

For an incompressible potential flow with small perturbations, the continuity and momentum equations can be written in index notation as

$$q_{i,i} = 0 \quad (2.1)$$

$$q_{i,0} - V_T q_{i,\xi} = -\Phi_{,i} \quad (2.2)$$

Eq. (2.1) is the continuity equation for mass conservation and Eq. (2.2) is the momentum equations for force equilibrium. The above equations are written in index notation for conciseness. The index i represents i -component of the velocity. The q_i are the perturbation velocity components, Φ is the pressure, $(),_0$ is a nondimensional time derivative, and $(),_\xi$ is the derivative along the relative wind direction.

From equation (2.2), it can be seen that spatial variation of the pressure is the superposition of contributions from both the gradient of velocity along the relative wind direction (or convection) and the unsteadiness of the flow field. The unsteady contribution $q_{i,0}$ is unique to the finite state induced flow theory. All conventional vortex wake models do not include this term and therefore are only quasi-steady in nature.

In the solution of Eqs (2.1 and 2.2), we divide the pressure into two parts (i.e., the part due to convection, denoted as Φ^V , and the part due to unsteadiness denoted as Φ^A). Then the pressure can be expressed as

$$\Phi = \Phi^V + \Phi^A \quad (2.3)$$

or

$$\Phi_{,i} = \Phi_{,i}^V + \Phi_{,i}^A \quad (2.4)$$

where

$$\Phi_{,i}^A = -q_{i,0} \quad (2.5)$$

$$\Phi_{,i}^V = V_T q_{i,\xi} \quad (2.6)$$

If we differentiate equation (2.2) with respect to the index i , then interchange the differentiation order of both $(i, 0)$ and (ξ, i) with the help of continuity equation (2.1), a Laplace's equation for pressure function can be obtained as follows,

$$\Phi_{,ii} = 0 \quad (2.7)$$

In a similar way, from equations (2.5) and (2.6), we have

$$\Phi_{,ii}^V = 0 \quad (2.8)$$

and

$$\Phi_{,ii}^A = 0 \quad (2.9)$$

Equations (2.8) and (2.9) indicate that each part of the total pressure satisfies Laplace's equation. Thus, each can be thought of as an acceleration potential, which is significant for the formulation of the theory. The boundary conditions for each Φ component are that the pressure match the blade loading on the rotor blades and be zero at infinity.

By the method of separation of variables, the solutions to the Eq. (2.7) can be obtained as, [30].

$$\Phi = -\frac{1}{2} \sum_{m=0}^{\infty} \sum_{n=m+1, m+3, \dots}^{\infty} \bar{P}_n^m(\nu) \bar{Q}_n^m(i\eta) [(\tau_n^{mc}) \cos(m\bar{\psi}) + (\tau_n^{ms}) \sin(m\bar{\psi})]$$

Similarly, we can have the solution for the Eqs. (2.8) and (2.9).

$$\Phi^V = -\frac{1}{2} \sum_{m=0}^{\infty} \sum_{n=m+1, m+3, \dots}^{\infty} \bar{P}_n^m(\nu) \bar{Q}_n^m(i\eta) [(\tau_n^{mc})^V \cos(m\bar{\psi}) + (\tau_n^{ms})^V \sin(m\bar{\psi})] \quad (2.11)$$

$$\Phi^A = -\frac{1}{2} \sum_{m=0}^{\infty} \sum_{n=m+1, m+3, \dots}^{\infty} \bar{P}_n^m(\nu) \bar{Q}_n^m(i\eta) [(\tau_n^{mc})^A \cos(m\bar{\psi}) + (\tau_n^{ms})^A \sin(m\bar{\psi})] \quad (2.12)$$

where the $\bar{P}_n^m(\nu)$ and $\bar{Q}_n^m(i\eta)$ are the normalized first and second kind of associated Legendre functions. The τ_n^{mc} and τ_n^{ms} are pressure functions and can be related to the blade lift. The ν , η and $\bar{\psi}$ are the ellipsoidal coordinates as defined in Fig. 2.1.

To establish the inflow dynamic equations, we expand the normal induced flow at rotor plane in terms of radial distribution and azimuthal variation,

$$w(r, \psi, \bar{t}) = \sum_{m=0}^{\infty} \sum_{n=m+1, m+3, \dots}^{\infty} \phi_n^m(r) [\alpha_n^m(\bar{t}) \cos(m\psi) + \beta_n^m(\bar{t}) \sin(m\psi)] \quad (2.13)$$

The radial expansion functions, $\phi_n^m(r)$, are the polynomial functions in the radial position, r . The α_n^m and β_n^m are the induced flow expansion coefficients. They are, in fact, the states of the rotor induced flow. Once these inflow states are solved from the inflow dynamics equations, the induced flow distribution at the rotor plane can be obtained from the Eq. (2.13).

As suggested by the Eq. (2.4), the induced flow field can be solved by the superposition of the unsteady and the convection. Solving the Eq. (2.5) gives

$$[M] \{ \alpha_n^m \}^* = \frac{1}{2} \{ \tau_n^{mc} \}^A \quad (2.14)$$

$$[M] \{ \beta_n^m \}^* = \frac{1}{2} \{ \tau_n^{ms} \}^A \quad (2.15)$$

At the same time, solving the Eq. (2.6) results

$$\{ \alpha_n^m \} = \frac{1}{2} [L^c] \{ \tau_n^{mc} \}^V \quad (2.16)$$

$$\{ \beta_n^m \} = \frac{1}{2} [L^s] \{ \tau_n^{ms} \}^V \quad (2.17)$$

Combining the Eq. (2.14) with (2.16) and the Eq. (2.15) with (2.17) and using the relationship of Eq. (2.4) gives final finite state induced flow equations as

$$[M] \left\{ \begin{array}{c} \vdots \\ \{ \alpha_n^m \} \\ \vdots \end{array} \right\}^* + [L^c]^{-1} \left\{ \begin{array}{c} \vdots \\ \{ \alpha_n^m \} \\ \vdots \end{array} \right\} = \frac{1}{2} \left\{ \begin{array}{c} \vdots \\ \{ \tau_n^{mc} \} \\ \vdots \end{array} \right\} \quad (2.18)$$

$$[M] \left\{ \begin{array}{c} \vdots \\ \{ \beta_n^m \} \\ \vdots \end{array} \right\}^* + [L^s]^{-1} \left\{ \begin{array}{c} \vdots \\ \{ \beta_n^m \} \\ \vdots \end{array} \right\} = \frac{1}{2} \left\{ \begin{array}{c} \vdots \\ \{ \tau_n^{ms} \} \\ \vdots \end{array} \right\} \quad (2.19)$$

In the above, the τ_n^{mc} and τ_n^{ms} are the inflow forcing functions. They can be computed from blade airloads, Ref. [32].

$$\tau_n^{oc} = \frac{1}{2\pi} \sum_{q=1}^Q \left[\int_0^1 \frac{L_q}{\rho \Omega^2 R^3} \phi_n^o(r) dr \right] \quad (2.20)$$

$$\tau_n^{mc} = \frac{1}{\pi} \sum_{q=1}^Q \left[\int_0^1 \frac{L_q}{\rho \Omega^2 R^3} \phi_n^m(r) dr \right] \cos(m\psi_q) \quad (2.21)$$

$$\tau_n^{ms} = \frac{1}{\pi} \sum_{q=1}^Q \left[\int_0^1 \frac{L_q}{\rho \Omega^2 R^3} \phi_n^m(r) dr \right] \sin(m\psi_q) \quad (2.22)$$

where L_q is blade sectional circulatory lift that can be evaluated from any time domain unsteady airload model, Ref. [41].

In the above equations, the $[L]^c$ and $[L]^s$ matrixes are obtained from a nondistorted cylindrical wake geometry in closed form. It does account for the effect of hub translational motion through a wake skewing angle, Fig. 2.2. But, it assumes no wake distortion due to the nonuniform wake induced velocity and hub rotation. The enhancement is to develop a formulation that includes these effects.

2.2 Formulation with Tip Vortex Distortion

The rotor blade tip vortex has been a dominant factor that affects rotor performance and response. Thus, the modeling of the tip vortex has long been a central issue in the rotor solution. The existing Peters/He finite state wake theory, Refs. [30] to [32], relies on adding more inflow states to approximate the tip vortex. Since the tip vortex is a concentrated vortex with strong discontinuity while the inflow states are continuous functions, the approximation with continuous inflow states to the discontinuous tip vortex has limitations. The approximation could be significant at the tip region if the tip vortex is strong, such as in the case of a rectangular blade tip.

Since the blade tip vortex is a dominant phenomena in the rotor wake modeling, we focus our efforts in introducing the tip vortex distortion into the new finite state wake formulation. In order to achieve computational efficiency while retaining necessary modeling accuracy, it has been a common practice in most comprehensive rotorcraft vortex wake codes that only the tip vortex is allowed to move freely for wake distortion modeling.

In this approach, we will derive two alternative formulations. The first general formulation allows for a combination of a tip vortex with the finite state dynamic wake equations for a complete dynamic induced flow solution. The other formulation provides parametric equations where the induced flow influence coefficients are extracted utilizing the results from a separate tip vortex model.

In the first formulation, the existing finite state dynamic wake model is modified and combined with a tip vortex model in one module. The effects of tip vortex distortion both **global** (such as those due to the hub rotation) and **local** (such as those due to vortex self-induced distortion) will be allowed for in the model. This approach has the advantage of a more accurate description of the physical phenomena, but will be very computationally intensive. It will be suitable for non-real time analysis on more complicated problems, such as blade-vortex interaction, vibratory load and aeroacoustic noise. The parametric formulation, on the other hand, utilizes predetermined wake distortion influence coefficients and adds little additional computation to the original finite state dynamic wake solution. Thus, the parametric formulation offers computational efficiency and satisfies the demand for real time simulation. Due to the complexity of the vortex deformation, only the global geometric wake distortion from the hub rotation and quasi-steady local vortex geometry distortion due to the self-induced velocity can be included in the parametric formulation.

To start with, we modify the blade tip vorticity modeling by introducing a concentrated tip vortex. The nondistorted cylindrical wake geometry is also improved by including the tip vortex distortion due to both the hub rotation and wake induced velocity. Since the current finite state induced flow model, Eqs (2.18 to 2.22), has already accounted for the contributions from the blade tip vorticity in terms of continuous distribution of the blade tip loading, a double counting of these effects needs to be avoided.

Let τ_n^m be the induced flow forcing function computed from the blade lift distribution, Fig. 2.3. We define a new inflow forcing function $\{\tau_n^m\}_{tip}$ that has only the contribution from the blade tip region (dot lines filled area), Fig. 2.3. By modifying Eqs. (2.14) to (2.17) to allow the induced velocity due to the convection to be computed from a distorted tip vortex, we can derive a new set of induced flow equations that include tip vortex distortion effects.

For unsteady part, Eqs. (2.14 and 2.15), we have

$$2 [M] \{ \alpha_n^m \}^* = \{ \tau_n^{mc} \}^A - \{ \tau_n^{mc} \}_{tip}^A + \{ \tau_n^{mc} \}_{tip}^A \quad (2.23)$$

$$2 [M] \{ \beta_n^m \}^* = \{ \tau_n^{ms} \}^A - \{ \tau_n^{ms} \}_{tip}^A + \{ \tau_n^{ms} \}_{tip}^A \quad (2.24)$$

For the convection part, Eqs. (2.16 and 2.17), we have

$$\{ \alpha_n^m \} = \frac{1}{2} ([L^c] \{ \tau_n^{mc} \}^V - [L^c] \{ \tau_n^{mc} \}_{tip}^V) + \{ \alpha_n^m \}_{tip} \quad (2.25)$$

$$\{ \beta_n^m \} = \frac{1}{2} ([L^s] \{ \tau_n^{ms} \}^V - [L^s] \{ \tau_n^{ms} \}_{tip}^V) + \{ \beta_n^m \}_{tip} \quad (2.26)$$

where the $\{ \alpha_n^m \}_{tip}$ and $\{ \beta_n^m \}_{tip}$ are the contributions from the tip vortex. They can be computed from the induced flow distribution over the rotor plane due to the distorted tip vortex. Multiplying both sides of Eqs. (2.25) and (2.26) by $[L^c]^{-1}$ and $[L^s]^{-1}$, respectively, results in

$$[L^c]^{-1} \{ \alpha_n^m \} = \frac{1}{2} (\{ \tau_n^{mc} \}^V - \{ \tau_n^{mc} \}_{tip}^V) + [L^c]^{-1} \{ \alpha_n^{mc} \}_{tip} \quad (2.27)$$

$$[L^s]^{-1} \{ \beta_n^m \} = \frac{1}{2} (\{ \tau_n^{ms} \}^V - \{ \tau_n^{ms} \}_{tip}^V) + [L^s]^{-1} \{ \beta_n^{mc} \}_{tip} \quad (2.28)$$

The final finite state induced flow equations with the tip vortex distortion effect can be obtained by combining Eq. (2.27) with (2.23) and Eq. (2.28) with (2.24).

$$\begin{aligned} & [M] \{ \alpha_n^m \}^* + [L^c]^{-1} \{ \alpha_n^m \} \\ &= \frac{1}{2} (\{ \tau_n^{mc} \} - \{ \tau_n^{mc} \}_{tip}) + [L^c]^{-1} \{ \alpha_n^{mc} \}_{tip} + \frac{1}{2} \{ \tau_n^{mc} \}_{tip}^A \end{aligned} \quad (2.29)$$

$$\begin{aligned} & [M] \{ \beta_n^m \}^* + [L^s]^{-1} \{ \beta_n^m \} \\ &= \frac{1}{2} (\{ \tau_n^{ms} \} - \{ \tau_n^{ms} \}_{tip}) + [L^s]^{-1} \{ \beta_n^{mc} \}_{tip} + \frac{1}{2} \{ \tau_n^{ms} \}_{tip}^A \end{aligned} \quad (2.30)$$

It is noted that the above equations introduce the inflow forcing function associated with induced flow rate change, $\{\tau_n^{mc}\}_{tip}^A$ and $\{\tau_n^{ms}\}_{tip}^A$. In steady flight, they are negligible. But during maneuver flight, we need to compute them from the change of induced flow associated with the tip loading. To do this, a set of inflow state

equations for the tip vortex can be applied

$$[M] \left\{ \alpha_n^m \right\}_{tip}^* + [L^c]^{-1} \left\{ \alpha_n^m \right\}_{tip} = \frac{1}{2} \left\{ \tau_n^{mc} \right\}_{tip} \quad (2.31)$$

$$[M] \left\{ \beta_n^m \right\}_{tip}^* + [L^s]^{-1} \left\{ \beta_n^m \right\}_{tip} = \frac{1}{2} \left\{ \tau_n^{ms} \right\}_{tip} \quad (2.32)$$

From the solution of the Eqs. (2.31) and (2.32), we can find

$$\left\{ \tau_n^{mc} \right\}_{tip}^A = 2 [M] \left\{ \alpha_n^m \right\}_{tip}^* \quad (2.33)$$

$$\left\{ \tau_n^{ms} \right\}_{tip}^A = 2 [M] \left\{ \beta_n^m \right\}_{tip}^* \quad (2.34)$$

$\{\tau_n^{mc}\}_{tip}^A$ and $\{\tau_n^{ms}\}_{tip}^A$ can also be obtained directly from the integration of the blade tip loading that is associated with the induced flow rate. In this way, no additional inflow state equations need to be solved.

2.3 Induced Flow due to Distorted Tip Vortex

In the new finite state induced flow formulation, Eqs. (2.29) and (2.30), the new terms $\{\alpha_n^{mc}\}_{tip}$ and $\{\beta_n^{mc}\}_{tip}$ allow for the effects of tip vortex distortion. Let the $w_{tip}(r, \psi, t)$ be the induced velocity associated with the distorted tip vortex, from Eq. (2.13) we have

$$\{\alpha_n^0\}_{tip} = \frac{1}{2\pi} \int_0^{2\pi} \int_0^1 [r \bar{P}_n^0(\nu) w_{tip}(r, \psi, t)] dr d\psi \quad (2.35)$$

$$\{\alpha_n^m\}_{tip} = \frac{1}{\pi} \int_0^{2\pi} \int_0^1 [r \bar{P}_n^m(\nu) \cos(m\psi) w_{tip}(r, \psi, t)] dr d\psi \quad (2.36)$$

$$\{\beta_n^m\}_{tip} = \frac{1}{\pi} \int_0^{2\pi} \int_0^1 [r \bar{P}_n^m(\nu) \sin(m\psi) w_{tip}(r, \psi, t)] dr d\psi \quad (2.37)$$

Note that we have made use of the orthogonality of the trigonometrical and associated Legendre functions, Ref. [30], in deriving the above equations.

In implementation, we can compute the induced velocity directly from the distorted tip vortex using a vortex model. The induced flow coefficients $\{\alpha_n^{mc}\}_{tip}$ and $\{\beta_n^{mc}\}_{tip}$ are then obtained from the Eqs. (2.35) to (2.37) and added to the final inflow dynamics equations, Eqs. (2.29) and (2.30).

2.4 Parametric Formulation of the Tip Vortex Effects

We can also formulate the induced flow due to the distorted tip vortex in parametric form so that no tip vortex has to be explicitly included in the solution of finite state

induced flow equations. This can be done by extracting the wake distortion influence coefficients from the induced velocity resulting from a separate tip vortex model. Instead of using the total contribution from the distorted tip vortex, it is much more efficient to make use of the perturbation induced velocity due to the wake distortion in the parametric formulation. To do so, we rearrange Eqs. (2.25 and 2.26),

$$\{ \alpha_n^m \} = \frac{1}{2} [L^c] \{ \tau_n^{mc} \}^V + \{ \Delta\alpha_n^m \} \quad (2.38)$$

$$\{ \beta_n^m \} = \frac{1}{2} [L^s] \{ \tau_n^{ms} \}^V + \{ \Delta\beta_n^m \} \quad (2.39)$$

where $\{ \Delta\alpha_n^m \}$ and $\{ \Delta\beta_n^m \}$ are the perturbation induced velocity due to the wake distortion. They are

$$\{ \Delta\alpha_n^m \} = \{ \alpha_n^m \}_{tip} - \frac{1}{2} [L^c] \{ \tau_n^{mc} \}_{tip}^V \quad (2.40)$$

$$\{ \Delta\beta_n^m \} = \{ \beta_n^m \}_{tip} - \frac{1}{2} [L^s] \{ \tau_n^{ms} \}_{tip}^V \quad (2.41)$$

These perturbation inflow due to the wake distortion associated with the blade tip vortex can be further computed as

$$\begin{aligned} \{ \alpha_n^m \}_{tip} - \frac{1}{2} [L^c] \{ \tau_n^{mc} \}_{tip}^V &= w_{i0} [\Delta L^c]_{tip} \{ \tau_n^{mc} \}_{tip}^V \\ &+ \frac{w_{i0}}{\Omega} [\Delta L^c]_{rot} \left\{ \begin{array}{l} p_{tpp} \\ q_{tpp} \end{array} \right\} \end{aligned} \quad (2.42)$$

$$\begin{aligned} \{ \beta_n^m \}_{tip} - \frac{1}{2} [L^s] \{ \tau_n^{ms} \}_{tip}^V &= w_{i0} [\Delta L^s]_{tip} \{ \tau_n^{ms} \}_{tip}^V \\ &+ \frac{w_{i0}}{\Omega} [\Delta L^s]_{rot} \left\{ \begin{array}{l} p_{tpp} \\ q_{tpp} \end{array} \right\} \end{aligned} \quad (2.43)$$

where $[\Delta L^c]_{tip}$ and $[\Delta L^s]_{tip}$ are the wake distortion influence coefficients accounting for the perturbation effects of the local tip vortex distortion due to self-induced velocity. $[\Delta L^c]_{rot}$ and $[\Delta L^s]_{rot}$ are the wake distortion influence coefficients for the perturbation effects of the global geometric distortion of the tip vortex due to tip path plane rotation. These influence coefficients are normalized by an averaged momentum theory induced flow to reduce the rotor thrust dependency in extracting the coefficients.

Substituting Eqs. (2.42) and (2.43) into (2.25) and (2.26) and combining with Eqs. (2.23) and (2.24), we obtain

$$[M] \{ \alpha_n^m \}^* + [L^c]^{-1} \{ \alpha_n^m \} = \frac{1}{2} \{ \tau_n^{mc} \}$$

$$+w_{i0} \left[\Delta \hat{L}^c \right]_{tip} \left\{ \tau_n^{mc} \right\}_{tip}^V + \frac{w_{i0}}{\Omega} \left[\Delta \hat{L}^c \right]_{rot} \left\{ \begin{array}{l} p - (\beta_s)^* \\ q - (\beta_c)^* \end{array} \right\} \quad (2.44)$$

$$\left[M \right] \left\{ \beta_n^m \right\}^* + \left[L^s \right]^{-1} \left\{ \beta_n^m \right\} = \frac{1}{2} \left\{ \tau_n^{ms} \right\}$$

$$+w_{i0} \left[\Delta \hat{L}^s \right]_{tip} \left\{ \tau_n^{ms} \right\}_{tip}^V + \frac{w_{i0}}{\Omega} \left[\Delta \hat{L}^s \right]_{rot} \left\{ \begin{array}{l} p - (\beta_s)^* \\ q - (\beta_c)^* \end{array} \right\} \quad (2.45)$$

where

$$\left[\Delta \hat{L}^c \right]_{tip} = \left[L^c \right]^{-1} \left[\Delta L^c \right]_{tip} \quad (2.46)$$

$$\left[\Delta \hat{L}^s \right]_{tip} = \left[L^s \right]^{-1} \left[\Delta L^s \right]_{tip} \quad (2.47)$$

$$\left[\Delta \hat{L}^c \right]_{rot} = \left[L^c \right]^{-1} \left[\Delta L^c \right]_{rot} \quad (2.48)$$

$$\left[\Delta \hat{L}^s \right]_{rot} = \left[L^s \right]^{-1} \left[\Delta L^s \right]_{rot} \quad (2.49)$$

2.5 Tip Vortex Modeling

Two solution methodologies are typically adopted in fluid dynamics: Lagrangian or Euler methods. The Lagrangian method solves the time variation of each individual vortex element, while the Euler method deals with the flow field point instead of following the individual vortex elements. The Lagrangian approach has the advantage of being able to trace the vortex element and attain a time accurate wake geometry solution. This is particularly important for maneuver flight, as required in flight simulation modeling. The Lagrangian approach applies a time marching scheme that is sometimes susceptible to solution instability in low flight speed. The instability can be both physical and numerical. As observed from flow visualization, the rotor wake can become unstable under certain low speed conditions. On the other hand, the numerical truncation of the number of the tip vortex elements retained in the solution can also cause the trajectory of the vortex elements near the truncation boundary to diverge. Extending the tip vortex far down the stream will help the convergence of the solution. For computational efficiency, an approximate tip vortex geometry can be used at the far field since its effect on the rotor is less significant as compared to those vortex elements that are in the vicinity of the rotor blades. Numerical damping is also often applied for a converged solution when a nonlinear vortex solution is pursued, but, it filters out wake geometry dynamics. The Euler approach is based on the field concept. It presents the flow characteristics in term of the field description. For rotorcraft applications, the Euler approach allows for enforcing the periodic condition under steady-state flight. The enforcement of the periodic condition through numerical relaxation benefits the numerical stability, but its application is limited to steady flight condition.

For maneuver flight simulation, the rotor periodic condition no longer exists as the pilot constantly applies the controls. The Lagrangian approach is therefore the only viable method for a physically realistic solution.

2.5.1 Tip Vortex Trajectory

The induced velocity field in the vicinity of a lifting rotor is determined by the rotor wake geometry and wake strength. In general, it is a nonlinear phenomena since the wake strength and geometry interact with each other. On one hand, the change in wake strength (e.g., circulation of the vortex) results in a variation in the associated induced velocity. On the other hand, the induced velocity alters the wake geometry. The perturbation in the wake geometry in return will change the induced velocity distribution that affects the rotor airloads, and thus the wake strength.

In general, an accurate description of rotor wake geometry can only be obtained by combining the effects of helicopter rotor hub motion (both translational and rotation velocity), rotor self-induced velocity, wind, and interference induced velocity from other lifting rotors or lifting surfaces (such as, wing, fuselage, and etc.). Due to the complexity of the problem, certain approximations have to be made in order to achieve a feasible solution.

In the conventional free vortex model, an averaged rotor tip-path-plane is assumed for the tip vortex trajectory solution. The tip vortex trajectory is referred to the tip-path-plane. The relative geometric position between the tip vortex and tip-path-plane remains unchanged during the transition from one rotor revolution to the next. A typical helicopter transient peak response is less than about two to three rotor revolutions. Therefore, the averaged tip vortex geometry is no longer valid for maneuver flight modeling. To overcome this hurdle, we take an approach in which the tip vortex will be emanating from the physical blade tip at each time instant during the maneuver. **Thus, the tip vortex trajectory follows the instantaneous blade tip response, rather than the averaged tip-path-plane.** The accurate tip vortex shedding position is essential to catch the effect of hub transient translation and rotation. Once the tip vortex is shed into the flow field, it will move with the resultant velocity that is the vector superposition of the wind, rotor self induced velocity and interference velocity from other aerodynamic lifting surfaces.

$$\frac{d\vec{x}}{dt} = \vec{v}_{wind} + \vec{v}_i + \vec{v}_{int} \quad (2.50)$$

where \vec{x} is the vortex element moving velocity, \vec{v}_{wind} , \vec{v}_i and \vec{v}_{int} are the wind, rotor self-induced and interference velocity respectively.

2.5.2 Prescribed and Free Vortex

There are two approaches that are commonly utilized in rotor wake geometry modeling. One is the prescribed wake method in which the rotor wake geometry is pre-

scribed. The wake geometry description can be based on either experimental data (flow visualization) or analytical approximation, such as using averaged induced flow for self-induced effect on the wake geometry. The other approach is the free vortex concept. The free vortex solution allows the vortex elements to move in the flow field resulting from the superposition of wind and vortex induced velocity. The force-free condition is satisfied when the vortex segments are aligned with the resultant flow velocity. The free vortex solution models physical distortion of the rotor wake. But, there are hurdles associated with the rotor free vortex approach. Two major issues are the vortex decay and the vortex interactions. All free vortex solutions have to rely on tuning vortex core size to prevent singularities in order to obtain a converged solution.

2.5.3 Induced Velocity Calculation

The induced velocity is computed based on the Biot-Savart Law, Ref. [42]. The induced velocity at a flow field point 'p' due to a straight vortex line with constant circulation is calculated as

$$\vec{v}_i^p = \frac{\Gamma}{4\pi} \vec{r}_{ap} \times \vec{r}_{bp} \quad (2.51)$$

$$\frac{(r_{ap} + r_{bp})(1 - \frac{r_{dot}}{r_{bp}r_{ap}})}{r_{bp}^2 r_{ap}^2 - r_{dot}^2 + r_c^2(r_{ap}^2 + r_{bp}^2 - 2r_{dot})} \quad (2.52)$$

where \vec{r}_{ap} and \vec{r}_{bp} are the position vectors from the two ends of the vortex line (points 'a' and 'b') to the point 'p'. The scalar r_{dot} is defined as $r_{dot} = \vec{r}_{ap} \cdot \vec{r}_{bp}$, r_c is the size of the vortex core; and Γ is the circulation of the vortex.

2.5.4 Global Geometric Distortion Effect

Most existing rotor vortex wake models do not include the effect of transient rotor hub motion in maneuver flight. The finite state wake model does let the rotor wake follow the rotor tip-path-plane instantaneously in response to the hub translational motion, but the rotor wake moves as a whole cylinder without the time step effect on each individual wake element. Moreover, for hub rotation, even the steady motion effect has been completely ignored. These are the first order effects that must be addressed for the maneuvering flight simulation. The hub translation causes the rotor wake to be skewed, while the hub rotation produces curved wake geometry which has been found to be significant in affecting the helicopter pitch-roll cross-axis response. In our writing, we refer to the hub motion induced effects as **global geometric wake distortion effect**. The rotor tip vortex geometry can also be further distorted by its self-induced velocity and other interference velocities. We refer to that as the **local wake distortion effect**. The local distortion effect is important for blade-vortex interaction, aeroacoustics, and vibrations.

The first step we take for enhancement of rotorcraft simulation modeling is to include the global geometric wake distortion effect in the finite state wake equations. To model the effect properly, an accurate description of the rotor hub motion is essential. The comprehensive rotorcraft simulation program—FLIGHTLAB, Refs. [33], [41], [43], and [44]. provides an ideal tool due to its geometrically exact nonlinear structural dynamics modeling. All the airframe dynamic modeling in FLIGHTLAB is fully nonlinear without ignoring any higher order geometric terms. This is of importance under maneuver conditions where the attitude change of the helicopter body can be large enough so that the small angle assumption is no longer valid.

In our tip vortex geometry calculation, the tip vortex trajectory is described relative to the physical rotor hub frames that experience linear and angular motion in all three directions. The rotor hub frame is attached at the center of the rotor hub. It is defined such that 'x' points downstream, 'y' to the right and 'z' is up. The relative position of the tip vortex to the rotor hub frame is computed at each time step, and thus includes the instantaneous change in the rotor hub motion under maneuver flight conditions. In the model, the tip vortex emanates from the physical blade tip and then sets off to move in the flow field that results from the wind and induced velocity. To extract the global geometric effect on the wake distortion, the vortex moving velocity is assumed to be that of rotor momentum theory value. Under unsteady flight conditions, the momentum theory value is updated at each time step from the instantaneous rotor thrust.

2.5.5 Local Distortion Effect

The **local distortion effect** here refers to the wake distortion due to the nonuniform induced velocity field. Including this effect produces the so called free vortex wake model. The local wake distortion effect has been found to have an effect on the rotor vibratory loads and aeroacoustics. Its impact on the vehicle flight dynamics remains to be investigated. In Phase One, we concentrate on the finite state wake modeling with the global geometric wake distortion effect. We will proceed to model the local distortion phenomena and investigate its effect on the flight simulation under Phase Two effort.

2.5.6 Vortex Core Model

The vortex core model is always a challenging issue in a distorted vortex solution. The core size of the vortex plays an important role when the vortex element is close to the point where the induced velocity is to be calculated. Too small a vortex core size can cause an unrealistically large fluctuation of the induced flow velocity and often lead to diverged solutions when it couples with rotor dynamics. On the other hand, if the core size is too large, an inaccurate solution may result. Many existing free wake codes adopt an empirical number and fix the core size for the whole solution process.

Instead of using a fixed core size during the process of a free vortex solution, in this approach, we allow the size of the vortex core to vary with the time. The formula is based on the classical incompressible viscous flow solution. In this solution, a two dimensional plate is set to move at a constant forward speed, the vortex created from the plate boundary layer is then grown through the flow field. The vortex core variation with time is thus obtained as

$$\begin{aligned} r_{vc} &= \eta_c \sqrt{\nu \epsilon t} \quad (t < t_1) \\ &= r_{vc0} + \eta_c \sqrt{\nu \epsilon t} \quad (t \geq t_1) \end{aligned} \quad (2.53)$$

where η_c is a constant, ν is the kinematic viscosity and ϵ is the eddy viscosity coefficient. The parameter t_1 is the time when the vortex passes by the first following blade. The parameter r_{vc0} is the core size change at the time of t_1 . This formulation allows for the effect of blade/vortex interaction on the growth of the vortex core. When applying the formula to the helicopter blade tip vortex, the physical tip vortex development is more complicated than the decay process of the ideal laminar vortex where the eddy viscosity coefficient is unity. Thus, the parameter ϵ needs to be selected based on experimental data.

2.6 Results and Discussion

The results presented in this section include both the induced downwash variation due to the tip vortex distortion and its effects on the helicopter off-axis response. The inflow influence coefficients extracted from the distorted tip vortex are also discussed.

2.6.1 Wake Distortion Influence Coefficients

Figure 2.4 shows the trajectory of the rotor tip vortex under three different tip-path-plane pitch rates ($q_{tpp} = 0, 5.0, 10.0, 15.0 \text{ deg/sec}$) during hub rotation. Eight rotor wake revolutions are used in these models. The wake geometries are plotted 8 rotor revolutions after the start of the hub rotation. At this time, the hub rotation effect has been transported to the last wake element. The tip vortex trajectories that emanate from the physical blade tip present two distinctive features. The rotation of the rotor hub produces a curved vortex geometry as compared to a straight cylindrical line under the conventional method. Moreover, the hub rotation causes the vortex sheet to compress on one side and expand on the other. The extent to which the tip vortex geometry is curved and compressed/expanded depends on the rate at which the hub is rotating.

Figure 2.5 shows the wake geometries at 30 knots with the four tip-path-plane rotation rate. The curvature of the wake is less pronounced than that in hover,

however, the wake concentration near the rotor trailing edge is more than in the similar region shown in Fig. 2.4.

In the parametric formulation, the elements of $[\Delta L^c]_{rot}$ and $[\Delta L^s]_{rot}$ are the global geometric wake distortion influence coefficients due to the hub rotation. In modeling, the blade tip vortex is trailed from physical blade tip during the hub rotation. Thus, the wake distortion effect is, in fact, directly related to the tip-path-plane rotation as formulated in Eqs. 2.42 and 2.43. To extract the influence coefficients from the distorted vortex results, it needs to identify the independent variables with which these influence coefficients vary.

Fig. 2.6 shows the variation of wake distortion influence coefficients during hub pitch and roll in hover. The ΔL_{12} is the fore-to-aft inflow state (α_2^1) change due to the pitch rate. The ΔL_{21} is the side-to-side inflow state (β_2^1) change due to the roll rate. The ΔL_{11} and ΔL_{22} are the cross coupling for the change of α_2^1 due to the roll and the β_2^1 due to the pitch, respectively. It is noticed that the influence coefficients are essentially constants soon after reaching the limiting value, i.e., independent of pitch angle. It is also noted that the cross coupling between the induced flow change and pitch/roll motion, i.e., the ΔL_{11} and ΔL_{22} are much less as compared to the on-axis inflow change (ΔL_{12} and ΔL_{21}). The wake distortion influence coefficients obtained here are based on the formulation of Eqs. 2.44 and 2.45. If we convert the influence coefficient to an equivalent parameter in Ref. [5], we have an equivalent value of 1.45 as compared to the 1.5 reported in the Ref. [5]. This is due to the fact that we have used physically more accurate helix vortex segments instead of the vortex ring tube as adopted in Ref. [5].

Fig. 2.7 shows the perturbation induced flow state variation with tip-path-plane angle of attack (i.e., the angle between the free stream and tip-path-plane) during the pitching motion at different pitch rates in 10 Knots forward flight. The inflow states have been normalized by the averaged momentum uniform inflow value. Fig. 2.8 shows similar results at 80 Knots forward flight. One distinguished feature of these results is the linear variation with the pitch rate as indicated by a nearly constant factor difference in the results for different pitch rates. This is further confirmed by directly plotting of the influence coefficients, i.e., the slopes of the inflow states with respect to the rotation rate, against the tip-path-plane angle of attack, Figs. 2.9 and 2.10. Fig. 2.9 shows the influence coefficients of fore-to-aft induced flow distribution due to pitch rate at different forward flight speeds. The variations of influence coefficients with various pitch rates fall into essentially one curve at each of the forward flight speed (10, 30, 60 and 80 Knots). This suggests that these influence coefficients can be either tabulated or curve fit as a function of the flight speed and the tip-path-plane angle of attack. Fig. 2.10 presents the influence coefficients of side-to-side induced flow distribution due to pitch rate. This is the inflow due to cross-axis rotation. As seen, the effect of the cross coupling is one order smaller as compared with the on-axis results in Fig. 2.9.

Fig. 2.11 shows the influence coefficients of side-to-side induced flow distribution

due to the roll at various flight speeds. These are the inflow influence coefficients from the on-axis rotation. As shown, the influence coefficients reach a nearly constant value for all the speeds, indicating that the side-to-side induced flow state is only a linear function of the roll rate. Fig. 2.12 presents the influence coefficients of fore-to-aft induced flow distribution due to the roll at various flight speeds. These are the inflow influence coefficients from the cross-axis coupling. They are one order smaller than the influence coefficients for the on-axis rotation. Similarly, the influence coefficients reach nearly constant limiting values at each of the flight speeds and are basically independent of the roll rate.

For implementation, the inflow influence coefficients due to the wake distortion are also plotted against forward flight speed, Figs. 2.13 to 2.16. Fig. 2.13 is the variation of fore-to-aft inflow influence coefficients due to pitch with the flight speed. The coefficients are plotted for three typical tip-path-plane angle of attack. A large variation occurs in the speed range of hover to 30 Knots. The wake distortion effect decreases with the flight speed. It becomes negligible after 80 Knots. Fig. 2.14 shows the variation of side-to-side inflow influence coefficients due to roll with the flight speed. The effect of the wake distortion on the side-to-side inflow influence coefficient decreases as helicopter flies forward. Similarly, the effect is negligible after 80 Knots. Figs. 2.15 and 2.16 are the variations of cross-axis inflow influence coefficients with forward flight speed. The results show that these cross-axis inflow influence coefficients are very small at the typical range of tip-path-plane rotation (5, 10, and 20 degrees). Thus, the effects of the wake distortion on the cross-axis inflow influence coefficients is essentially negligible.

The above results present a breakthrough in modeling the global geometric wake distortion effect in the finite state dynamic wake formulation in forward flight because all the work before this have been limited to hover flight. Thus far, no systematic results have been obtained for the wake distortion influence coefficients in forward flight. With the above results, we can apply these wake distortion influence coefficients in the parametric formulation for flight simulation. Thus, our accomplishments have presented a practically feasible solution to the problem.

To summarize, the perturbation induced flow from the wake distortion due to the hub rotation is a function of flight speed and tip-path-plane angle of attack for pitch, and flight speed and tip-path-plane lateral tilt angle for roll. Most importantly, they are only linear functions of the pitch and the roll rates. Thus, there is no hurdle in implementing the parametric formulation to allow for global geometric wake distortion in flight simulation.

2.6.2 Inflow State Variation with Vortex Wake Local Distortion

In this section, we examine the effect of vortex local distortion due to rotor self-induced velocity by comparing the inflow state variation between the free vortex and

the finite state dynamic wake models. The inflow states for the vortex wake model are extracted from the induced flow distribution over the rotor plane by using Eqs. 2.35 to 2.37.

Fig. 2.17 illustrates the free vortex wake geometry of a UH-60 rotor in 30 Knots forward flight. This is the speed range where the rotor wake distortion is the most significant. Fig. 2.18 compares the uniform and first harmonic inflow states computed from undistorted and distorted wake. These are the three most important inflow states concerning the flight dynamics. They are the inflow states describing uniform (α_1^0), fore-to-aft (α_2^1) and side-to-side (β_2^1) distributions. As shown, both the free vortex model and finite state dynamic wake results have shown the same variation trend. There are only magnitude difference that could be compensated by the trim setting. Thus, the effect from the local wake distortion will be higher order as compared to the global geometric wake distortion that affects even the direction in which the rotorcraft responds in maneuver flight. Fig. 2.19 compares the inflow states of (α_2^1) and (β_2^1) in forward flight. The oscillation of the inflow states is mainly due to the blade passage effect (or blade bound vortex effect). The 4/rev oscillation of the inflow states for the 4-bladed rotor is clearly seen for both the undistorted and distorted wake. The wake distortion effect is not significant on the oscillation magnitude. There is a minor phase shift for the inflow states that may be due to the difference in inflow collocation points. When we extract the wake distortion influence coefficients, these bound vortex contribution will not be a concern since there is no bound vortex geometry distortion.

2.6.3 Off-Axis Response

The results presented in this section are to validate the enhanced finite state dynamic wake model as described above. The UH-60 helicopter response is computed in FLIGHTLAB simulation environment. The rotor blades are modeled as elastic using the FLIGHTLAB modal component. The enhanced finite state dynamic wake equation is applied for the rotor inflow dynamics modeling.

The first case investigated is the UH-60 response to a step lateral stick in hover. Figure 2.20 displays the pilot control inputs as applied to the simulation. Figure 2.21 is the helicopter body response to the pilot stick inputs. The results from the model with and without the wake distortion due to the hub rotation are compared to the flight test measured data. As seen, the model without considering the wake geometry change due to the hub rotation predicts a pitch rate (off-axis) response opposite to the test data. The wrong prediction of the response trend is, however, corrected by the enhanced 3-state inflow model that includes the wake geometry distortion effect due to the hub rotation during the transient maneuver. Figure 2.22 is the response of the helicopter attitude. The enhanced model predicts the right pitch attitude variation due to the lateral stick input.

To understand the improved prediction from the enhanced model, Fig. 2.23 com-

pares the rotor side-to-side induced flow distribution and rotor hub pitch moment from the two models. The upper plot displays the induced flow distribution at the peak of the body roll rate after the pilot lateral stick is applied. Compared to the existing finite state inflow model without the hub rotation effect, the enhanced model that introduces the hub rotation effect on the inflow calculation predicts a dramatic change in the rotor side-to-side induced flow variation. The change in the side-to-side inflow variation directly affects the rotor load distribution that generates a much different rotor pitch moment response, as indicated in the lower plot of Fig. 2.23. The hub pitch moment change from the enhanced model results in a correct helicopter pitch response to the lateral stick input.

Using the enhanced formulation, we have further investigated the effects on off-axis response in forward flight. Figure 2.24 shows the UH-60 helicopter response to a one inch aft longitudinal step stick input at 60 Knots forward flight. The results from three models and their correlation with the flight test data are compared. The first simulation model uses the unsteady uniform inflow with Glauert fore-to-aft inflow distribution. The other two are the 3-state inflow models with and without tip vortex distortion. For the on-axis pitch response correlation, all the three models have predicted the right trend. The uniform inflow model slightly overshoots. The 3-state inflow model without the wake distortion slightly underestimates the response peak. The wake distortion model provides the best correlation. But, all the three models matched the measured data within a reasonable accuracy. The off-axis response comparisons, however, have shown large difference. The uniform inflow model fails in predicting even the right trend. The 3-state inflow without tip vortex distortion shows too small of a roll rate amplitude response. Inclusion of the tip vortex distortion in the 3-state inflow model not only predicts the right direction in which the helicopter rolls, but also improves the correlation of the amplitude of the roll rate response, although there is a remaining difference as compared to the flight test data. Fig. 2.25 shows the rotor tip-path-plane variation during the maneuvering. A larger lateral tilt of the tip-path-plane to the right occurs with the simulation that models the wake distortion. The wake distortion effect is also reflected on the rotor hub moment variation, Fig. 2.26.

It is noted that the response peak of the roll rate predicted is still less than that of measured data. In fact, this is no surprise since there are other factors that affect the helicopter response in forward flight. This remaining difference can be due to the fuselage aerodynamic interaction on the rotor. As shown in Fig. 2.27 (from Ref. [30]) there is a rotor flow field variation due to the existence of a fuselage. In forward flight, the fuselage induces upwash in the forward part of the rotor plane and increases the downwash at the rear portion of the rotor plane. The rotor will respond to this fore-to-aft inflow variation in the lateral flapping that will further increase the roll response of the helicopter. The fuselage beneath the rotor mainly affects this fore-to-aft rotor inflow variation. It also increases with forward flight speed. In Phase Two effort, we will develop the fuselage interference model and investigate the fuselage

upwash influence on the helicopter response.

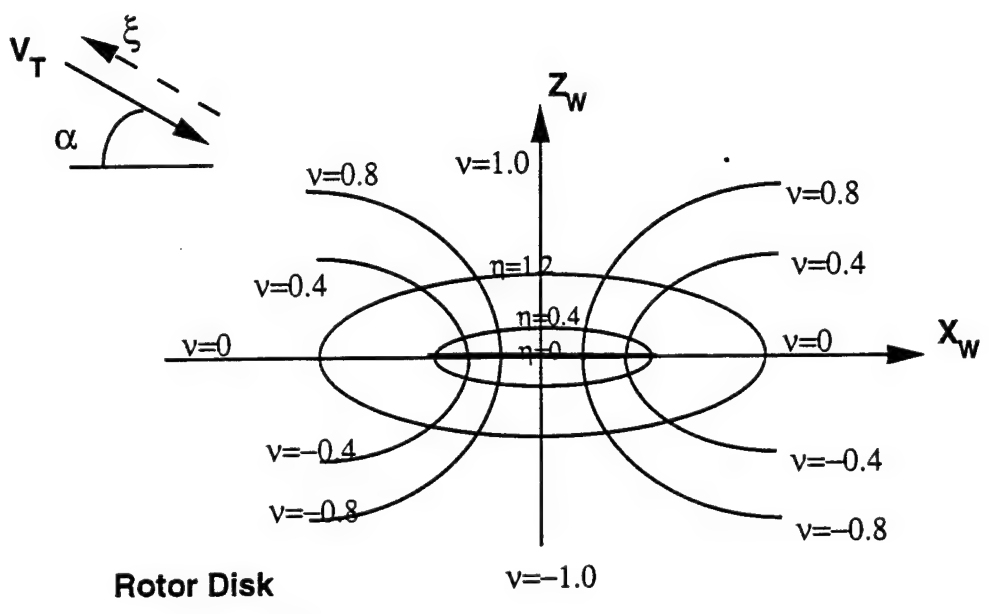


Figure 2.1: Ellipsoidal Coordinates

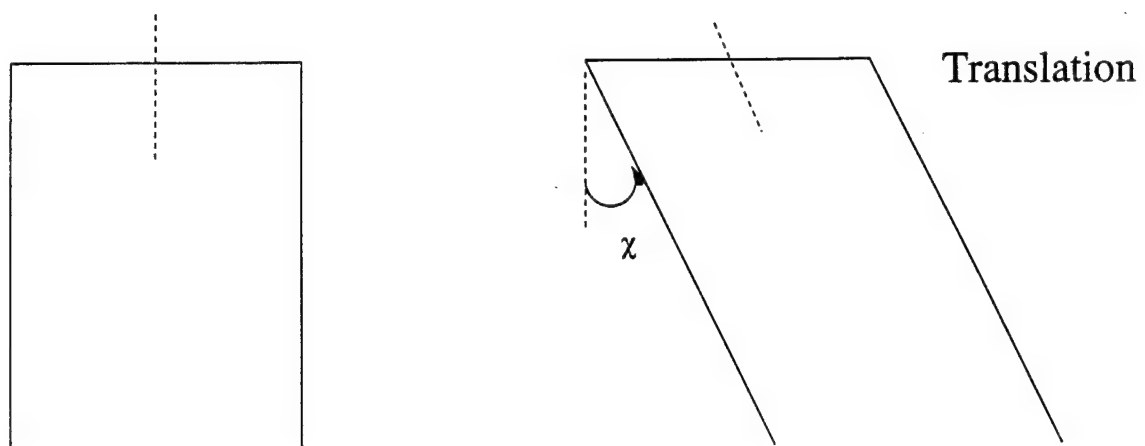


Figure 2.2: Skewed wake geometry due to hub translation

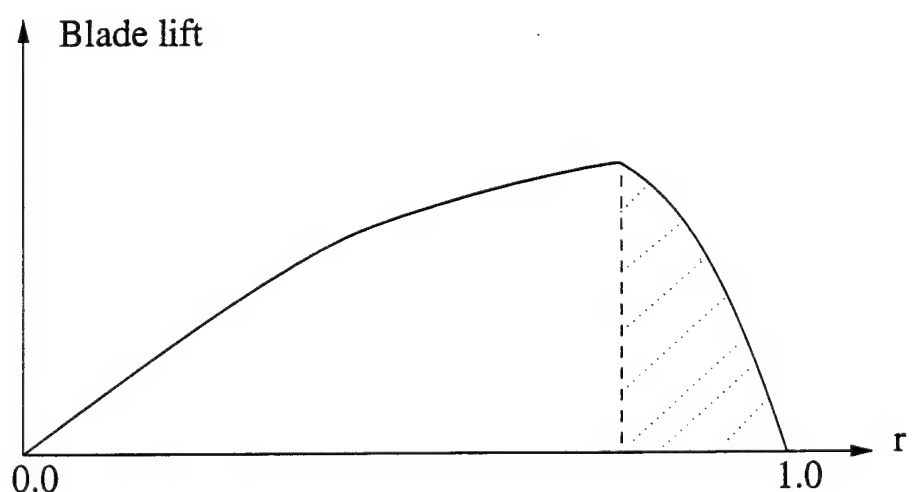


Figure 2.3: Illustration of blade lift distribution

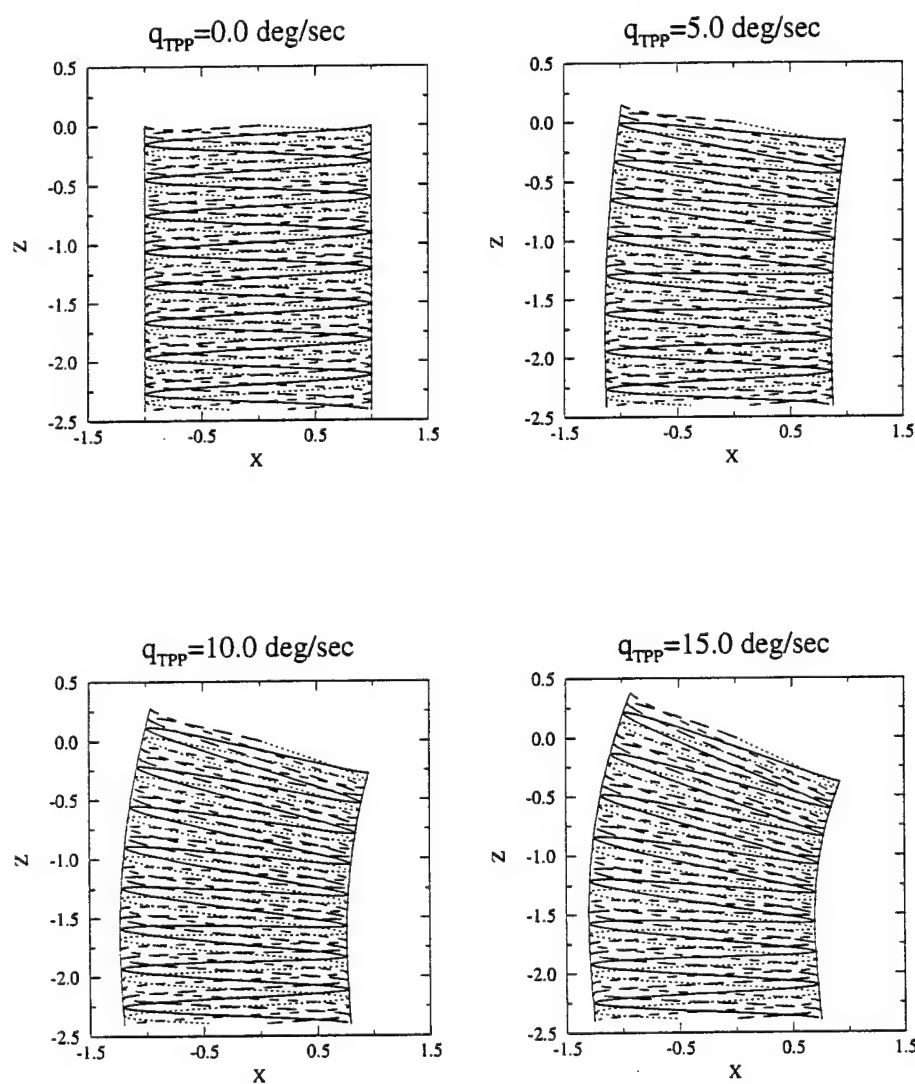


Figure 2.4: Wake geometry at hover with different tip-path-plane rotation rates

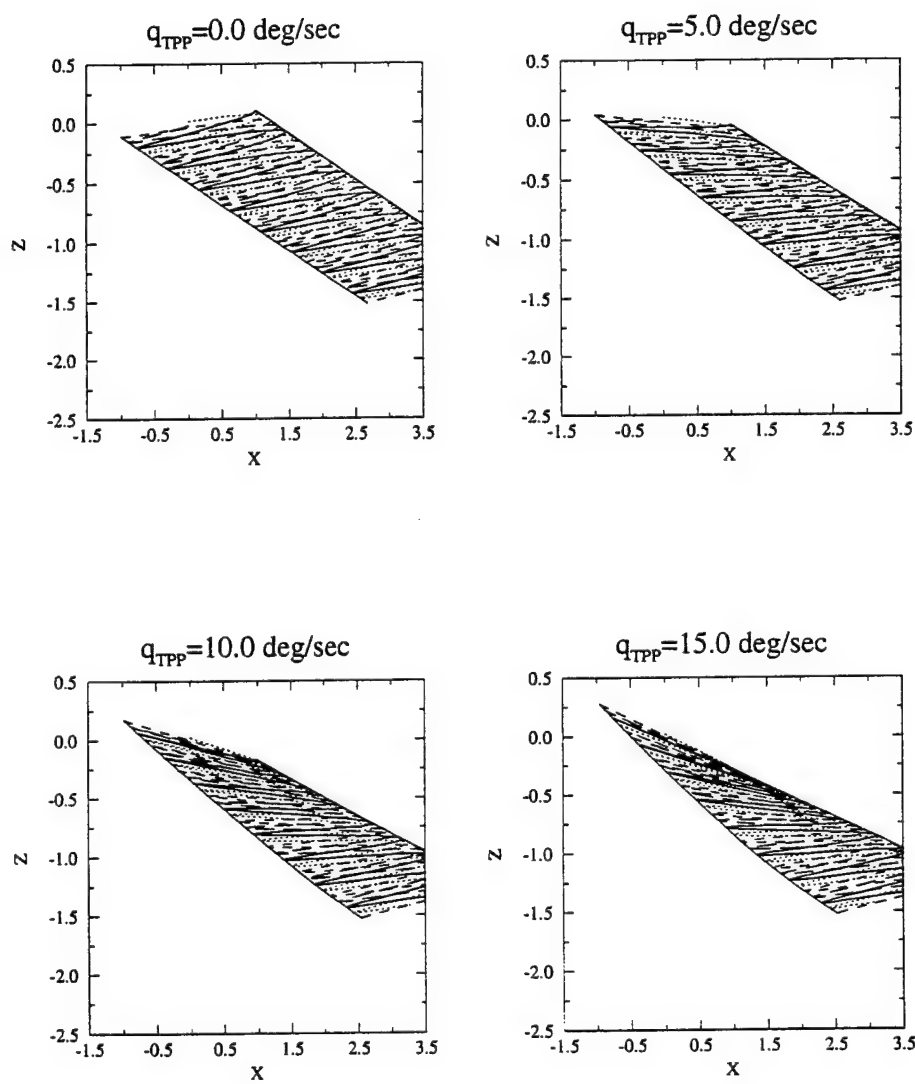


Figure 2.5: Wake geometry at 30 knots with different tip-path-plane rotation rates

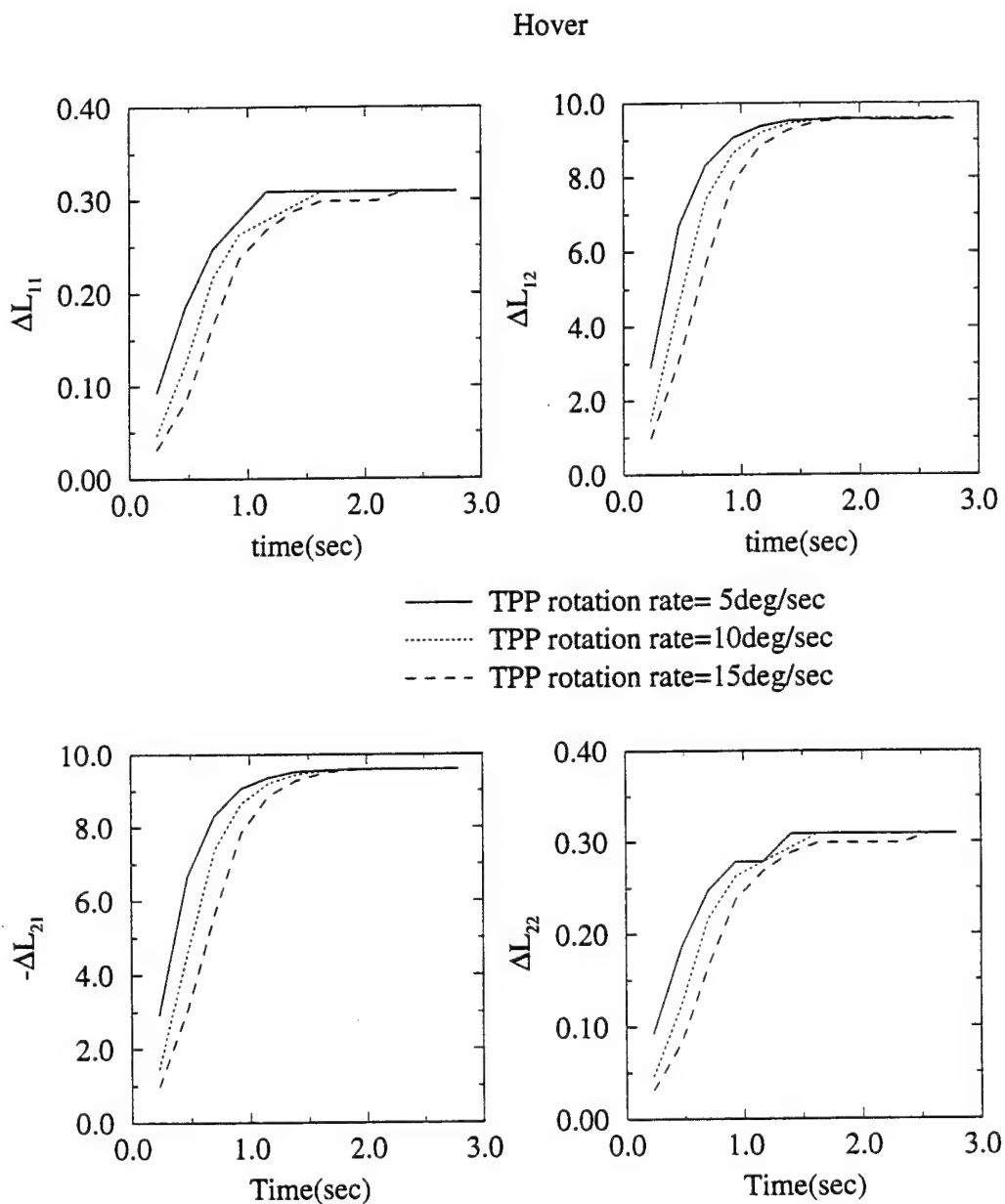


Figure 2.6: Global geometric wake distortion influence coefficient in hover

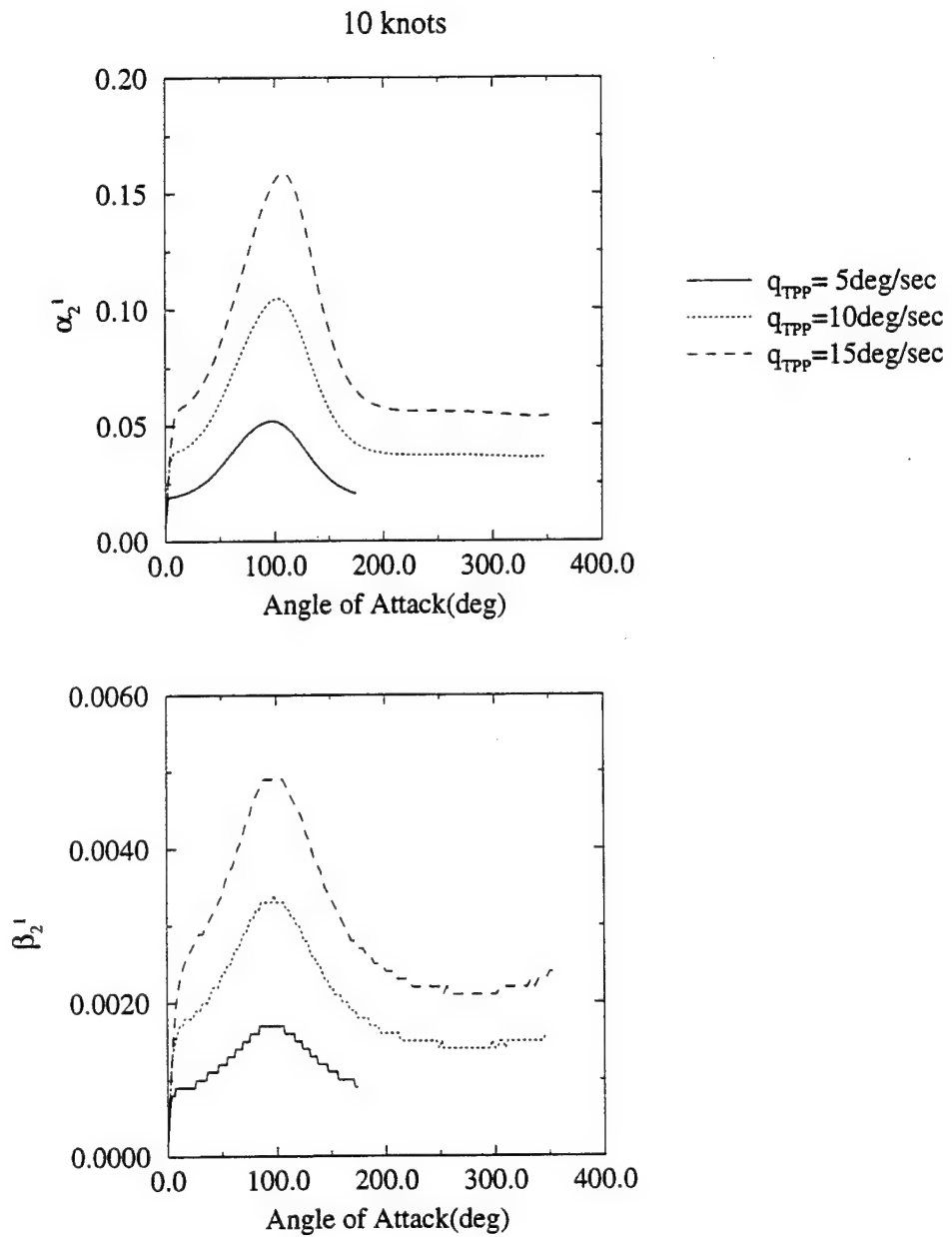


Figure 2.7: Variation of normalized induced flow states with Tpp angle of attack at 10 Knots

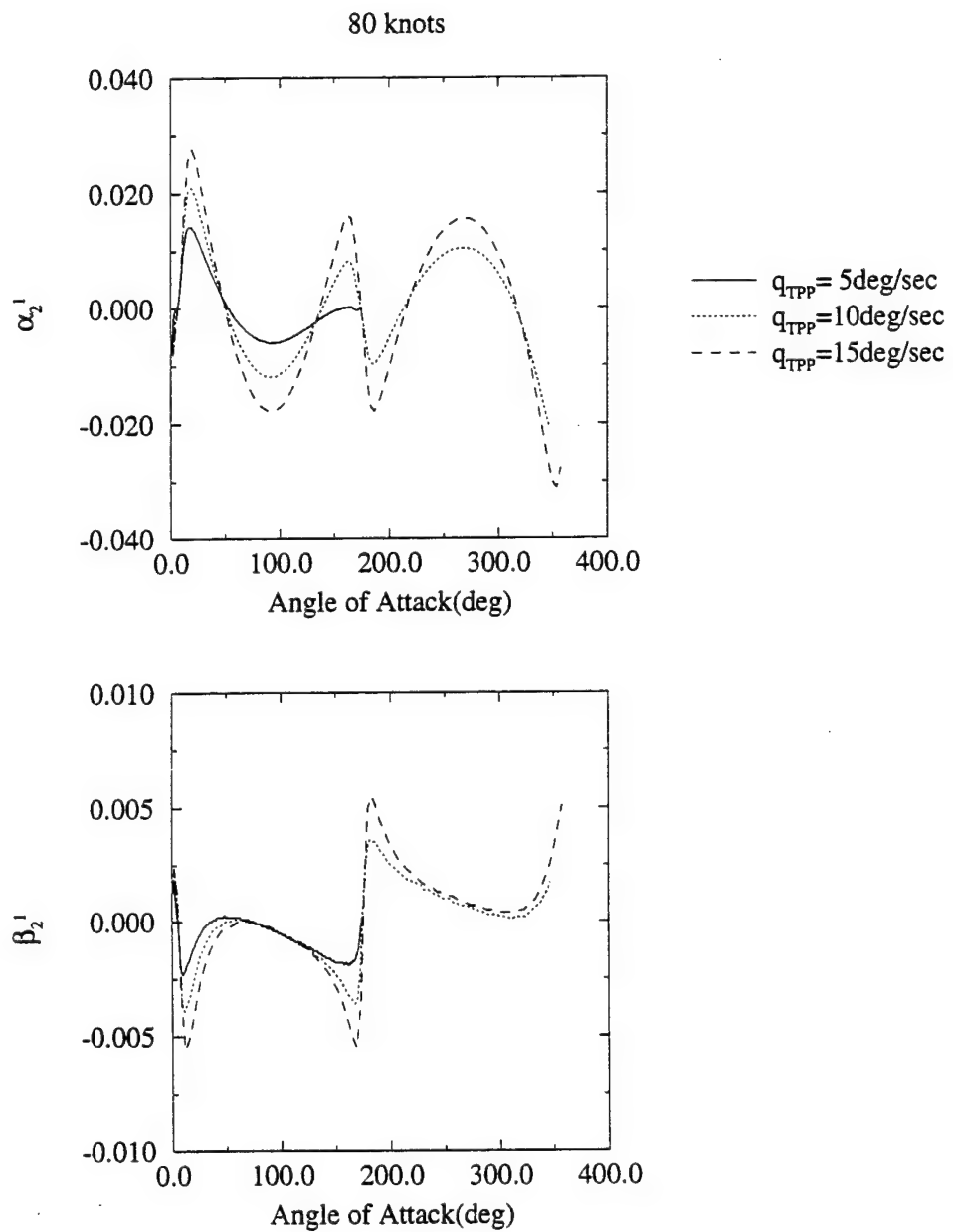


Figure 2.8: Variation of normalized induced flow states with Tpp angle of attack at 80 Knots

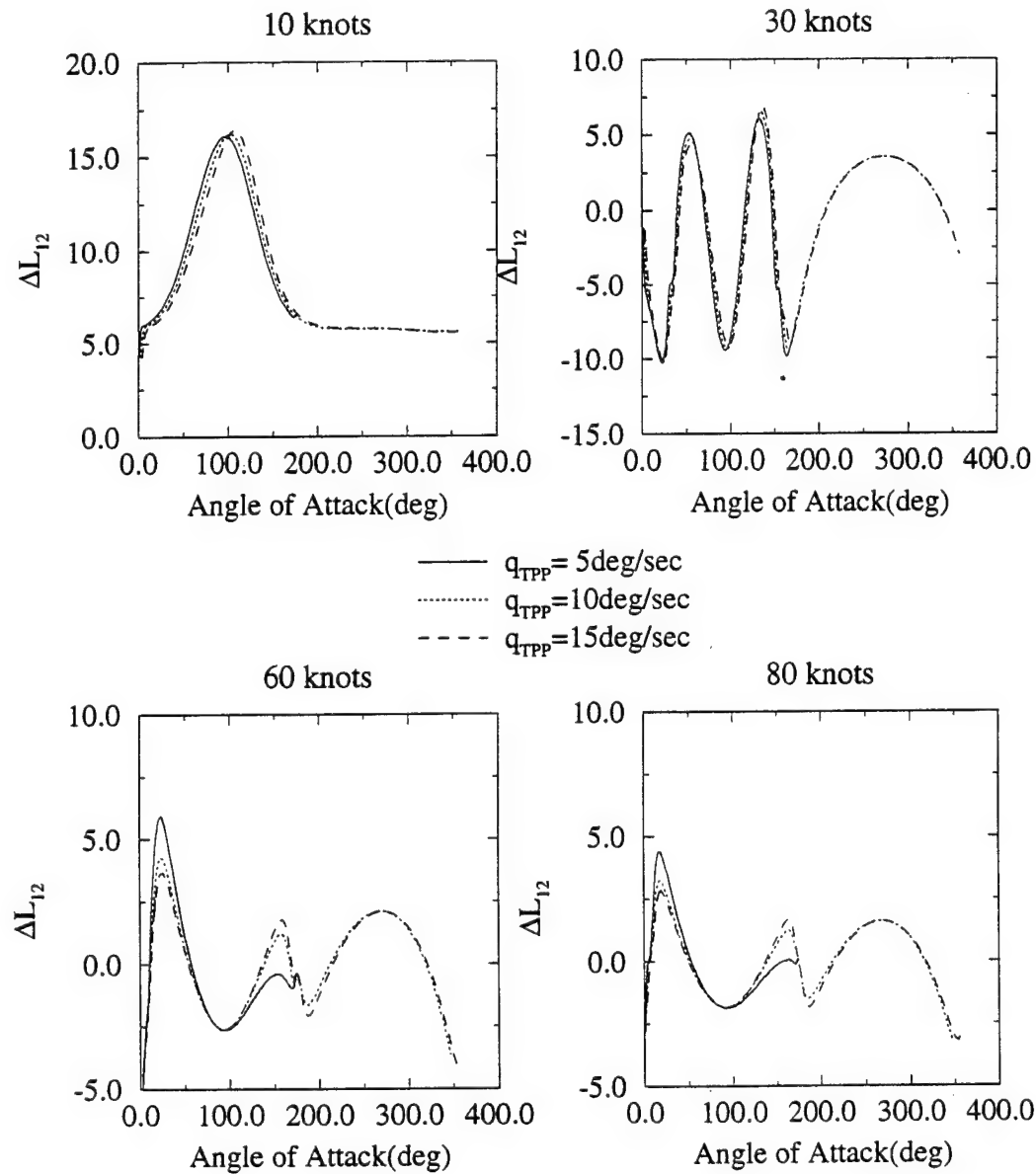


Figure 2.9: Fore-to-aft inflow influence coefficient due to pitch in forward flight

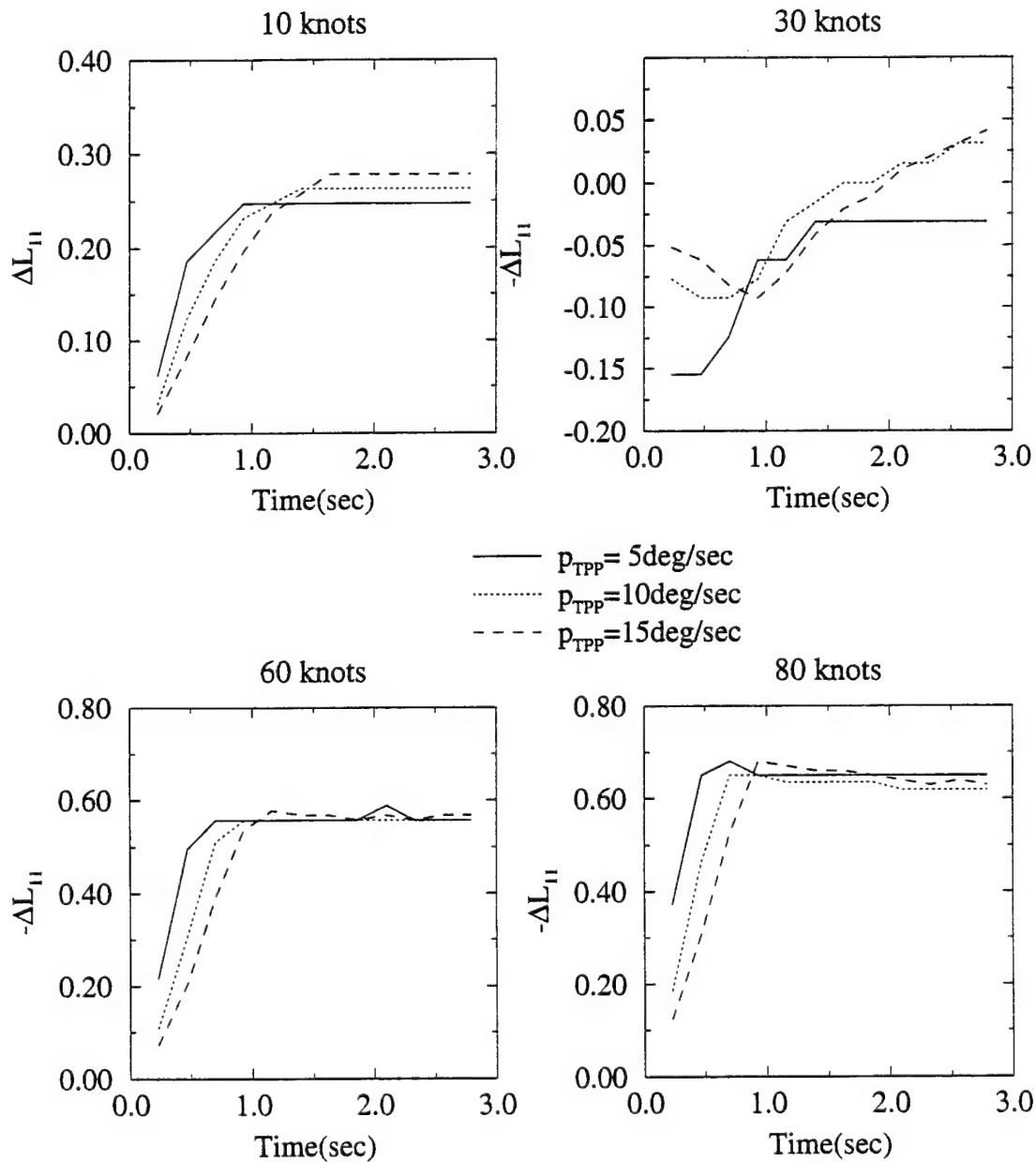


Figure 2.10: Side-to-side inflow influence coefficient due to pitch in forward flight

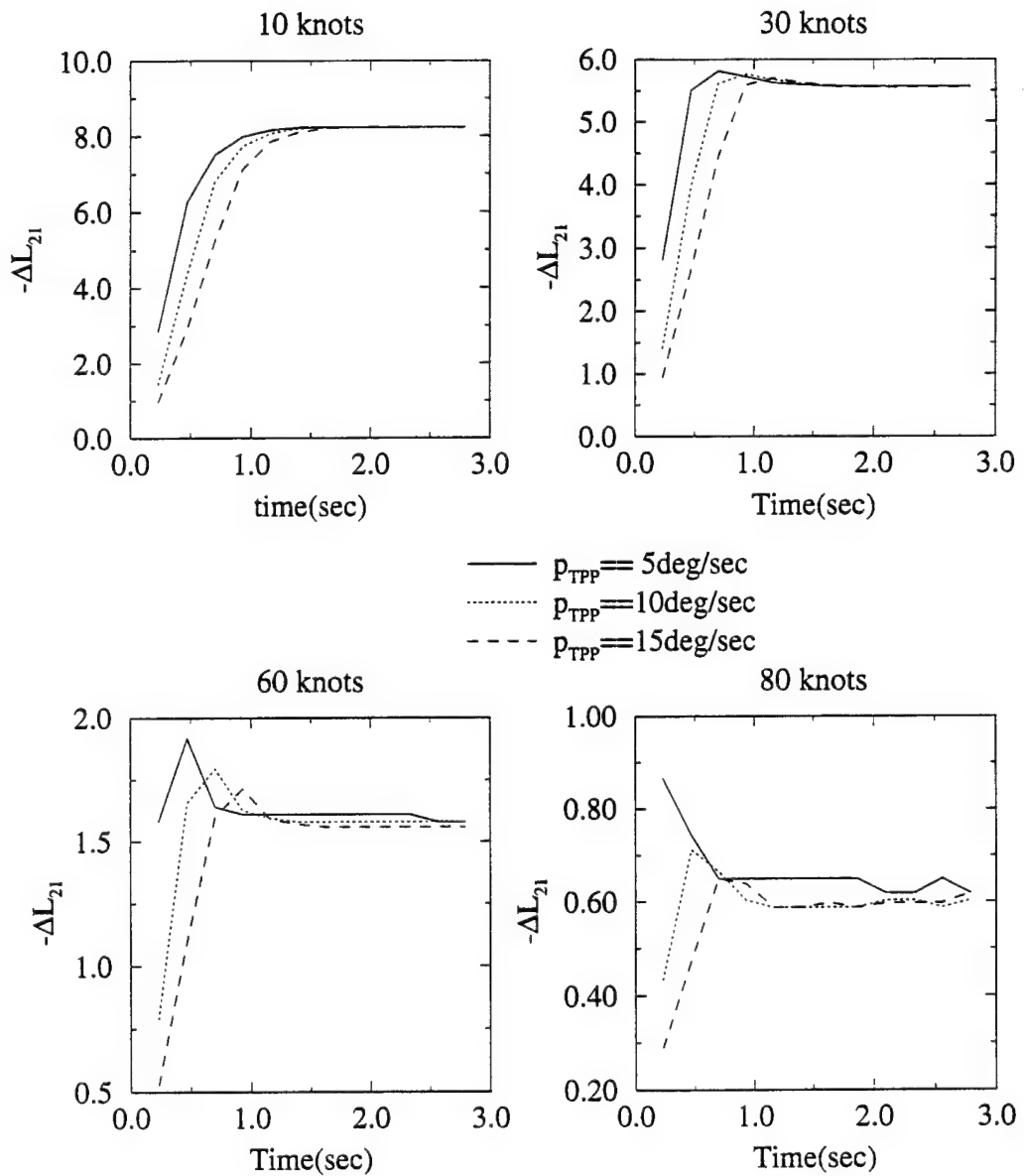


Figure 2.11: Side-to-side inflow influence coefficient due to roll in forward flight

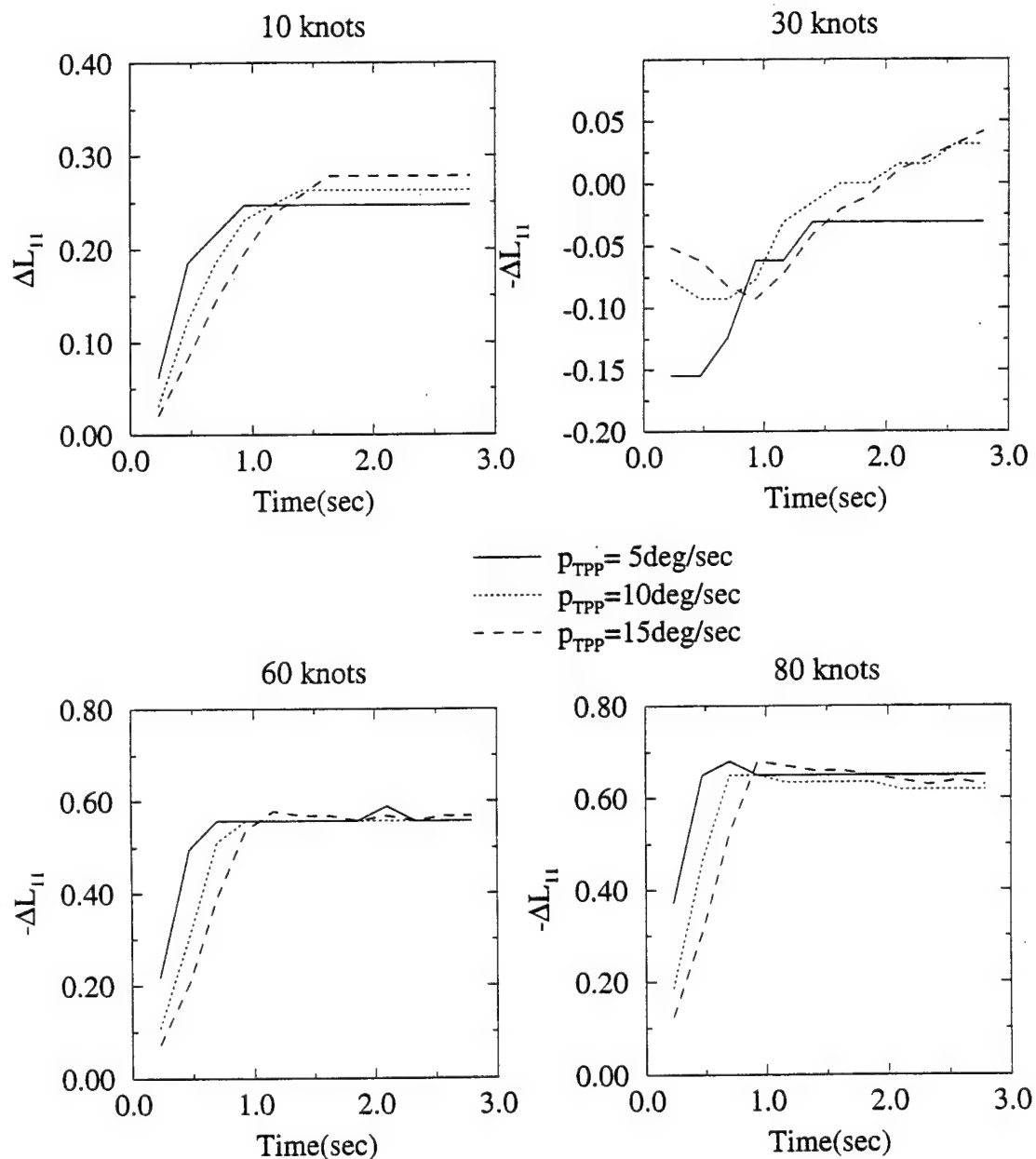


Figure 2.12: Fore-to-aft inflow influence coefficient due to roll in forward flight

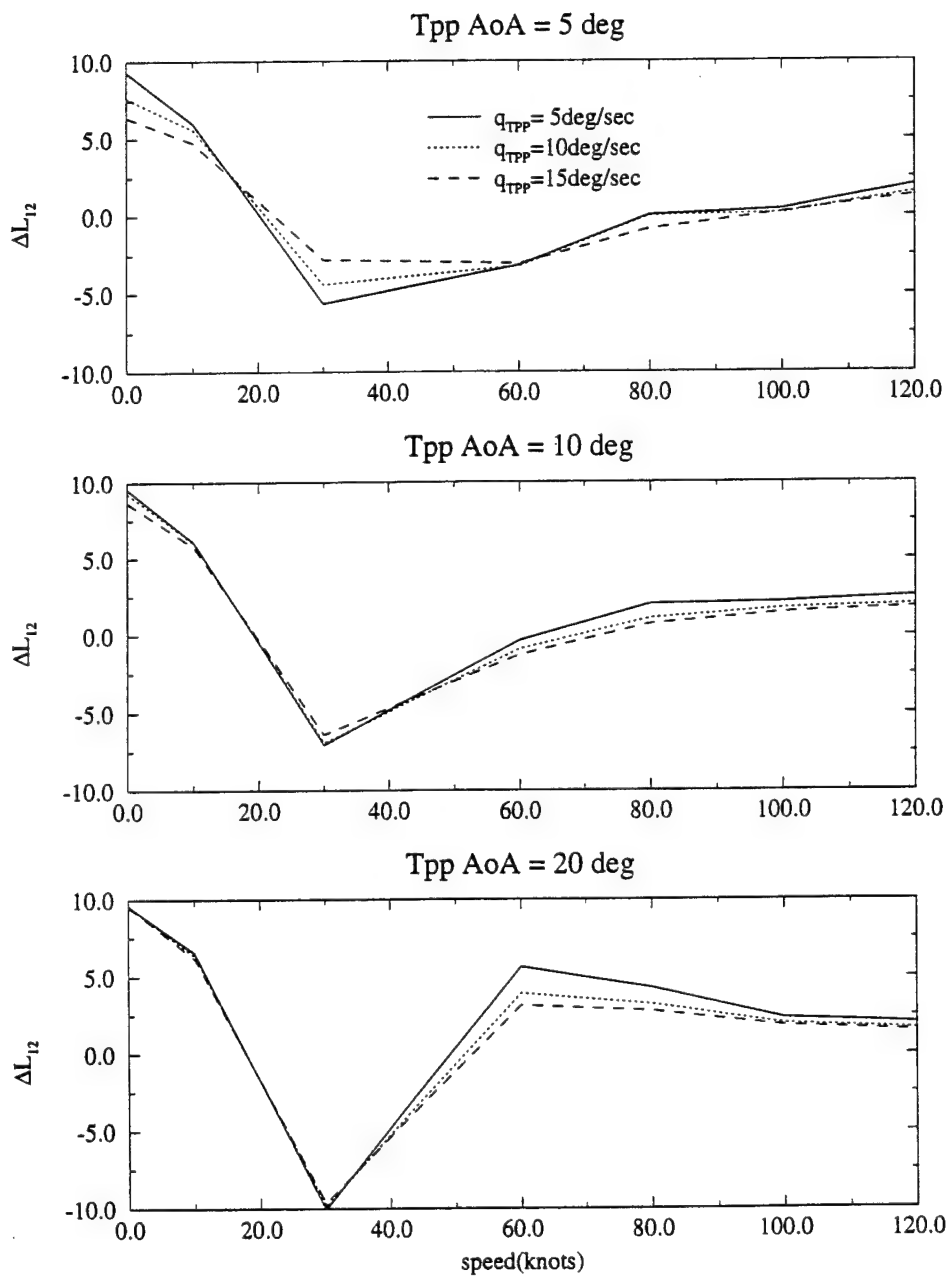


Figure 2.13: Variation of fore-to-aft inflow influence coefficient due to pitch with forward flight speed

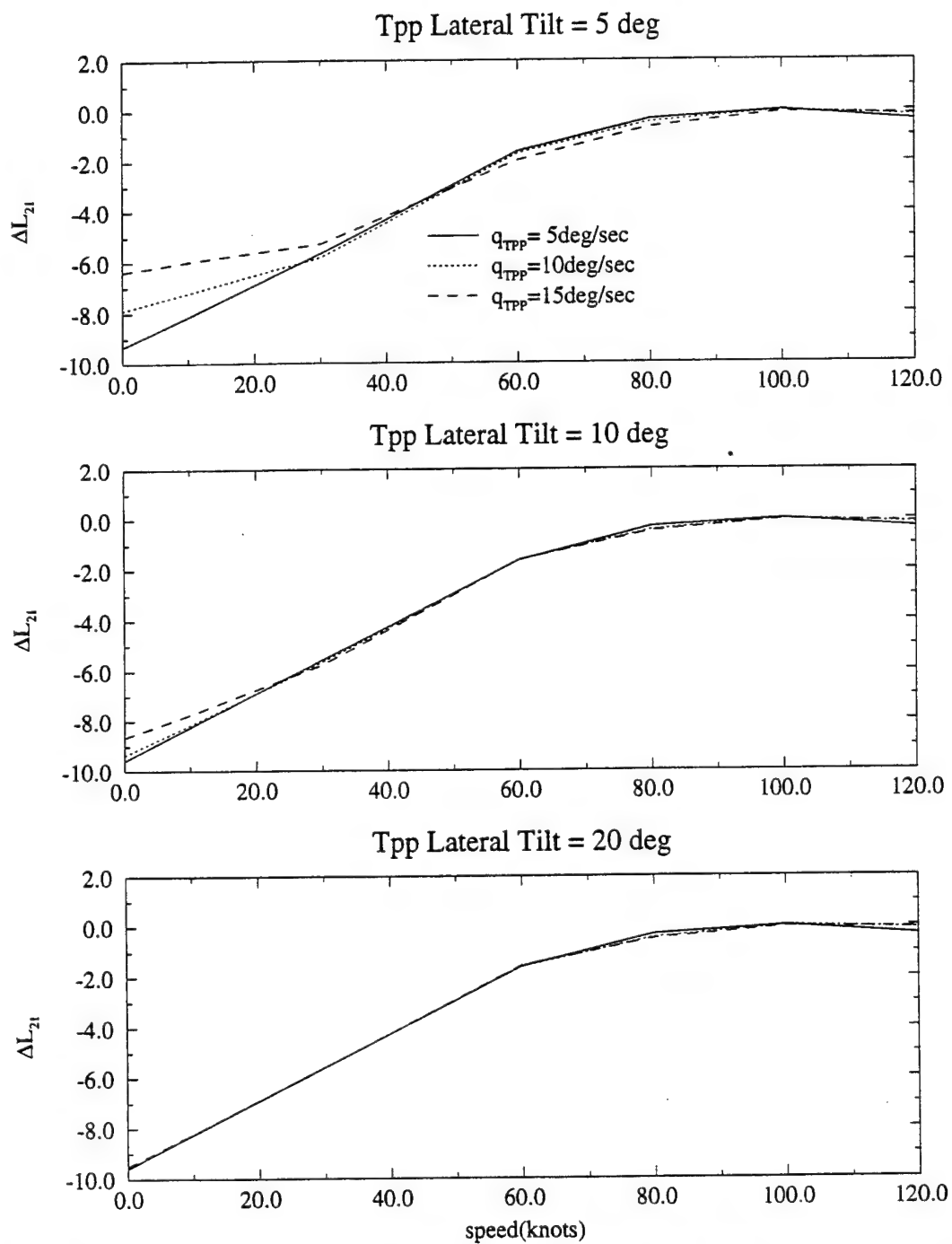


Figure 2.14: Variation of side-to-side inflow influence coefficient due to roll with forward flight speed

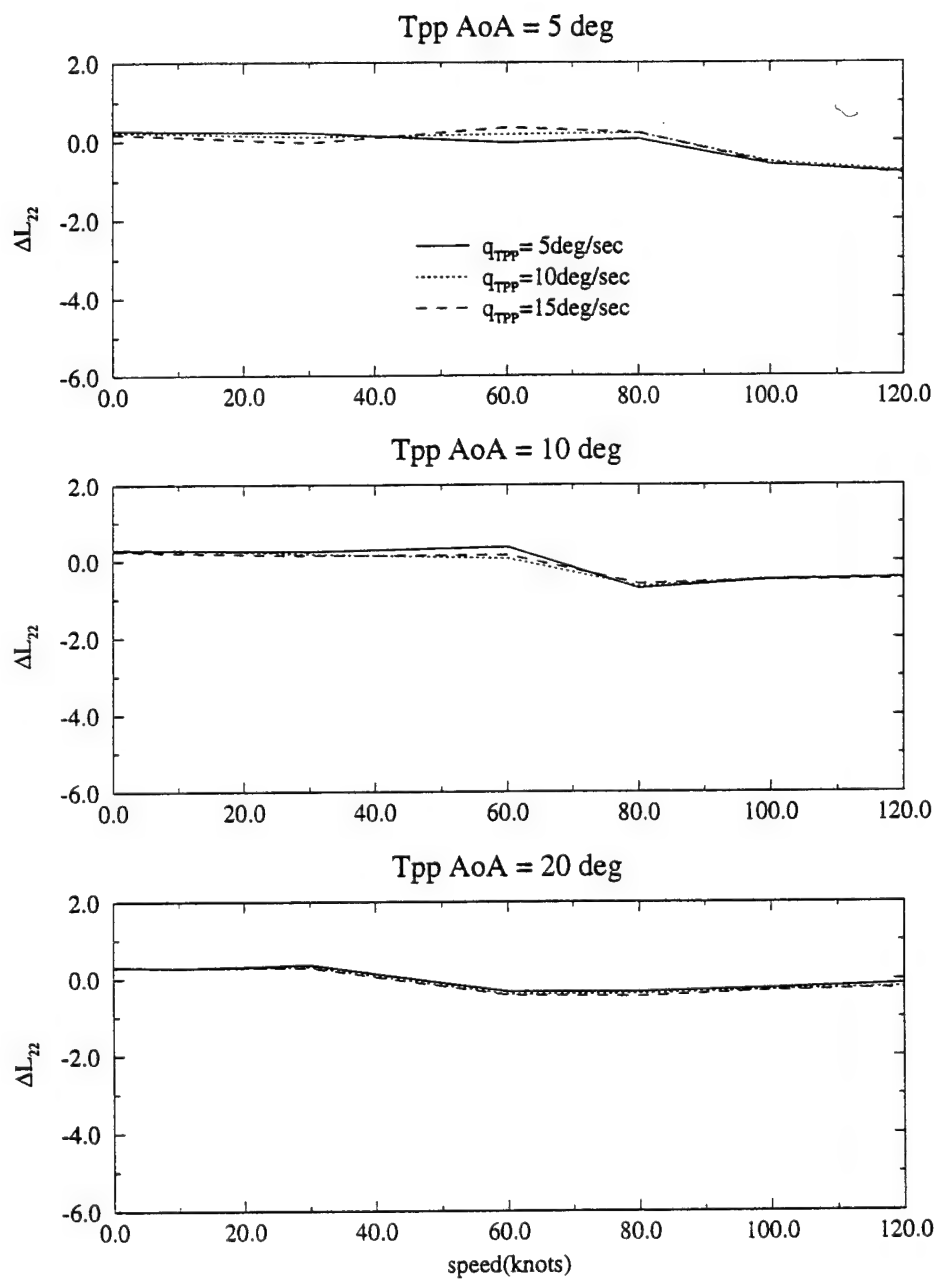


Figure 2.15: Variation of side-to-side inflow influence coefficient due to pitch with forward flight speed

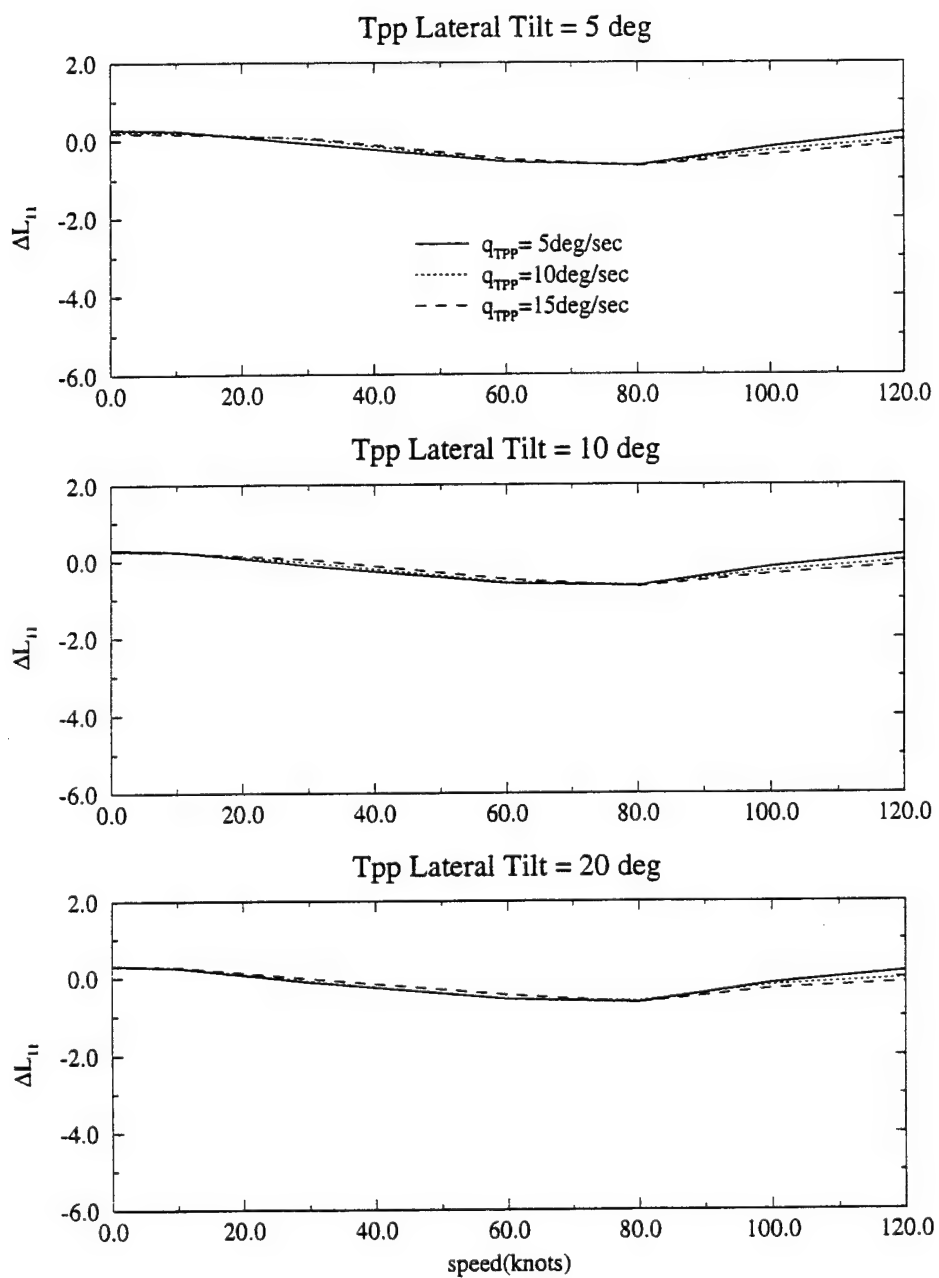


Figure 2.16: Variation of fore-to-aft inflow influence coefficient due to roll with forward flight speed

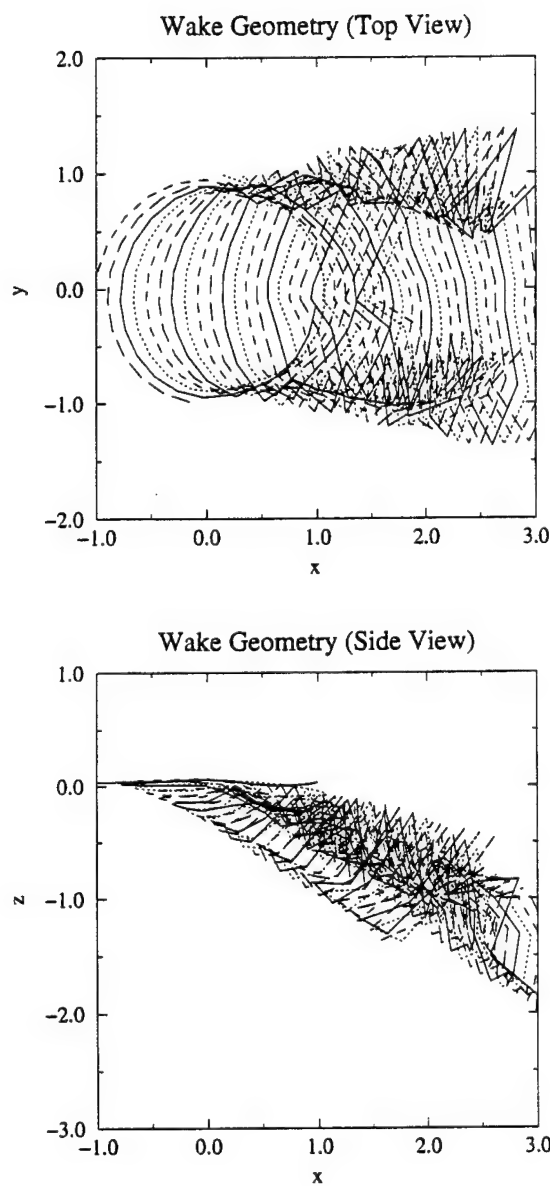


Figure 2.17: Illustration of rotor wake distortion in 30 Knots

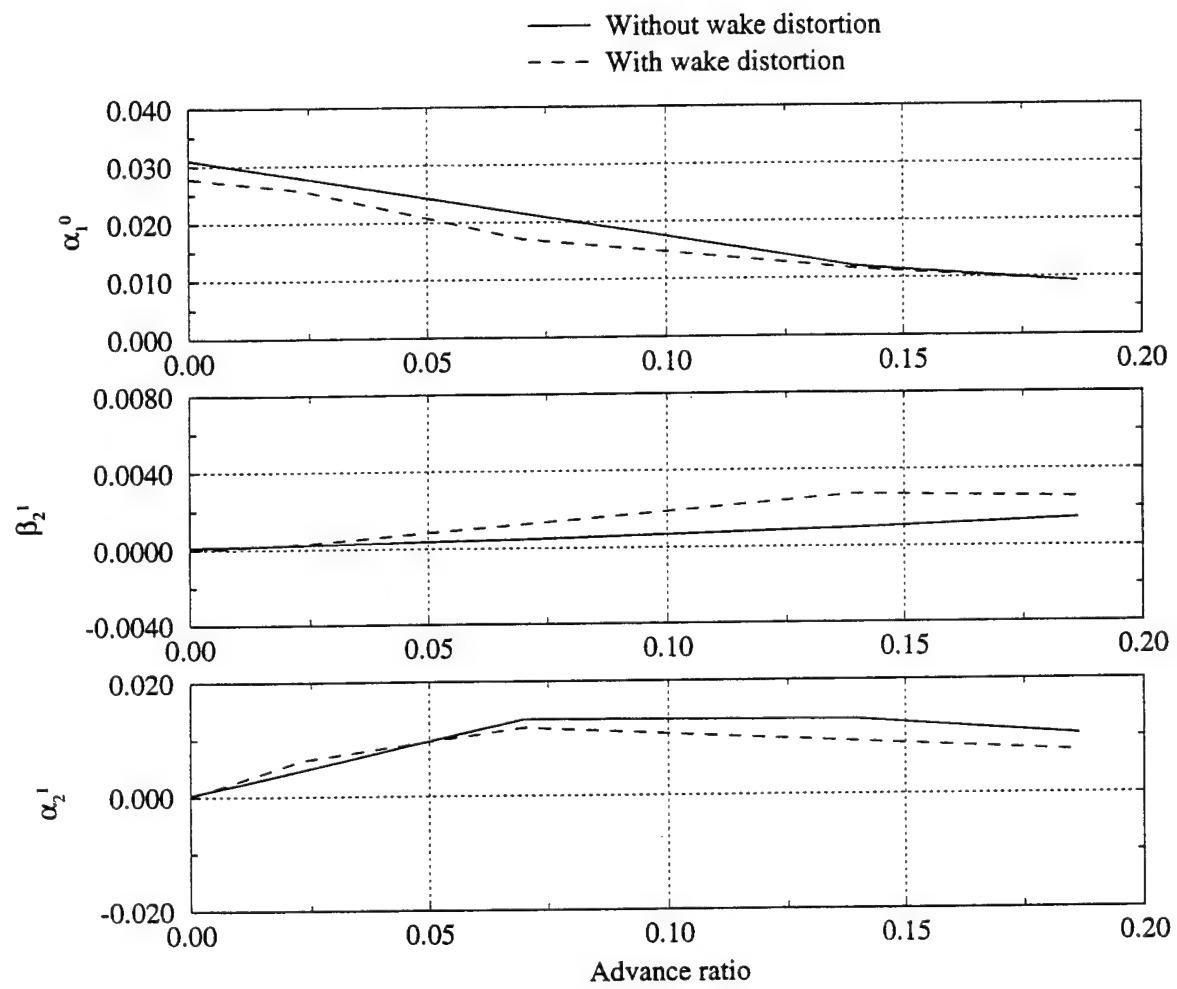


Figure 2.18: Averaged inflow states from distorted and undistorted wake

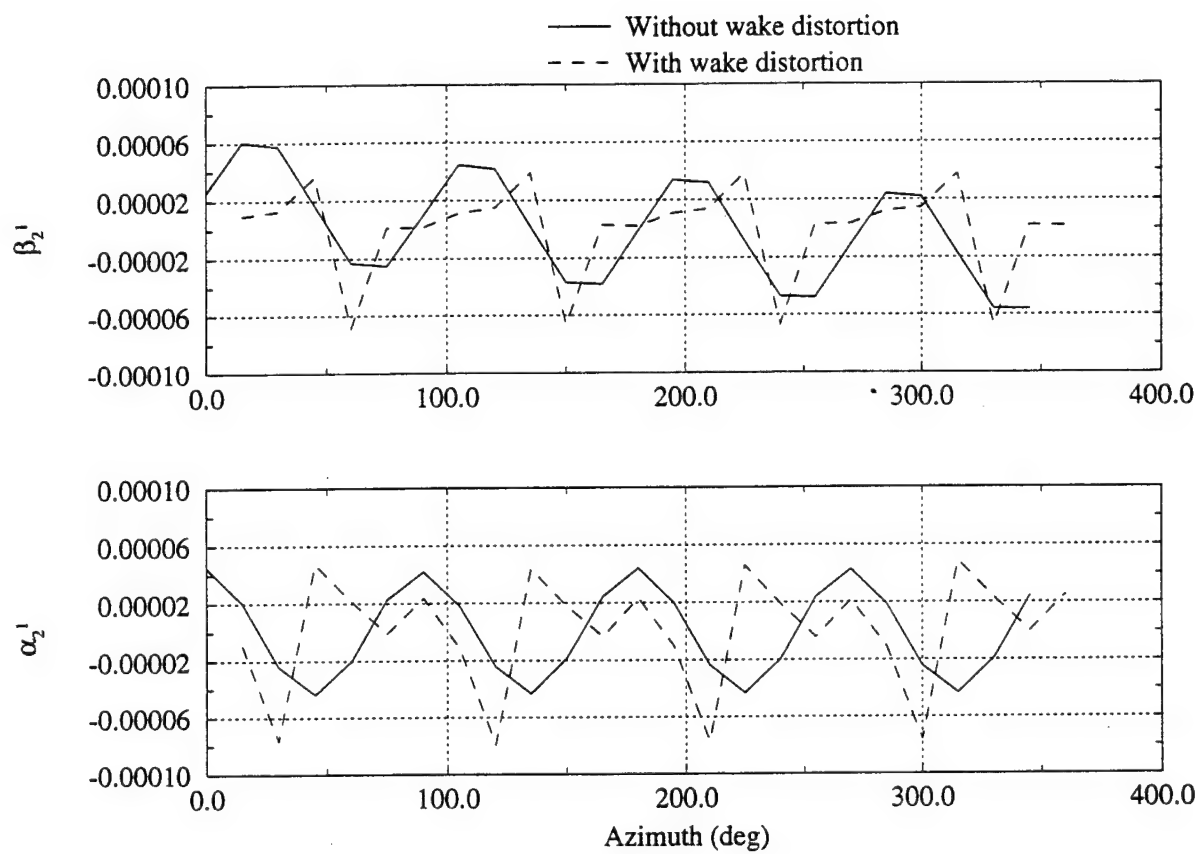


Figure 2.19: Oscillating inflow states from distorted and undistorted wake, 30 Knots

G.W. (lb) : 15870 F.S.C.G. (in) : 358.00 B.L.C.G. (in) : 0
Alt (ft) : 5587.52 Temp (deg C) : 3.77 Rotor RPM : 257.83
File : 201

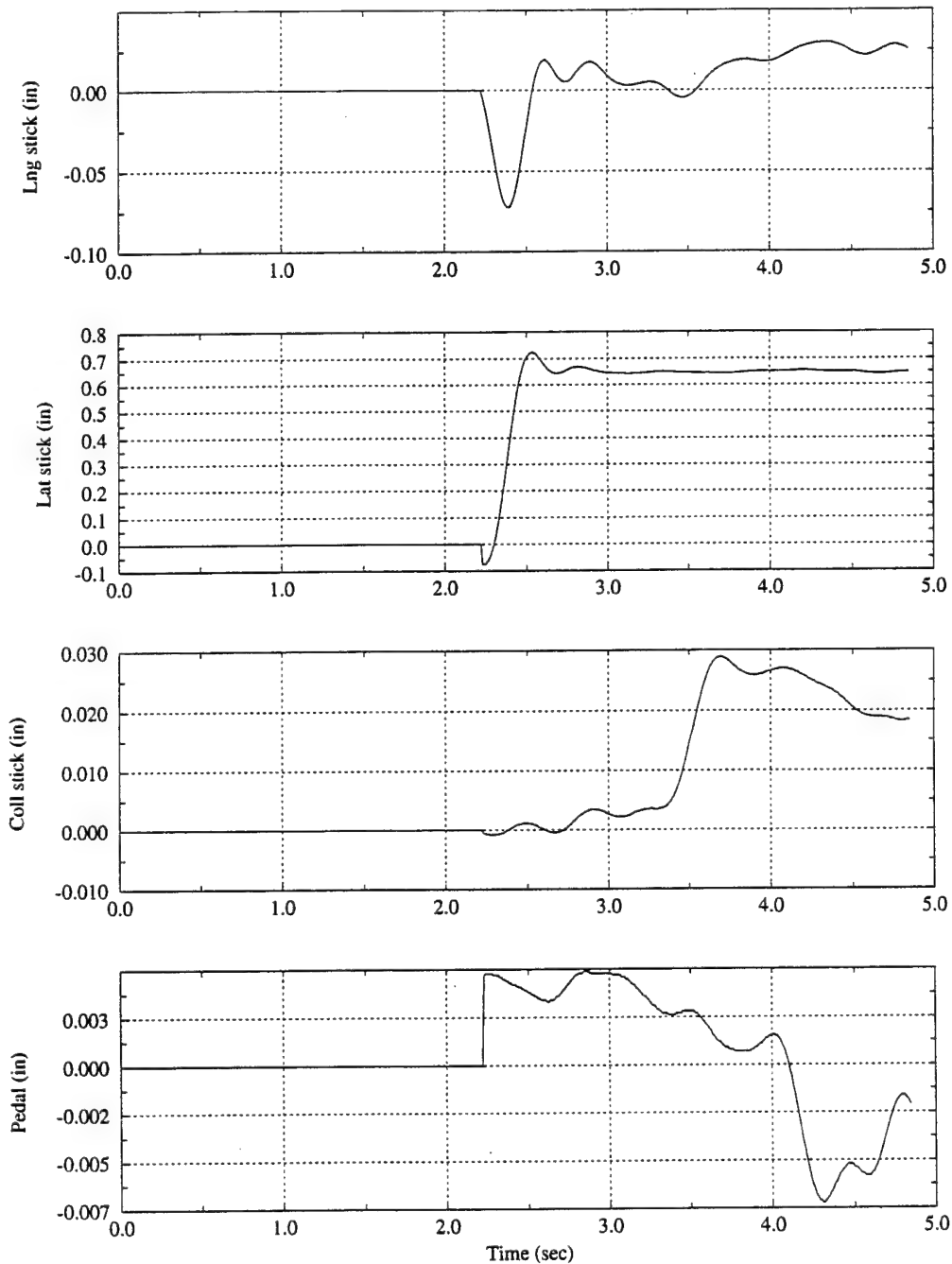


Figure 2.20: Pilot control stick inputs

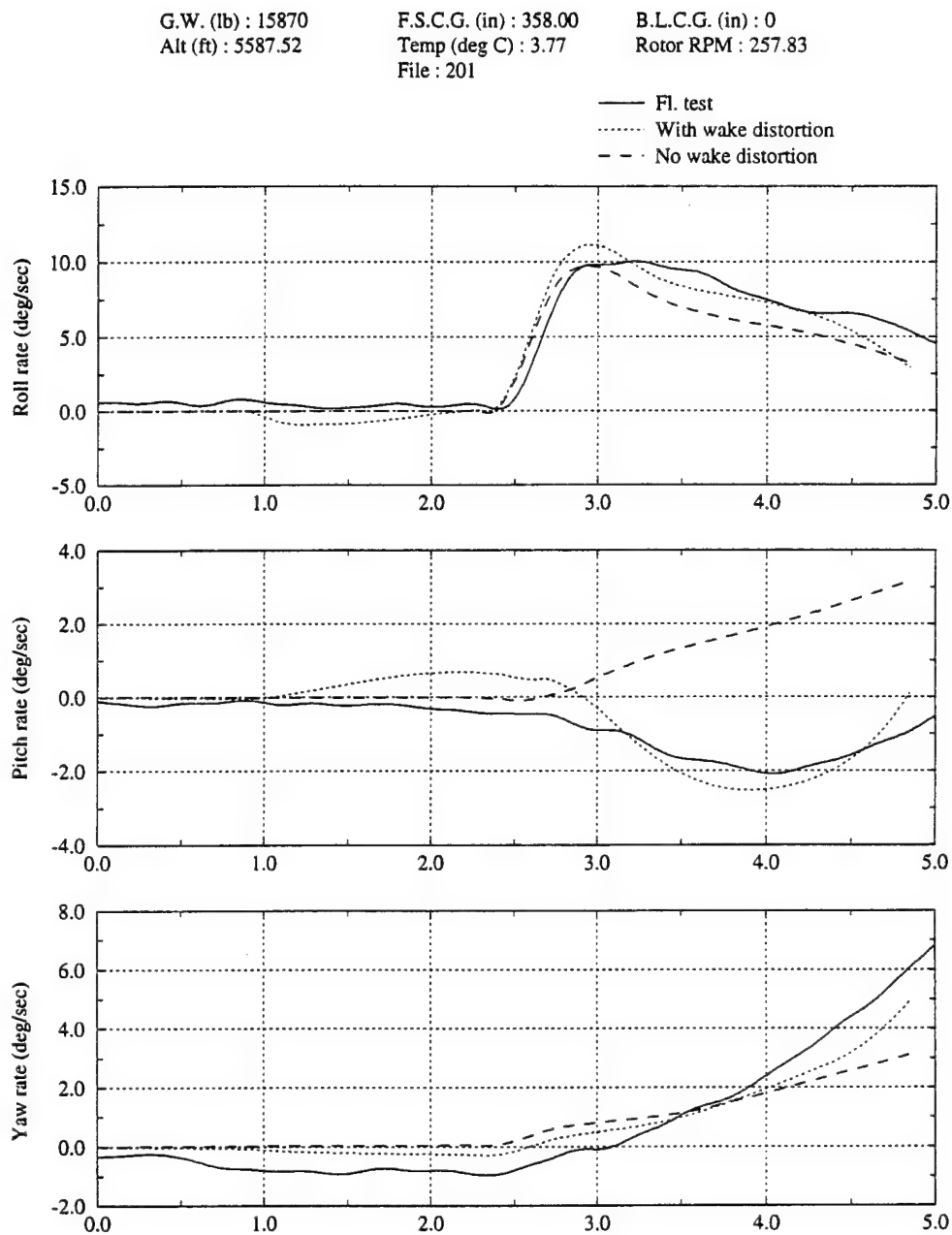


Figure 2.21: UH-60 body rotation rate response in hover

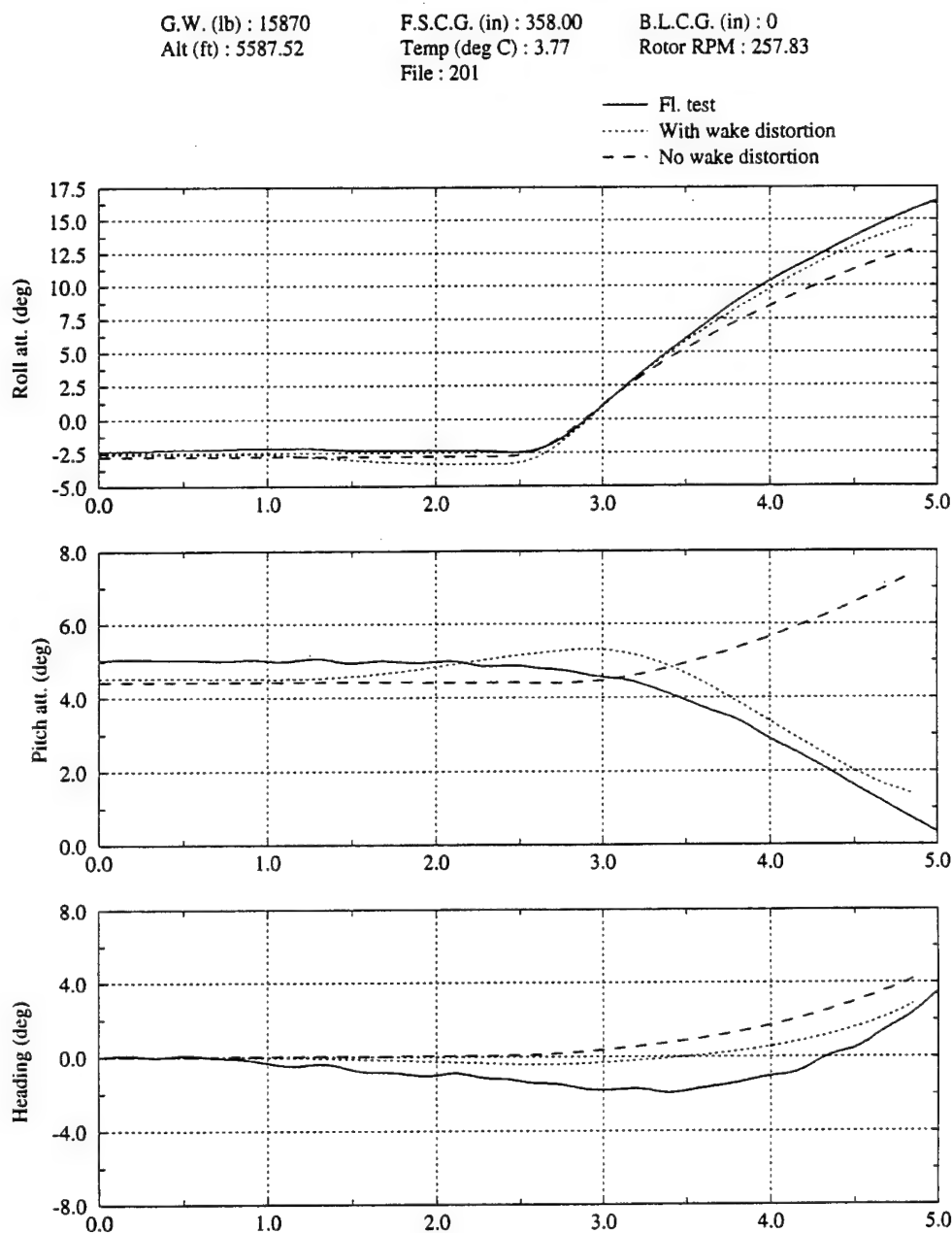


Figure 2.22: UH-60 body attitude response in hover

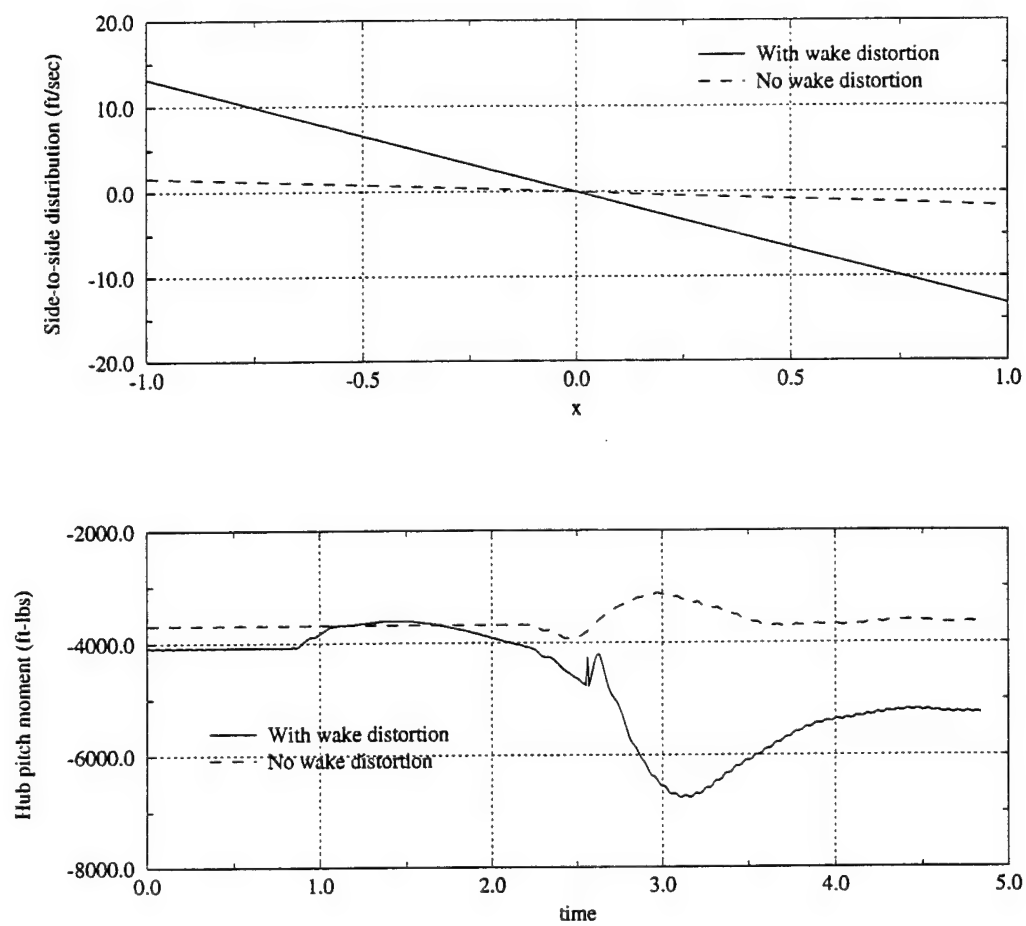


Figure 2.23: Effect of hub rotation on inflow and hub moment

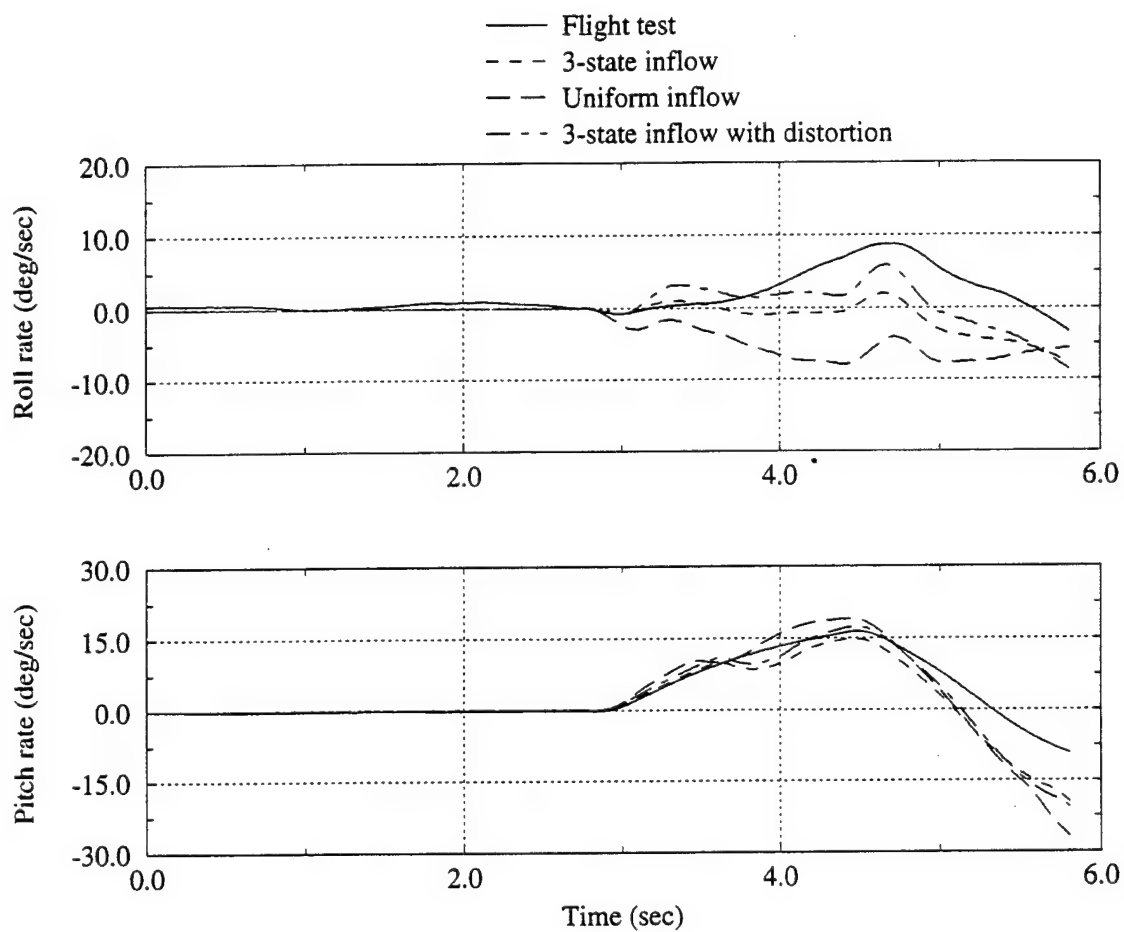


Figure 2.24: Wake distortion effect on off-axis response in 60 Knots

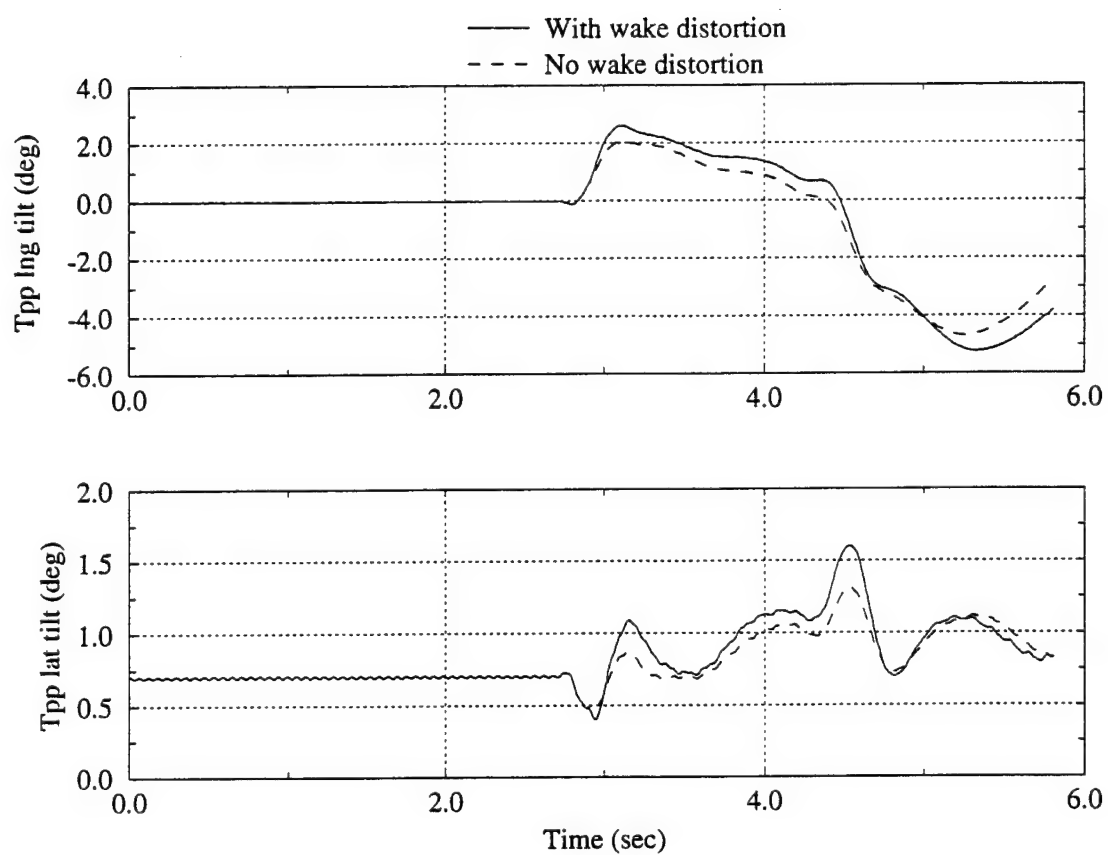


Figure 2.25: Wake distortion effect on rotor tip-path-plane in 60 Knots

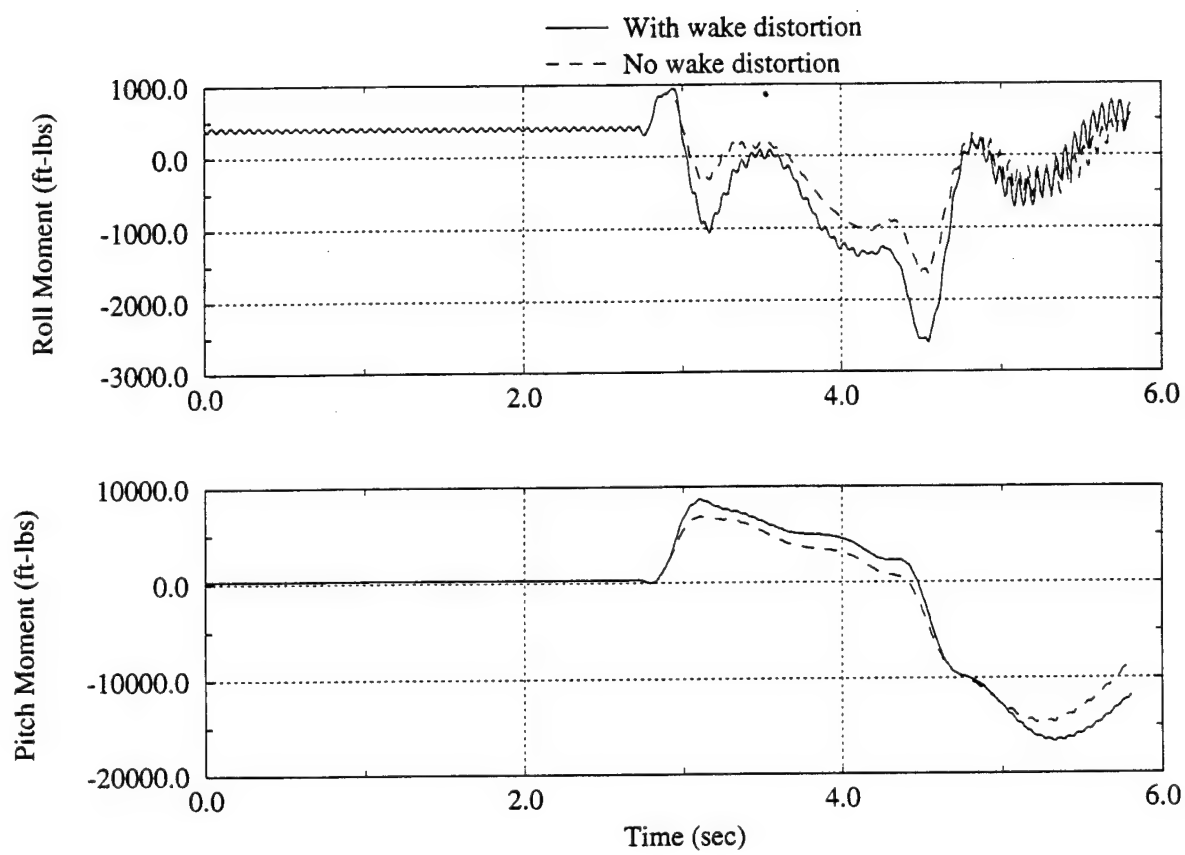


Figure 2.26: Wake distortion effect on hub moments in 60 Knots

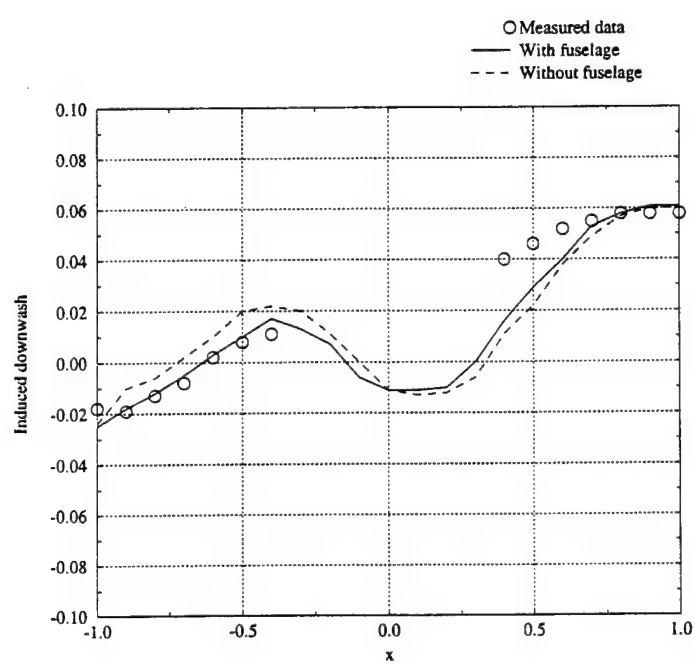


Figure 2.27: Fuselage induced downwash at rotor plane, $\mu = 0.15$

Chapter 3

Finite State Inflow Interference

Including the tip vortex distortion in finite state dynamic wake formulation improves the prediction of pitch-roll cross axis coupling. There is another class of off-axis coupling phenomena associated with aerodynamic interference. For example, there is a pitch response from sideslip due to the asymmetric distribution of main rotor downwash over the horizontal tail surfaces. Unfortunately, the aerodynamic interference is another poorly modeled phenomena in rotocraft simulations. Most flight simulation programs at the present time use simple momentum estimation models, or rely on crude empirical models or table look-ups for specific vehicles.

The simple models do not provide enough fidelity to generate an acceptable simulation. The empirical models or table look-up methods are limited to a specific helicopter and can't include transient dynamic effects. The vortex wake models, Refs. [17] to [20], on the other hand, are time consuming and have limitations in modeling maneuvering flight. Calculation of the aerodynamic interference from the finite state dynamic wake model, Refs. [30] to [32], provides a solution to the problems. The finite state dynamic wake model has the sophistication of the vortex wake for modeling accuracy and is applicable in transient flight. At the same time, it offers efficiency in satisfying the stringent computational demand of flight simulation. Moreover, the finite-state modeling of complicated rotor wake dynamics presents a solution format that is consistent with all existing flight dynamics formulations. The finite-state induced flow model was first developed to compute normal induced velocity at the rotor plane. But, the inflow solution has been limited at the rotor plane and can't be used for interference modeling. A natural and beneficial step is to enhance the rotor finite state wake modeling capability to calculate the rotor induced velocity at any arbitrary point in the flowfield. This provides solutions for main rotor interference effects on the tail rotor, fuselage, and tail aerodynamic surfaces (vertical fin and horizontal surface). In a previous effort, we have developed a basic formulation for the finite state rotor interference solution. Here the rotor inflow interference model is further made to work under the finite state dynamic wake model enhanced with the wake distortion. We have also performed validation of the finite state rotor interference

model and investigated its effects on rotorcraft trim and response.

3.1 Formulation

From the basic equations presented in the previous section, the induced velocity at an arbitrary flow field point can be attained through an integration of Eq. (2.6). This gives

$$q_i = -\frac{1}{V_T} \int_{\xi}^{\infty} \Phi_{,i}^V d\xi \quad (3.1)$$

This relationship is derived in the relative-wind frame $(x_{\xi}, y_{\xi}, z_{\xi})$, Figure 3.1, but it is also true in the wind-hub reference frame (x_w, y_w, z_w) because of the linear transformation relationship between the two frames,

$$\begin{Bmatrix} x_{\xi} \\ y_{\xi} \\ z_{\xi} \end{Bmatrix} = \begin{bmatrix} \cos\alpha & 0 & -\sin\alpha \\ 0 & 1 & 0 \\ \sin\alpha & 0 & \cos\alpha \end{bmatrix} \begin{Bmatrix} x_w \\ y_w \\ z_w \end{Bmatrix} \quad (3.2)$$

3.1.1 Partial Derivative Relationship

Since the solution of the pressure function Φ^V is expressed in ellipsoidal coordinates, Fig. 2.1, the calculation of induced velocity by Eq. (3.1) needs an application of the chain rule for the evaluation of $\Phi_{,i}^V$. In the following, a matrix of first partial derivatives between the ellipsoidal coordinates and wind-hub coordinates are derived.

If we denote the x_w^i as index representation of wind-hub coordinates and x_{ν}^j as the index notation of ellipsoidal coordinates, we have $\partial x_w^1 / \partial x_{\nu}^1 = \partial x_w / \partial \nu$, $\partial x_w^1 / \partial x_{\nu}^2 = \partial x_w / \partial \eta$, \dots , $\partial x_w^2 / \partial x_{\nu}^3 = \partial y_w / \partial \bar{\psi}$, and etc.. Thus, we have

$$\left[\frac{\partial x_w^j}{\partial x_{\nu}^i} \right] = \left[\frac{\partial x_w^i}{\partial x_{\nu}^j} \right]^{-1} \quad (3.3)$$

This can be further written as

$$\begin{aligned} \left[\frac{\partial x_w^j}{\partial x_{\nu}^i} \right] &= \begin{bmatrix} \partial \nu / \partial x_w & \partial \nu / \partial y_w & \partial \nu / \partial z_w \\ \partial \eta / \partial x_w & \partial \eta / \partial y_w & \partial \eta / \partial z_w \\ \partial \bar{\psi} / \partial x_w & \partial \bar{\psi} / \partial y_w & \partial \bar{\psi} / \partial z_w \end{bmatrix} \\ &= \begin{bmatrix} -\frac{\nu \cos \bar{\psi}}{s_2} s_1 & -\frac{\nu \sin \bar{\psi}}{s_2} s_1 & \frac{\eta(1-\nu^2)}{s_2} \\ \frac{\eta \cos \bar{\psi}}{s_2} s_1 & \frac{\eta \sin \bar{\psi}}{s_2} s_1 & \frac{\nu(1-\eta^2)}{s_2} \\ -\frac{\sin \bar{\psi}}{s_1} & \frac{\cos \bar{\psi}}{s_1} & 0 \end{bmatrix} \end{aligned} \quad (3.4)$$

where $s_1 = \sqrt{(1+\eta^2)(1-\nu^2)}$ and $s_2 = \nu^2 + \eta^2$

We also have the relationship between the hub-wind and relative wind coordinates, Fig. 3.1.

$$\left[\begin{array}{c} \frac{\partial x_w^i}{\partial x_\xi^j} \end{array} \right] = \left[\begin{array}{ccc} \cos\alpha & 0 & \sin\alpha \\ 0 & 1 & 0 \\ -\sin\alpha & 0 & \cos\alpha \end{array} \right] \quad (3.5)$$

where x_ξ^j represent relative wind coordinates.

3.1.2 Gradient of Pressure Function

The pressure function, Eq. (2.11), is attained in the ellipsoidal coordinates. For induced velocity calculation, we need the gradient of the pressure function with respect to the relative wind frame and wind-hub frame.

Applying the chain rule, we attain the gradient of the pressure function with respect to the relative wind frame.

$$\left\{ \begin{array}{c} \frac{\partial \Phi^V}{\partial x_\xi^i} \\ \frac{\partial \Phi^V}{\partial y_\xi^i} \\ \frac{\partial \Phi^V}{\partial z_\xi^i} \end{array} \right\} = \left[\begin{array}{c} \frac{\partial x_w^i}{\partial x_\xi^j} \end{array} \right]^T \left[\begin{array}{c} \frac{\partial x_w^i}{\partial x_w^j} \end{array} \right]^T \left\{ \begin{array}{c} \frac{\partial \Phi^V}{\partial x_w^i} \\ \frac{\partial \Phi^V}{\partial y_w^i} \\ \frac{\partial \Phi^V}{\partial z_w^i} \end{array} \right\} \quad (3.6)$$

Similarly, the gradient of the pressure function with respect to the wind-hub frame can be obtained as

$$\left\{ \begin{array}{c} \frac{\partial \Phi^V}{\partial x_w^i} \\ \frac{\partial \Phi^V}{\partial y_w^i} \\ \frac{\partial \Phi^V}{\partial z_w^i} \end{array} \right\} = \left[\begin{array}{c} \frac{\partial x_\psi^i}{\partial x_w^j} \end{array} \right]^T \left\{ \begin{array}{c} \frac{\partial \Phi^V}{\partial x_\psi^i} \\ \frac{\partial \Phi^V}{\partial y_\psi^i} \\ \frac{\partial \Phi^V}{\partial z_\psi^i} \end{array} \right\} \quad (3.7)$$

Integration of the pressure gradient along the free stream line results in all three components of the induced velocity associated with lifting rotors. The results are given in the following section.

3.1.3 Three Components of Induced Velocity

To calculate all three components of the induced velocity at an arbitrary flowfield point, the integrations of the spatial derivatives of the pressure function need to be performed. Based on the finite state dynamic wake theory, these integrals are the functions of the geometric relationship between the rotor and the flowfield point of interest for interference. The induced velocities thus obtained are both nonuniform and unsteady. Moreover, the interference model can be truncated at various frequency ranges in the interest of different applications.

To make use of the computational advantage of using wind-hub or relative wind reference frames, we like to express the induced velocity calculations in both of those frames. In rotorcraft analysis and simulation applications, these induced velocities are then, in general, transformed to the nonrotating-hub frame, and further expressed

in the local frame attached at each aerodynamic panel. The transformations to the nonrotating hub frame can be accomplished through the frame relationships.

x_ξ -Component

The x -component of the induced velocity component is calculated in the relative-wind frame due to the availability of the analytical closed form. From Eq. (3.1), we have

$$q_{x_\xi} = \frac{1}{V_T} \int_{\xi}^{\infty} \Phi_{,\xi}^V d\xi \quad (3.8)$$

Outside the rotor wake, Φ^V is continuous, and $\Phi^V|^\infty$ tends to zero. Therefore

$$q_{x_\xi}(x_\xi, y_\xi, z_\xi) = -\frac{1}{V_T} \Phi^V(x_\xi, y_\xi, z_\xi) \quad (3.9)$$

Inside the wake, Φ^V is discontinuous wherever the integration crosses the rotor plane. Then

$$\begin{aligned} q_{x_\xi} = & \frac{1}{V_T} [\Phi^V(x_\xi|_{\xi=0^-}, y_\xi, z_\xi|_{\xi=0^-}) \\ & - \Phi^V(x_\xi|_{\xi=0^+}, y_\xi, z_\xi|_{\xi=0^+}) \\ & - \Phi^V(x_\xi, y_\xi, z_\xi)] \end{aligned} \quad (3.10)$$

In numerical computation, a finite value denoted as ϵ needs to be used for the 0^- or 0^+ . This value is designated as the "singularity clearance distance" in the numerical implementation of the theory. This number may be seen as an equivalence of the conventional vortex core size. In fact, it physically refers to the discontinuity of the pressure across the rotor plane.

y_w -Component

To reduce one level of transformation from the relative wind frame to the wind-hub frame, the y -component of induced velocity is calculated in the wind-hub frame. From Eqs. (3.1 and 3.5), we have

$$q_{y_w} = -\frac{1}{V_T} \int_{\xi}^{\infty} \Phi_{,y_w}^V d\xi \quad (3.11)$$

Although the induced velocity component is expressed in the wind-hub frame, it should be kept in mind that the integration is performed along the free stream line.

Substituting Eq. (2.11) into Eq. (3.11), the y_w -component of induced velocity can be obtained as

$$q_{y_w} = \frac{1}{2V_T} \sum_m^{\infty} \sum_n^{\infty} (q_{y_w n}^{mc} \tau_n^{mcV} + q_{y_w n}^{ms} \tau_n^{msV}) \quad (3.12)$$

where the $q_{y_w n}^{mc}$ and $q_{y_w n}^{ms}$ are the induced flow influence coefficients and are related to each specific distribution of the pressure function. They are

$$q_{y_w n}^{mc} = \int_{\xi}^{\infty} \frac{\partial}{\partial y_w} [\bar{P}_n^m(\nu) \bar{Q}_n^m(i\eta) \cos(m\bar{\psi})] d\xi \quad (3.13)$$

$$q_{y_w n}^{ms} = \int_{\xi}^{\infty} \frac{\partial}{\partial y_w} [\bar{P}_n^m(\nu) \bar{Q}_n^m(i\eta) \sin(m\bar{\psi})] d\xi \quad (3.14)$$

The derivatives of the associated Legendre functions with respect to the wind-hub coordinates can be obtained through chain rule.

$$\frac{\partial \bar{P}_n^m(\nu)}{\partial y_w} = \frac{d\bar{P}_n^m(\nu)}{d\nu} \frac{\partial \nu}{\partial y_w} \quad (3.15)$$

$$\frac{\partial \bar{Q}_n^m(i\eta)}{\partial y_w} = \frac{d\bar{Q}_n^m(i\eta)}{d\eta} \frac{\partial \eta}{\partial y_w} \quad (3.16)$$

$$\frac{\partial \cos(m\bar{\psi})}{\partial y_w} = -m \sin(m\bar{\psi}) \frac{\partial \bar{\psi}}{\partial y_w} \quad (3.17)$$

$$\frac{\partial \sin(m\bar{\psi})}{\partial y_w} = m \cos(m\bar{\psi}) \frac{\partial \bar{\psi}}{\partial y_w} \quad (3.18)$$

z_w -Component

Taking derivative of the pressure function in the z_w direction and integrating along ξ , we have

$$q_{z_w} = -\frac{1}{V_T} \int_{\xi}^{\infty} \Phi_{,z_w}^V d\xi \quad (3.19)$$

Substituting Eq. (2.11) into Eq. (3.19), the z_w -component of induced velocity is attained as

$$q_{z_w} = \frac{1}{2V_T} \sum_m^{\infty} \sum_n^{\infty} q_{z_w n}^{mc} \tau_n^{mcV} + q_{z_w n}^{ms} \tau_n^{msV} \quad (3.20)$$

where the $q_{z_w n}^{mc}$ and $q_{z_w n}^{ms}$ are the induced flow influence coefficients and can be calculated from each distribution of the pressure function.

$$q_{z_w n}^{mc} = \int_{\xi}^{\infty} \frac{\partial}{\partial z_w} [\bar{P}_n^m(\nu) \bar{Q}_n^m(i\eta) \cos(m\bar{\psi})] d\xi \quad (3.21)$$

$$q_{z_w n}^{ms} = \int_{\xi}^{\infty} \frac{\partial}{\partial z_w} [\bar{P}_n^m(\nu) \bar{Q}_n^m(i\eta) \sin(m\bar{\psi})] d\xi \quad (3.22)$$

As formulated in the previous sections, the pressure distribution coefficients, (τ_n^{mcV} and τ_n^{msV}) are needed in the calculation of the rotor induced velocity at arbitrary flowfield points. These pressure distribution coefficients are obtained from the rotor solutions, Eqs. 2.29 and 2.30

3.2 Results and Discussion

The following sections examine the induced velocity computed from the finite state dynamic wake interference model and investigates its effects on helicopter trim and control responses.

3.2.1 Induced Flowfield

The main rotor induced velocity at the empennage (horizontal and vertical surfaces) are computed for the UH-60 helicopter at 86 Knots, Figs. 3.2 and 3.3. The results are also compared with the predictions of a 'flat' prescribed wake model, Ref. [45], and free wake model, Ref. [15]. Figure 3.2 is the predictions of the induced velocity distribution at the location of the horizontal stabilizer of UH-60 helicopter at $\mu = 0.2$ and $C_T = 0.007$. The induced inplane, sidewash, and normal components shown in the rotor hub frame are normalized by the main rotor uniform downwash at the rotor plane. The UH-60 horizontal surface has a full span of about $0.5R$. The finite state wake model prediction has a close agreement with the free wake model, Ref. [15]. The well established fact that the downwash at the advancing side is stronger than at the retreating side is well predicted by all the three models. But, the flat wake model overestimates about 30% of the peak in both the sidewash and normal components. There is no data available from the free wake model, Ref. [15], for the inplane component prediction. Comparing the flat wake and finite state wake models, the former underestimates the inplane component. But, for the calculation of airloads on the horizontal stabilizer, only the normal induced velocity is of significance. Although there is no direct experimental data for correlation, the induced flow distribution predicted here, in general, compares well with the experimental pattern as shown in Ref. [45].

The induced velocity distribution at the vertical tail location is presented in Figure 3.3. Of the three velocity components, the sidewash component directly changes the angle of attack of the tailplane, and thus has a much larger effect on the tailplane aerodynamics than the other two velocity components. Only the sidewash data is available from Ref. [15] for comparison. It is seen that the finite state wake results closely agree with those of vortex wake models. There is a slight shift at the crossover where the sidewash changes its direction. This is probably due to either the inconsistency in the vertical fin location between the two calculations or the trim setting

difference.

One of the distinctive features of the finite state rotor wake model is its capability to predict the unsteady and nonuniform interference induced velocity. The interference solution from the finite state dynamic wake provides both the time averaged induced flow effect and the unsteady time variation of the induced velocity on the impinged aerodynamic surfaces. A good example for understanding this effect is to consider a trailing vortex with time varying strength from the main rotor that takes time to reach the aerodynamic surface and then passes it. This would create a time varying history of the wake induced velocity on the aerodynamic surface. Thus, its impact will affect both the magnitude and phase of the helicopter responses. The modeling of this unsteady wake effect is a significant step toward the improvement of the fidelity of rotorcraft flight simulations.

Figure 3.4 is the time-varying induced velocity at the fuselage aerodynamic center and the horizontal tail location at 40 Knots and 80 Knots forward flight speeds. The induced velocity varies at a frequency of 4/rev corresponding to the number of rotor blades.

3.2.2 Effects on Helicopter Trim

The effects of rotor interference on the helicopter trim are examined in Fig. 3.5 where the trim results for the UH-60 helicopter in level forward flight are shown. The comparison of the helicopter trim is made with and without the main rotor wake interference. As seen, the main rotor interference is most significant at forward flight speeds around 40 Knots. It is found that the large change in the longitudinal stick position and helicopter pitch attitude is due to the impingement of main rotor wake on the horizontal tail. Figure 3.5 also compares the trim results of the three state inflow interference model with the empirical interference, Ref. [46]. A close agreement for most control channels and fuselage attitudes between the two interference models is obtained. A discrepancy is noticed for the longitudinal control. More forward longitudinal stick is required for the finite state wake interference than for the empirical interference. This discrepancy is improved when a six state dynamic wake interference is used.

3.2.3 Effects on Helicopter Response

The UH-60 response at 60 Knots to a one inch aft longitudinal stick is examined in Fig. 3.6. The prediction of the vehicle response from three models are presented and compared with flight test data. The first model uses 3-state induced inflow with its interference on the fuselage, horizontal, vertical tails and the tail rotor. The second model uses a uniform inflow state and its interference. Between the uniform inflow model and the 3-state inflow model, there are differences in both the interference modeling and main rotor aerodynamics. To examine the interference effect, the results

from another model that uses the 3-state inflow model for the main rotor, but allows for interference from the uniform inflow state is also presented for comparison. In the last model, the interference effect is related to the rotor thrust only. No effect of rotor hub moments on the interference is considered.

Compared to the uniform main rotor inflow model, the 3-state inflow model improves correlation in both the on-axis (pitch rate) and off-axis responses. The interference effect on the yaw response is remarkable. The 3-state inflow with interference model has the best agreement with the flight test data, Ref. [47].

Examining the interference velocity at the tail rotor, Fig. 3.7, reveals a large variation in the sidewash induced flow component predicted by the 3-state inflow interference model. This variation can not be present in a table look-up method due to the dynamic change of relative position between the main rotor wake and interference location during the maneuvering flight.

The variation of this sidewash induced velocity has a significant impact on the changes in the angle of attack of tail rotor blade sections. The angle of attack changes further result in a corresponding variation in the yaw torque that the tail rotor applies at the helicopter center of gravity, Fig. 3.7.

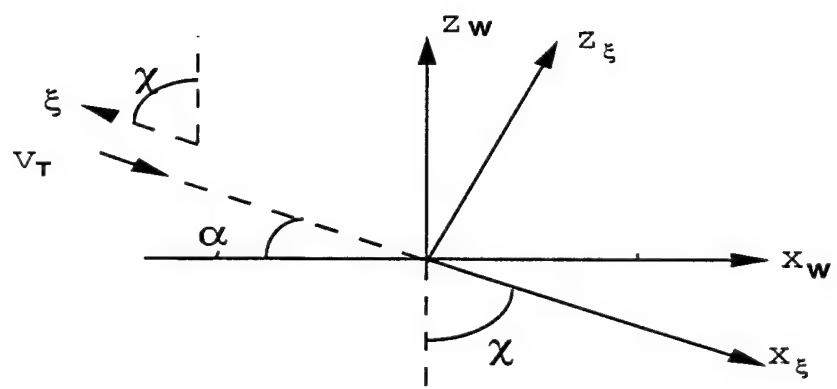


Figure 3.1: Relative wind and wind-hub coordinates

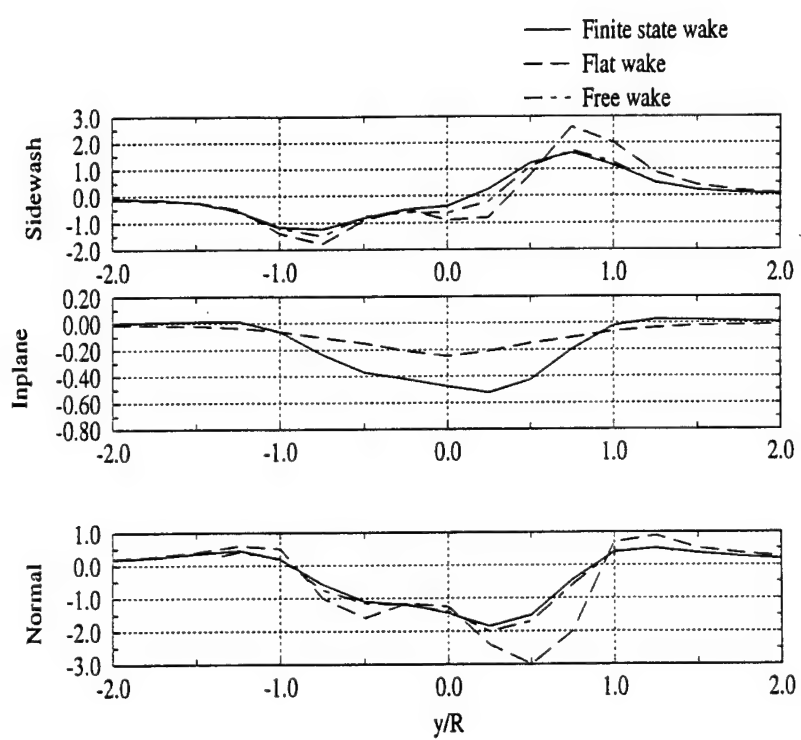


Figure 3.2: Induced flow distribution along horizontal stabilizer, $\mu = 0.2$

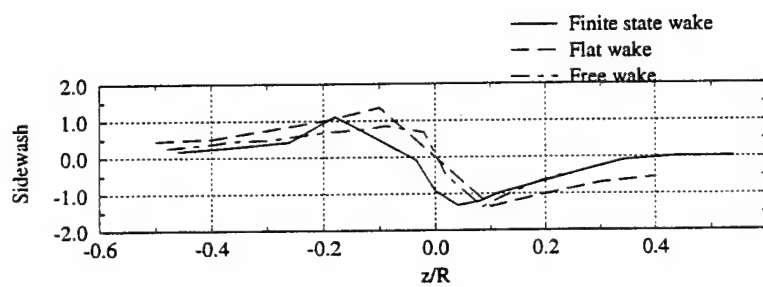


Figure 3.3: Induced velocity distribution along vertical tail, $\mu = 0.2$

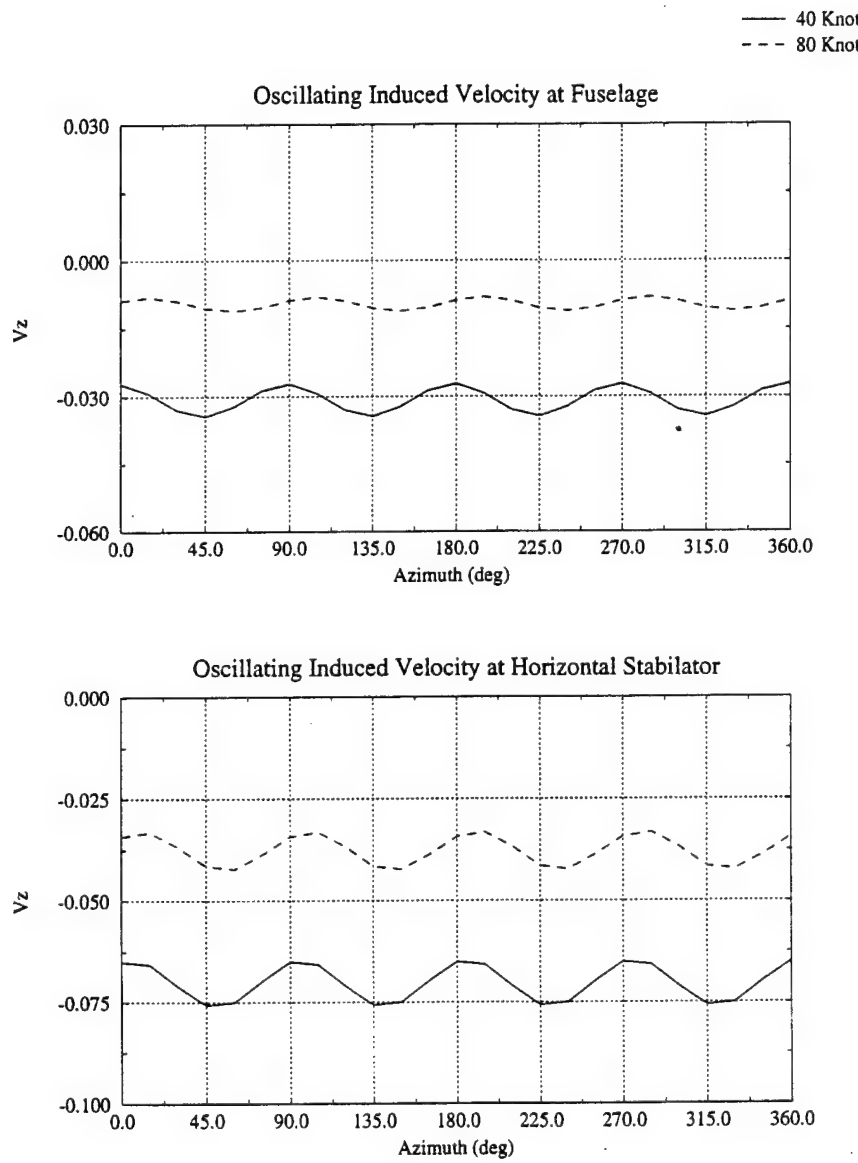


Figure 3.4: Time Varying Induced Velocity at Fuselage and Horizontal Tail

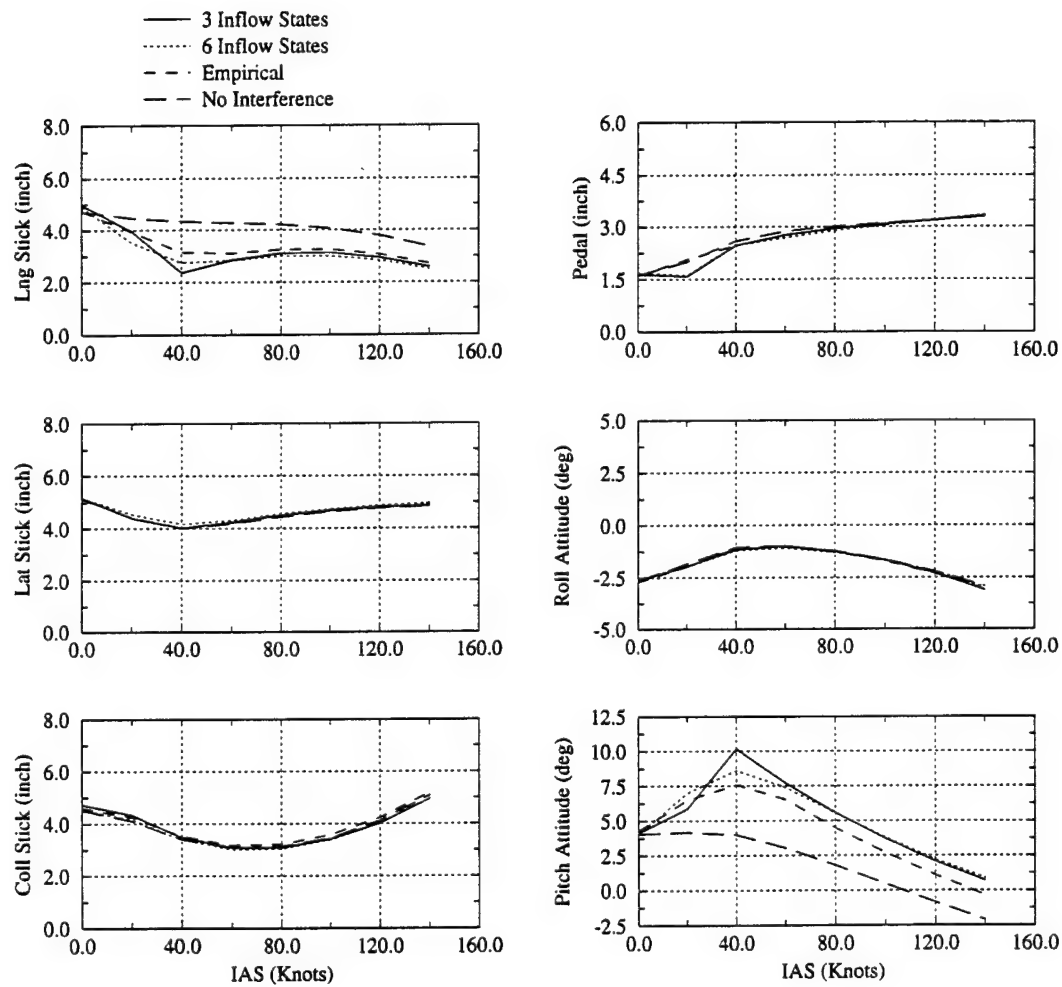


Figure 3.5: UH-60 trim comparison at level flight

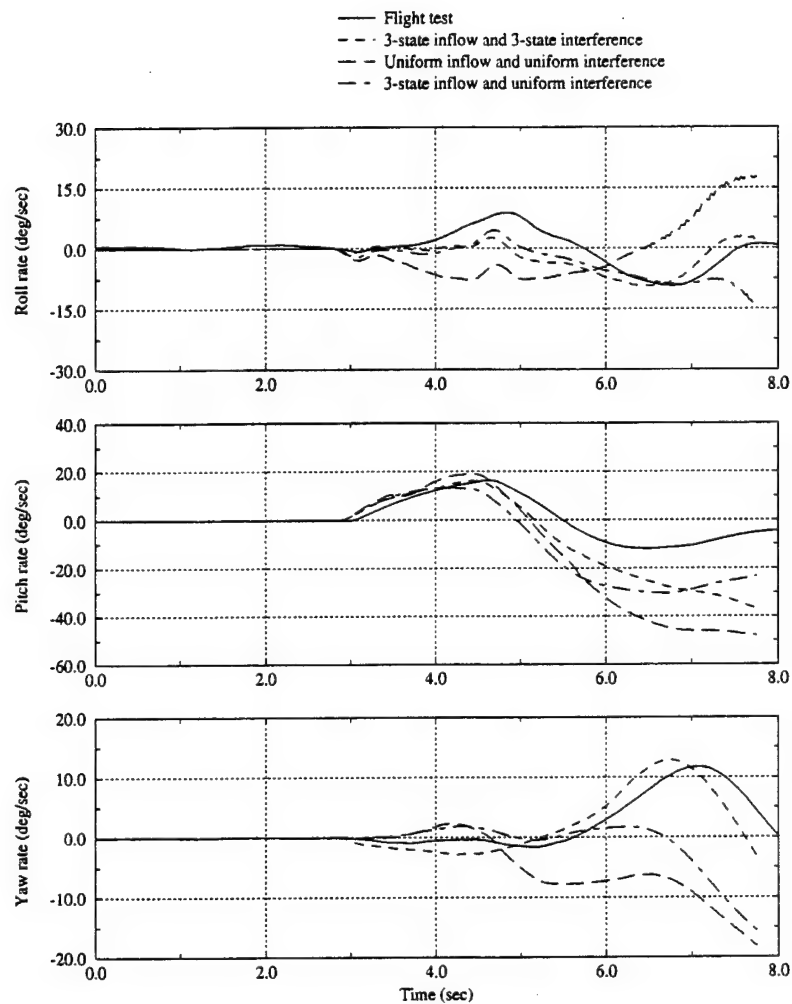


Figure 3.6: UH-60 responses to an aft longitudinal stick (1 inch) at 60 Knots

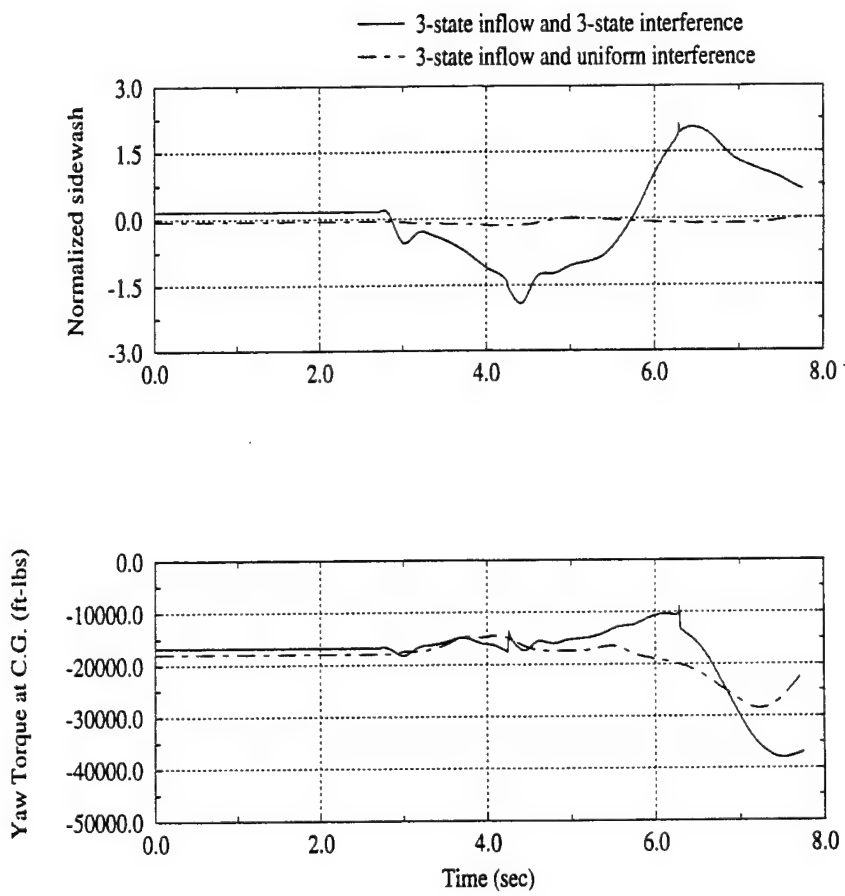


Figure 3.7: Main rotor interference effect on tail rotor, 60 Knots

Chapter 4

Finite State Inflow in Vortex Ring State

As known, all analytical models break down at the vortex ring state. One of the tasks under this contract is to extend the finite state wake model to the vortex ring state. To accomplish this, two important issues need to be addressed.

4.1 Vortex Ring State Boundary

The first is to define the boundary between the vortex ring and the normal flow states. A vortex ring state boundary criteria is required for a smooth transition of the finite state dynamic wake model from the normal flow state to the vortex ring condition. In practice, a validated analytical vortex ring state boundary definition is invaluable as a guidance for a safe helicopter flight. When a helicopter is descending vertically or in a steep descent angle, a definite slipstream ceases to exist. The rotor downwash and normal free stream are in the opposite flow directions. This causes the rotor wake be pushed close to the rotor plane, and the flow around the rotor becomes highly turbulent. This flow condition is usually called rotor vortex ring state. Based on physical observations, the rotor vortex ring state entrance condition occurs when the value of the flow component of total relative air in the negative rotor downwash direction is less than a certain value, i.e.,

$$-\frac{\vec{V}_T \cdot \vec{w}_{i0}}{|\vec{w}_{i0}|} = v_{cr} \quad (4.1)$$

where \vec{V}_T is the total relative air velocity at the rotor plane and \vec{w}_{i0} is the induced velocity. The criteria value where the rotor enters the vortex ring state, v_{cr} , can be further expressed as

$$v_{cr} = g_h w_{ih} \quad (4.2)$$

where w_{ih} is the rotor downwash in hover and g_h can be attained from the measured data, Refs. [23] to [26]. In implementation, this criteria is built into the coefficients of the finite state dynamic wake equations so that a smooth transition to the vortex ring state is obtained.

4.2 Vortex Ring Model

Rotor total inflow is defined as the sum of the rotor downwash and normal free stream, A zero rotor total inflow can result from descent flight for a main rotor or sideward flight for a tail rotor. The zero total inflow implies a zero air mass flow through the rotor in descent flight. The existing finite state dynamic wake model has a singularity at the zero air mass flow condition and is ill-conditioned near the zero air mass flow state. To overcome the singularity and improve the ill-condition in the vortex ring state, a modification of the mass flow parameter in the finite state wake equations is required.

The vortex ring state is highly turbulent. The air viscosity effect plays a significant role on the air flow behavior. No reliable analytical fluid dynamics modeling is available at this time. The approach here is to extend the finite state wake flow parameter into the vortex ring state based on a semi-empirical model derived in the following.

We have experimented with a decay vortex length model, Refs. [28] and [16], in the generalization of the uniform inflow model. Since the model is first derived for vertical descent only, the transition between normal flight and the vortex ring state in forward flight is not smooth. This model also introduces an additional nonlinear equation associated with the decay vortex length. Dependent upon the vortex ring state entrance point there could be a convergence problem in attaining the solution. For this model to work properly in both axial and forward flight, a further modification is needed.

There is an alternative to generalize the finite state wake equations in the vortex ring state. The singularity in the flow parameter of the finite state wake equation can be removed by fitting the data from the universal induced flow curve, Ref. [27], through the vortex ring region. To assure a smooth transition between the universal induced flow data and theoretical prediction outside the vortex ring state, we match them along the vortex ring state entrance boundary, Eq. (4.1).

Under normal flight conditions, the flow parameter is calculated from the total resultant air flow at the rotor plane as follows,

$$\frac{1}{V_T} = \sqrt{\lambda^2 + \mu^2} \quad (4.3)$$

where μ is advance ratio, and λ is the total inflow. To derive the parameter applicable

in the vortex ring region, we assume that

$$\frac{1}{V_{ring}} = J_\lambda J_\mu \quad (4.4)$$

The parameter J_λ is formulated for vertical descent and can be written as

$$J_\lambda = f_{ring} [c_\lambda (\lambda_f + w_{ih})^2 + d_\lambda (\lambda_f + w_{ih}) + e_\lambda] \quad (4.5)$$

where w_{ih} is the nondimensional momentum theory value of induced flow in hover and λ_f is the free stream air flow nondimensionalized by rotor tip speed. The f_{ring} is derived from the universal induced flow data and is approximated by a cubic function as

$$f_{ring} = \frac{2}{C_T} w_{ih} [a_r \left(\frac{\lambda_f}{w_{ih}}\right)^3 + b_r \left(\frac{\lambda_f}{w_{ih}}\right)^2 + c_r \left(\frac{\lambda_f}{w_{ih}}\right) + d_r] \quad (4.6)$$

A curve fit of the universal induced flow data in the range of $-2 < \lambda_f/w_{ih} < -0.5$ gives $a_r = 0.9606$, $b_r = 2.4168$, $c_r = 1.2666$, and $d_r = 1.7099$.

For the generalized induced flow formulation in axial flight, Eq (4.5), there are three coefficients c_λ , d_λ , and e_λ to be defined. They can be determined by matching the theoretical induced flow prediction with the universal data on the the vortex ring state boundary. Three matching points are selected. These include vortex ring state entrance and exit points in vertical descent and a central point inside the vortex ring region. At vortex ring state entrance, we have

$$\lambda_f = -v_{cr} = -g_h w_{ih} \quad (4.7)$$

$$V_{ring} = V_T = \frac{w_{ih}}{2} (-g_h + \sqrt{4 + g_h^2}) \quad (4.8)$$

At vortex ring state exit to the windmill state, we have

$$\lambda_f = -2w_{ih} \quad (4.9)$$

$$V_{ring} = w_{ih} \quad (4.10)$$

At vortex ring state central point,

$$\lambda_f = -w_{ih} \quad (4.11)$$

$$V_{ring} = \frac{1}{f_{ring}} \quad (4.12)$$

Combining the above three conditions, the coefficients can be determined

$$c_\lambda = \frac{B - 1 + (1 - g_h)(A - 1)}{(1 - g_h)(2 - g_h)w_{ih}^2} \quad (4.13)$$

$$d_\lambda = \frac{B - 1 - (1 - g_h)^2(A - 1)}{(1 - g_h)(2 - g_h)w_{ih}} \quad (4.14)$$

$$e_\lambda = 1 \quad (4.15)$$

where

$$A = \frac{1}{f_{ring} w_{ih}} \quad (4.16)$$

$$B = \frac{2A}{-g_h + \sqrt{4 + g_h^2}} \quad (4.17)$$

The parameter J_λ approximates the vertical descent. The parameter J_μ is derived for forward flight descent.

$$J_\mu = g_\mu(1 - \mu)^2 + h_\mu(1 - \mu) + k_\mu \quad (4.18)$$

First, to recover the axial flight modeling, we set J_μ to unity, resulting in

$$g_\mu + h_\mu + k_\mu = 1 \quad (4.19)$$

The second condition is to have V_{ring} match V_T for normal flight, Eq. (4.3), and on the transition boundary, Eq. (4.1). Let μ_{cr} denote the criteria value of advance ratio beyond which no vortex ring state can occur regardless of helicopter descent rate. The parameter μ_{cr} is determined from the vortex ring state criteria Eq. (4.1). This condition yields

$$\frac{1}{J_\lambda J_\mu} = \sqrt{\mu_{cr}^2 + (\lambda_f + w_{i0})^2} \quad (4.20)$$

where w_{i0} is the momentum theory value of induced flow at the boundary

$$w_{i0} = \frac{C_T}{2} \frac{1}{\sqrt{\mu^2 + (\lambda_f + w_{i0})^2}} \quad (4.21)$$

The last condition is to match the universal empirical data at one selected forward descent condition inside the vortex ring region. The point, $\mu = \frac{1}{2}w_{ih}$, has been selected for the fitting since it is located midway between the vertical and forward descent boundary. Thus, we have

$$f_{ring}[g_\mu(1 - \frac{1}{2}w_{ih})^2 + h_\mu(1 - \frac{1}{2}w_{ih}) + k_\mu] = \frac{1}{\sqrt{(\frac{1}{2}w_{ih})^2 + (\lambda_f + f_\mu f_{ring} w_{ih}^2)^2}} \quad (4.22)$$

where the parameter f_μ is obtained from the universal induced flow data. Solving the combined equations (4.19, 4.20, and 4.23) gives

$$k_\mu = 1 - g_\mu - h_\mu \quad (4.23)$$

$$g_\mu = \frac{\frac{1}{2}w_{ih}(A_\mu - 1) - \mu_{cr}(1 - B_\mu)}{\frac{1}{2}\mu_{cr}(\mu_{cr} - 2) - \mu_{cr}w_{ih}(1 - \frac{1}{4}w_{ih})} \quad (4.24)$$

$$h_\mu = \frac{1}{\mu_{cr}}[1 - A_\mu + g_\mu\mu_{cr}(\mu_{cr} - 2)] \quad (4.25)$$

where

$$A_\mu = \frac{w_{i0}|_{\mu=\mu_{cr}}}{J_\lambda w_{ih}^2} \quad (4.26)$$

$$B_\mu = \frac{1}{J_\lambda V_{T\mu_{cr}}} \quad (4.27)$$

$$V_{T\mu_{cr}} = \sqrt{\mu_{cr}^2 + (\lambda_f + w_{i0})^2} \quad (4.28)$$

4.3 Results and Discussion

Figure 4.1 presents the results from the above formulation. The induced velocity is normalized by the momentum theory value in hover, w_{ih} , and plotted as a function of vertical climb/descent rate. The climb/descent rate is also normalized by w_{ih} . The upper figure is for axial flight and the lower is the result at $\mu = 0.5w_{ih}$. The results are also compared to the data obtained from the universal inflow curve, Ref. [27]. As shown, the singularity in the theoretical formulation has been removed and the prediction reasonably matches the measured data. The remaining discrepancy between the analytical formulation and data is not a concern since the agreement is well within the scatter of the measurement.

Figure 4.2 shows the induced flow variations with both vertical and forward descent. A smooth transition between the theoretical and semi-empirical formulations as derived above has been obtained. With this new formulation, the enhanced finite state induced flow model can now be applied in all flight ranges for rotorcraft simulation.

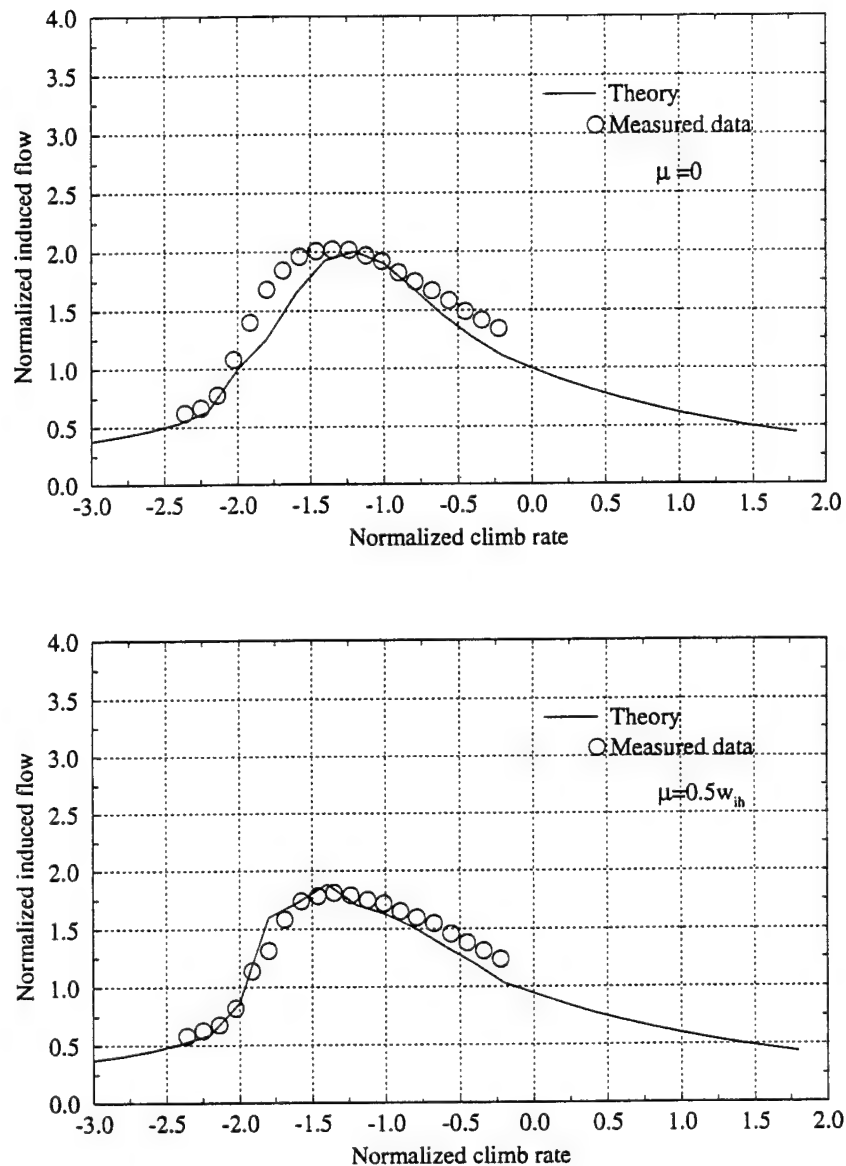


Figure 4.1: Comparison of induced flow between prediction and measured data

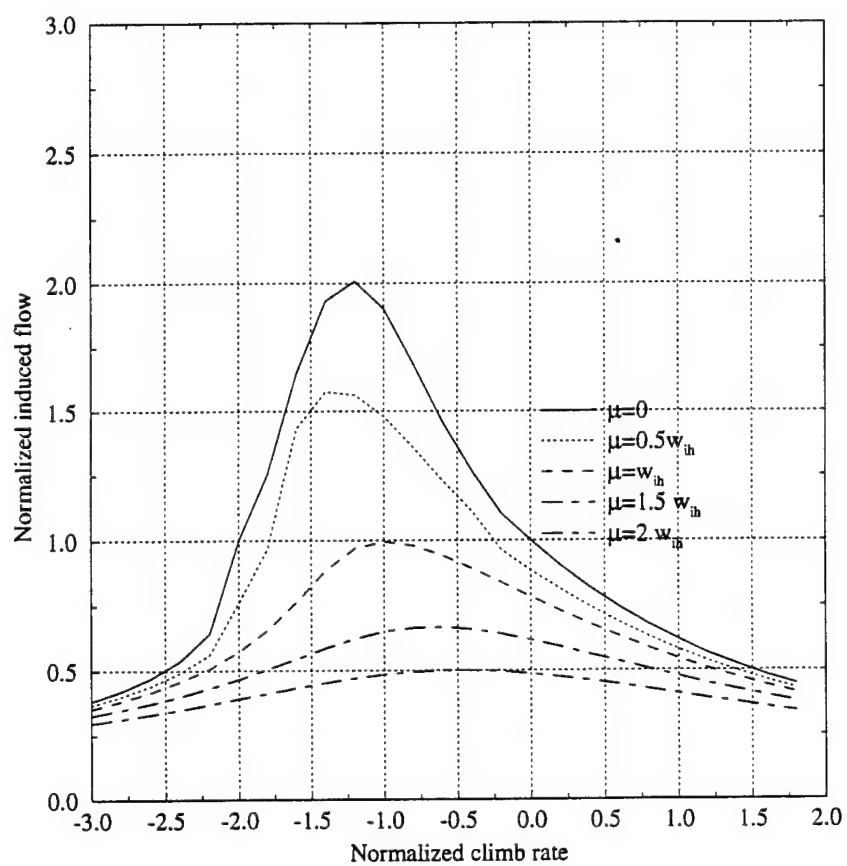


Figure 4.2: Induced flow variation in vertical and forward descent

Chapter 5

Conclusions

For rotorcraft simulation model enhancements, we have developed a finite state dynamic wake formulation that includes the wake distortion effect due to the hub rotation to overcome the poor prediction of rotorcraft off-axis response. The formulation also includes the rotor aerodynamic interference on other lifting surfaces, such as the horizontal tail and the vertical fin, and the tail rotor. An enhancement of the finite state dynamic wake model in the vortex ring state has also been made to generate a simulation model applicable across the full range of flight conditions.

The following conclusions can be made from the Phase One effort:

- A significant breakthrough has been made in the development of a parametric formulation using wake distortion influence coefficients due to hub rotation in both hover and forward flight. It is found that the perturbation inflow states due to the wake distortion vary linearly with the tip-path-plane rotation rate during maneuvering flight. They are also only functions of flight speed and tip-path-plane angle of attack for pitch, and flight speed and tip-path-plane lateral tilt angle for roll.
- Inclusion of a wake distortion effect due to the hub rotation in the finite state induced flow model has greatly improved the correlation of simulation results with the flight test data in pitch/roll coupling. The improvement of the correlation has been obtained in both hover and forward flight.
- The wake distortion effect due to the hub rotation is more pronounced in hover and low speed. The hub rotation effect is mainly on the on-axis inflow distribution (i.e., the fore-to-aft inflow variation due to the pitch and side-to-side inflow change due the roll). The cross-axis inflow variation due to the hub rotation (i.e., the side-to-side inflow distribution due the pitch, or the fore-to-aft inflow distribution due to the roll) is much less significant.
- The capability of the finite state dynamic wake model has been extended in

modeling the aerodynamic interference between the main rotor and the empennage. The results have shown that the aerodynamic interference is an another factor that has an impact on the cross-axis coupling response, such as the yaw due to collective or longitudinal inputs, or the pitch due to sideslip, etc..

- The enhanced model formulation has removed the singularity of inflow variation in the vortex ring state. A smooth induced flow variation has been obtained in both vertical and forward flight descent. The analysis results well match measured universal induced flow curves.
- The formulation of the vortex ring state model has provided a criteria that describes the vortex ring state boundary. This can be used as a flight safety guide.

Chapter 6

Future Plan

We have successfully achieved the Phase One objectives for rotorcraft simulation model enhancement. The Phase One results have shown that the approach is effective and feasible. The formulation developed can be fully implemented in a comprehensive rotorcraft simulation program for both real-time flight simulation or non-real time analysis.

Further Phase Two model enhancement efforts will be made in the following major areas.

- **Wake distortion modeling:** We will fully implement the wake distortion formulation as developed in Phase One in a comprehensive rotorcraft simulation program to address rotorcraft response in both trim and maneuvering flight. Phase One has only performed the feasibility study. For the formulation to be fully validated, more cases will be tested and correlated with measured data.
- **Aerodynamic interaction modeling:** The wake distortion due to the hub rotation mainly affects the helicopter pitch/roll coupling. In forward flight, there are other physical phenomena that affect the simulation correlation with the flight test data in helicopter coupling response. One of them is the fuselage induced fore-to-aft inflow variation at the rotor plane that can influence the helicopter roll response in forward flight. In Phase Two, a panel module for interference velocity calculation will be developed and implemented to model the fuselage and other lifting surfaces with low aspect ratio.
- **Special operation modeling:** We will address the simulation of the vortex ring state in descent and ground effect modeling during ship deck landing. For the vortex ring state modeling, the formulation developed in Phase One will be fully implemented in a comprehensive simulation program, such as FLIGHT-LAB. The vortex ring state boundary will also be computed in the simulation as a flight safety guide and a set of critical azimuth control margin plots will be generated for a selected vehicle. For the ship deck landing, both dynamic

ground effect when the ship deck is moving and partial ground effect will be modeled.

- **Swirl velocity:** We will enhance the finite state dynamic wake model to calculate the induced flow in the azimuthal direction due to the in-plane loading known as swirl effect. The swirl is a unique feature that is especially important for prop-rotors as used in tilt rotor configurations. Due to the high blade pitch setting, the swirl velocity becomes significant in affecting both performance and response analysis of the tilt rotor.
- **Fuselage airloads calculation:** Most rotorcraft simulations still rely on empirical data for fuselage airload calculation. As a first step, a panel model will be developed for the computation of the steady fuselage airloads. The flow separation will be considered by a boundary layer correction with the potential flow solution. The panel airload model will have applications beyond rotorcraft, such as automobile simulation.

Bibliography

- [1] Harris, Frank D. and Scully, Michael P., "Helicopter Cost Too High," Proceedings of 53rd AHS Annual Forum, Virginia Beach, Virginia, April 29-May 1, 1997,
- [2] Proud, R.W., "The Case of the Cross-Coupling Mystery", Rotor/Wing, June 1994.
- [3] Ballin, M.G. and Dalang-Secretan, M.A., "Validation of the Dynamic Response of a Blade element UH60 Simulation Model in Hovering Flight," American Helicopter Society 46th Annual Forum, Washington, D.C., May 1990.
- [4] Rosen, A. and Issur, A., "A New Unsteady Aerodynamic Model for the Coupled Rotor-Body Dynamics," Proceedings of the 51st American Helicopter Society Annual Forum, Forth Worth, Texas, May 1995.
- [5] Keller, Jeffrey, D., "An Investigation of helicopter Dynamic Coupling Using an Analytical Model," Proceedings of 21st European Rotorcraft Forum, St. Petersburg, Russia, Aug. 29 - Sept. 1, 1995.
- [6] Fletcher, Jay, "Identification of Linear Models of the UH-60 in Hover and Forward Flight," 21st European Rotorcraft Forum, St. Petersburg, Russia, Aug. 29 - Sept. 1, 1995.
- [7] Grünhagen, W. von, " Dynamic Inflow Modeling for Helicopter Rotors and Its Influence on the Prediction of Cross-Coupling," Proceedings of the 2nd International Aeromechanics Specialists' Conference of American Helicopter Society, Bridgeport, CT, Oct. 11-13, 1995.
- [8] Pierre-Marie Basset, "Modeling of the Dynamic Inflow on the Main Rotor and the Tail Components in Helicopter Flight Mechanics," Proceedings of 53rd AHS Annual Forum, Virginia Beach, Virginia, April 29-May 1, 1997,
- [9] Padfield, G.D., *Helicopter Flight Dynamics: The Theory and Application of Flying Qualities and Simulation Modeling* , AIAA Education Series, 1996.
- [10] Crawford, C.C., Jr., "Rotorcraft Analytical Improvement Needed to Reduce Development Risk," *J. of AHS*, Vol. 35, No.1 , 1990.

- [11] Sherridan, P.F. and Smith, R.P., "Interactional Aerodynamics - A New Challenge to Helicopter Technology," *Journal of American Helicopter Society*, Vol. 25, No. 1, 1980
- [12] Liou, S.G., Komerath, N.M., and McMahon, H.M., "Measurement of the Interaction between a Rotor Tip Vortex and a Cylinder," *AIAA Journal*, Vol. 28, (6), June 1990.
- [13] Bi, Nai-Pei and Leishman, J.G. , "Experimental Study of Aerodynamic Interactions between a Rotor and Fuselage," AIAA Paper 89-2211, AIAA 7th Applied Aerodynamics Conference, Seattle, Wash. Jul-Aug, 1989.
- [14] Ellin, A.D.S., "An In-Flight Investigation of Lynx AH Mk5 Main Rotor/Tail Rotor Interactions," 19th European Rotorcraft Forum, Cernobbio, Italy, Sept. 1993.
- [15] Curtiss, H.C. Jr. and Quackenbush, T.R., "The Influence of the Rotor Wake on Rotorcraft Stability and Control," Proceedings of 15th European Rotorcraft Forum, Setp. 12-15, 1989, Amesterdam, The Netherlands, Sept. 1989
- [16] Lee, Johnson, He, Cheng-Jian and Xue, Yu, "A Blade Element Tail Rotor Model with Main Rotor/Ground Interference for Yaw Control," Proceedings of AHS Aeromechanics Technology and Product Design for the 21st Century, Oct. 11-13, 1995, Bridgeport, Connecticut.
- [17] Scully, M.P., "A Method of Computing Helicopter Vortex Wake Distortion," MIT, ASRL TR138-1, June 1967.
- [18] Sadler, S.G., "Development and Application of a Method for Predicting Rotor Free Wake Positions and Resulting Rotor Blade Airloads," NASA CR-1911 Vol.I: Model and Results, NASA CR-1912 Program Listing, 1971.
- [19] Quackenbush, T.R. and Bliss, D.B., "Free Wake Prediction of Rotor Flow Fields for Interactional Aerodynamics, " Proceedings of the 44th Annual Forum of the AHS, June 1988.
- [20] Lee, Johnson and He, Cheng-Jian, "A Free Wake/Ground Vortex Model for Rotors at Low Speed In-Ground-Effect Flight," Proceedings of the 51th Annual Forum of the AHS, Fort Worth, TX, May 9-11, 1995.
- [21] Brotherhood, P., "Flow through a Helicopter Rotor in the Vertical Descent," A.R.C.R/M -2735, July 1949
- [22] Stewart, W., "Helicopter Behaviour in the Vortex-Ring Conditions," A.R.C.R/M-3117, November 1951.
- [23] Yeates, J.E., "Flight Measurements of the Vibration Experienced by a Tandem Helicopter in Vortex-Ring State," NACA-TN-4409, August 1958.

- [24] Washizu, K., Azuma, A., Koo, J. and Oka, T., "Experiments on a Modle Helicopter Rotor Operating in the Vortex Ring State," *Journal of Aircraft*, Vol. 3(3), May-June 1966.
- [25] Dress, J.M. and Hendar, W.P., "Air Flow Patterns in the Neighborhood of Helicopter Rotor," *Aircraft Engineering* Vol.3, April 1951
- [26] Xin, Hong and Gao, Zheng, "An Experimental Investigation on Vortex-Ring State Boundary," First Russian Helicopter Society Annual Forum Proceedings, August 1994.
- [27] Johnson, Wayne, "Helicopter Theory," Princeton University Press, Princeton, N.J., 1980.
- [28] Wang, Shi-Cun, "Analytical Approach to the Induced Flow of a Helicopter Rotor in Vertical Descent," *Journal of American Helicopter Society*, Vol. 35(1), Jan. 1990.
- [29] Peters, D.A. and Chen, S.Y., "Momentum Theory, Dynamic Inflow, and the Vortex-Ring State," *Journal of AHS*, Vol. 35(1), Jan. 1982.
- [30] He, Cheng-Jian, "Development and Application of Generalized Dynamic Wake Theory for Lifting Rotors," Ph.D. Thesis, School of Aerospace Engineering, Georgia Institute of Technology, July, 1989.
- [31] Peters D.A. and He, Cheng-Jian, "A Closed Form Unsteady Aerodynamic Theory for Lifting Rotor in Hover and Forward Flight," Proceedings of the 43rd Annual National Forum of the American Helicopter Society, St. Louis, Missouri, May 1987.
- [32] Peters D.A. and He, Cheng-Jian, "Correlation of Measured Induced Velocities with a Finite-State Wake Model ", *Journal of the American Helicopter Society*, Vol. 36, No.3, July, 1991.
- [33] Advanced Rotorcraft Technology, Inc., "FLIGHTLAB Theory Manual," April 20, 1995.
- [34] Amer, K.B., "Theory of Helicopter Damping in Pitch or Roll and Comparison with Flight Measurement," NACA, TN2136, October 1948.
- [35] Sissingh, G.J., "The Effect of Induced Velocity Variation on Helicopter Rotor Damping in Pitch or Roll," Aeronautical Research Council (Great Britain), A.R.C. Technical Report C.P.No.101 (14, 757), 1952.
- [36] Carpenter, P.J. and Fridovich, B., "Effect of a Rapid Blade Pitch Increase on the Thrust and Induced Velocity Response of a Full Scale Helicopter Rotor," NACA TN3044, Nov. 1953.

- [37] Curtiss, H.C., Jr. and Shupe, N.K., "A Stability and Control Theory for Hingeless Rotors," *Proceedings of the 27th Annual National Forum of the American Helicopter Society*, Washington, D.C., May 1971.
- [38] Ormiston, R.A. and Peters, D.A., "Hingeless Rotor Response with Nonuniform Inflow and Elastic Blade Bending," *Journal of Aircraft*, Vol.9, No.10, pp.730-736, October 1972.
- [39] Pitt, D.M. and Peters, D.A., "Theoretical Prediction of Dynamic Inflow Derivatives," *Vertica*, Vol.5, No.1 pp.21-34, March 1981.
- [40] Peters, D.A. and Ninh HaQuang, "Dynamic Inflow for Practical Application," *Journal of the American Helicopter Society*, Vol.33 (4), Oct. 1988.
- [41] He, Cheng-Jian and Du Val, Ronald, "An Unsteady Airload Model with Dynamic Stall for Rotorcraft Simulation," *Proceedings of 50th Annual Forum of the American Helicopter Society*, Washington, D.C. May 11-13, 1994.
- [42] Kuethe, Arnold M. and Chow, Chuen-Yen, *Foundamentals of Aerodynamics*:, Third edition, Published by John Wiley & Sons, Inc.
- [43] Choi, K., He, Cheng-Jian and Du Val, R, "Comparison of Rotormap and and Blade Element Model Simulations Using UH60," *Proceedings of the 52nd American Helicopter Society Forum*, Washington, DC, June, 1996.
- [44] Saberi, Hossein-Ali, Jung, Yoon C. and Anastassiades Tassos, " Finite Element and Modal Method in Multibody Dynamic Code," *Proceedings of American Helicopter Society 2nd International Aeromechanical Specialists' Conference*, Bridgeport, CT 06604, Oct. 11-13, 1995
- [45] Baskin, V.E., "Theory of the Lifting Aircrew, NASA TT F-823, 1976.
- [46] Howlett, J.J, "UH-60A Black Hawk Engineering Simulation Program: Volume I Mathematical Model", NASA CR 166309, Dec., 1981,
- [47] Ballin, M.G., " Validation of a Real-Time Engineering Simulation of the UH-60A Helicopter," NASA TM-100991, 1988.



DETAILS - Awards Search Results

Program: SBIR
Agency: OSD
TOPIC Number: OSD96-012
Contract Number: N00421-97-C-1061
Awarded In: 96
Award Start Date: 15DEC96
Field Office: NAVY
Control Number: N962-1569
Phase: 1
Award Amount: \$99,972
Award Completion Date: 15JUN97

Proposal Title: Rotorcraft Model Enhancements to Support Land and Sea-Based Testing and Operational Analysis

Principal Investigator Name: Cheng-Jian He
Principal Investigator Phone: 415-968-1464

Firm

ADVANCED ROTORCRAFT TECHNOLOGY, INC
1685 Plymouth Street Suite 250
Mountain View, CA 94043

Woman Owned: N
Minority Owned: N
Number of Employees: 0

Keywords:

7085